

Broadband solid-state MAS NMR of paramagnetic systems^{☆,☆☆}

Andrew J. Pell^{a,1}, Guido Pintacuda^{a,*}

^a*Centre de RMN à Très Hauts Champs, Université de Lyon / UMR 5280 CNRS / Ecole Normale Supérieure de Lyon / Université Claude Bernard Lyon 1, 5 rue de la Doua, 69100 Villeurbanne, France*

Abstract

The combination of new magnet and probe technology with increasingly sophisticated pulse sequences has resulted in an increase in the number of applications of solid-state nuclear magnetic resonance (NMR) spectroscopy to paramagnetic materials and biomolecules. The interaction between the paramagnetic metal ions and the NMR-active nuclei often yields crucial structural or electronic information about the system. In particular the application of magic-angle spinning (MAS) has been shown to be crucial to obtaining resolution that is sufficiently high for studying complex systems. However such systems are generally extremely difficult to study as the shifts and shift anisotropies resulting from the same paramagnetic interaction broaden the spectrum beyond excitation and detection, and the paramagnetic relaxation enhancement (PRE) shortens the lifetimes of the excited signals considerably. One specific area that has therefore been receiving significant attention in recent years, and for which great improvements have been seen, is the development of broadband NMR sequences. The development of new excitation and inversion sequences for paramagnetic systems under MAS has often made the difference between the spectrum being unobtainable, and a complete NMR study being possible. However the development of the new sequences must explicitly take account of the modulation of the anisotropic shift interactions due

[☆]Received October 27, 2014

^{☆☆}Edited by J. W. Emsley and J. Feeney

*Corresponding author

Email address: guido.pintacuda@ens-lyon.fr (Guido Pintacuda)

¹Present address: Department of Chemistry, University of Cambridge, Lensfield Road, Cambridge, Cambridgeshire, CB2 1EW, UK

to the sample rotation, with the resulting spin dynamics often being complicated considerably. The NMR sequences can either be helped or hindered by MAS, with the efficiency of some pulse schemes being destroyed, and others being greatly enhanced. This review describes the pulse sequences that have recently been proposed for broadband excitation, inversion, and refocussing of the signal components of paramagnetic systems. In doing so we define exactly what is meant by “broadband” under spinning conditions, and what the perfect pulse scheme should deliver. We also give a unified description of the spin dynamics under MAS which highlights the strengths and weaknesses of the various schemes, and which can be used as guidance for future research in this area. All the reviewed pulse schemes are evaluated both with simulations and experimental data obtained on the battery material $\text{LiFe}_{0.5}\text{Mn}_{0.5}\text{PO}_4$ which is typical of the complexity of the paramagnetic systems that are currently under study.

Keywords: Solid-state NMR, Magic-angle spinning, Paramagnetic, Broadband, Adiabatic pulse, WURST, tanh/tan, Hyperbolic secant, DANTE

Contents

1	Introduction	3
2	General recommendations for NMR of paramagnetic systems	7
3	What is broadband NMR?	9
4	Experimental and simulated examples	12
4.1	A paramagnetic benchmark material	12
4.2	Experimental details	13
4.3	Simulation details	14
5	The chemical shifts of paramagnetic systems	14
5.1	Paramagnetic shifts	15
5.2	Magic-angle spinning	18
5.2.1	Single crystallite spectra	18
5.2.2	Powder averaging	21

6	Radiofrequency pulse schemes	24
6.1	Conventional constant-amplitude pulses applied to static systems	25
6.2	Swept-frequency adiabatic inversion pulses	26
6.3	Superadiabaticity	30
6.4	Delays Alternating with Nutations for Tailored Excitation (DANTE) sequence	33
6.5	Broadband inversion and refocussing	37
6.6	Selective radiofrequency pulses applied to spinning solids: the jolting frame	43
7	Pulse schemes applied to spinning paramagnetic solids	48
7.1	The spin echo	48
7.2	Frequency stepping	53
7.3	Broadband inversion and refocussing with Short, High-power Adiabatic Pulses (SHAPs)	62
7.4	Broadband inversion and refocussing using frequency-selective irradiation by Single-Sideband-Selective Adiabatic Pulses (S ³ APs)	72
7.5	DANTE	85
8	Concluding remarks and recommendations for practical broadband NMR	100
9	Acknowledgements	104

1. Introduction

Solid-state NMR has become established as an important method for structural characterisation in chemistry, biology, and the materials sciences [1]. One area that has seen increased activity in recent years is the development of new NMR methods for studying the structural and electronic properties of paramagnetic solids, and their application to systems of interest [2–11]. The interactions between the NMR-active nuclei and the unpaired electrons of the paramagnetic centres potentially yield important information about the system ranging from the crystal structure to the electron

delocalisation. However these same interactions are also at the root of the problems encountered when attempting to acquire NMR data of these systems. The interactions give rise to (1) large shifts and shift anisotropies (SAs) in the NMR spectrum, resulting in inefficient and non-broadband excitation of the nuclei with practicable radio-frequency (RF) powers, and (2) large paramagnetic relaxation enhancements (PREs) which cause the coherences to decay rapidly once they have been excited. This results in many commonly-used conventional techniques often failing to yield *any* data, and even when the spectrum has been successfully recorded the low sensitivity and poor resolution may render it uninterpretable.

It is of crucial importance to use a broadband pulse sequences to manipulate the nuclear spins in order to obtain meaningful NMR data. Such sequences should be applicable to simple excitation to obtain a conventional one-dimensional spectrum, and ideally be easily incorporated into more complex experiments such as homo- and heteronuclear correlation spectroscopy. Recently a number of broadband NMR techniques have been published for solids under both static and magic-angle spinning (MAS) conditions. The majority of experiments proposed for static powders have been designed for the NMR of nuclei with large quadrupole moments in diamagnetic materials, but are also applicable to spin-1/2 nuclei subject to paramagnetic interactions [12]. Notable examples of experiments include the “ultra-wideline” pulse sequences of Schurko et al. where wideband, uniform rate, and smooth truncation (WURST) frequency-swept pulses are incorporated into the Carr–Purcell–Meiboom–Gill (CPMG) sequence. The resulting WURST-CPMG experiment is combined with frequency-stepped acquisition, where several acquisitions are made with the carrier frequency tuned to different parts of the spectrum and the results added to give the actual spectrum [13]. The WURST pulses have also been incorporated into the cross-polarisation sequence, giving the broadband adiabatic inversion cross polarization (BRAIN-CP) experiment, allowing the transfer of polarisation from ^1H to quadrupolar nuclei with large quadrupole moments [14].

These experiments have been very successful in analysing the NMR parameters for a single nuclear site. However in order to be able to differentiate between several nuclear sites with different isotropic shifts we need to employ magic-angle spinning [15]. In order to average the large SA and obtain the best possible resolution, it

was shown by Ishii et al. that the optimum experimental conditions include spinning at the largest practicable spinning frequency [16]. The substantial improvement obtained by spinning fast is evident from Fig. 1 which shows ^7Li MAS NMR spectra of $\text{LiFe}_{0.5}\text{Mn}_{0.5}\text{PO}_4$. The spectrum at 20 kHz MAS in Fig. 1(a) is broad and featureless, with the individual sidebands barely perceptible. Better resolution between neighbouring sidebands is obtained by doubling the MAS frequency to 40 kHz (Fig. 1(b)), and at 60 kHz MAS there is baseline resolution (Fig. 1(c)).

Very fast MAS must be accompanied by the use of broadband NMR schemes that have been optimised for spinning samples. To date few practical pulse schemes have been proposed for NMR under such conditions, the most notable being frequency-stepping under MAS conditions [17, 18] high-power [19] and low-power adiabatic pulses [20–24], and the application of the Delays Alternating with Nutation for Tailored Excitation (DANTE) [25]. This article reviews these techniques and compares their effectiveness at delivering broadband excitation, refocussing, and inversion. A full theoretical treatment is provided, incorporating the complexity of the anisotropic interactions under MAS, which identifies why and under what conditions the sequences work. In particular the important similarities and differences are highlighted which, in addition to unifying the descriptions in the literature which, at first glance may appear very different, we anticipate will be of help in the design and implementation of new sequences in the future.

This review is organised as follows. Section 2 summarises the high-resolution NMR techniques that have hitherto been applied to paramagnetic systems, and summarises which methods perform best for obtaining different spectra. We then discuss the meaning of “broadband” when applied to spinning solids in Section 3, and highlight important differences to static solids and isotropic solutions. The specialised broadband NMR pulse schemes that are herein described and reviewed were applied to the battery cathode material $\text{LiFe}_{0.5}\text{Mn}_{0.5}\text{PO}_4$, thus obtaining new data which, in combination with simulations, allow a direct comparison of the methods. The experimental and simulation parameters are summarised in Section 4. The remaining sections provide theoretical accounts of these specialised broadband pulse schemes when applied to paramagnetic species in combination with MAS. The origin of the paramagnetic shift and SA

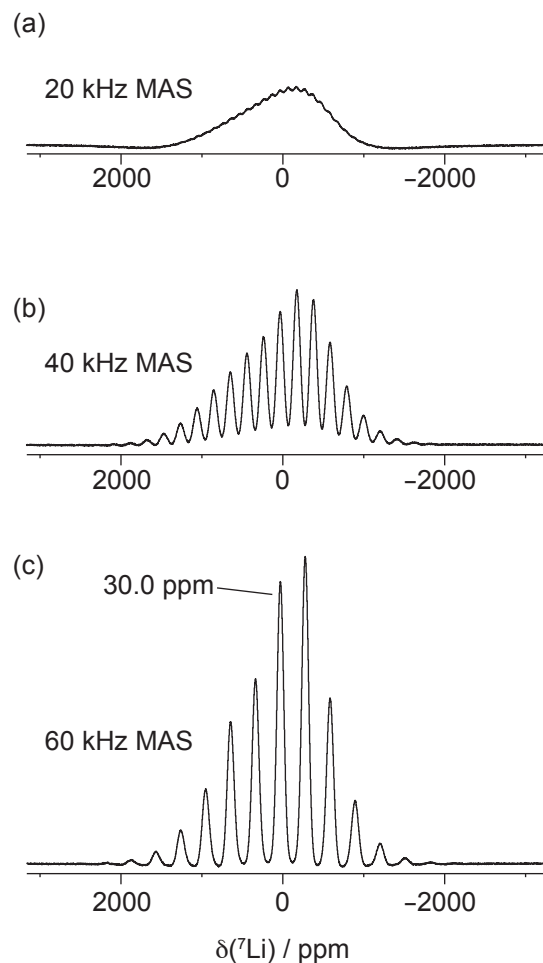


Figure 1: The effect of faster MAS on the spectrum of a paramagnetic material. The examples shown are the ^7Li spectrum of the olivine cathode material $\text{LiFe}_{0.5}\text{Mn}_{0.5}\text{PO}_4$ acquired at 11.74 T, exhibiting large shifts and shift anisotropies due to the hyperfine interactions between the Li nuclei and the unpaired electrons of the surrounding Fe^{2+} and Mn^{2+} ions. The spectrum acquired at 20 kHz MAS is shown in (a) is broad and featureless. Increasing the spinning frequency to (b) 40 kHz dramatically increases the resolution between the neighbouring sidebands, and at 60 kHz MAS (c) we obtain baseline resolution. All spectra were acquired with a 1.3 mm HX probe using the double-SHAP spin echo sequence as described in Section 7.3. The SHAP was a tanh/tan pulse of RF field amplitude 455 kHz that swept through 5 MHz in 50 μs . Excitation at the start of the sequence was achieved with a short, non-selective pulse of RF field amplitude 455 kHz, and length 0.55 μs . 8192 scans were acquired per spectrum with a recycle delay of 100 ms.

is described in Section 5 followed by a description of the SA under MAS conditions, an understanding of which is crucial if the subtleties of the RF pulse schemes is to be fully appreciated. Section 6 describes these pulse schemes, all of which were originally developed for application to isotropic NMR of solutions or magnetic resonance imaging (MRI). This section also includes a description of the excitation sculpting principle [26, 27] when applied under MAS, which allows us to employ *any* inversion pulse to refocussing of coherences. The application of these pulse schemes to spinning solids is described in Section 7, with the interesting effects that are observed with an emphasis of how MAS either helps or hinders their effectiveness. Finally in Section 8 we give a summary of the advantages and disadvantages of the various broadband methods when applied to different types of system, and provide a series of recommendations for practical NMR.

2. General recommendations for NMR of paramagnetic systems

For paramagnetic systems containing several distinct nuclear sites, Ishii demonstrated that the best resolution and sensitivity is obtained by using the highest spinning frequency that is practicable [16]. For a few years now the state of the art has been 60 kHz MAS, and recently faster spinning probes capable of MAS frequencies up to 100 kHz have become available. The reduction in sensitivity from the smaller sample volume of the small-diameter rotors that are capable of spinning at such frequencies is not as serious as one might expect due to the more favourable filling factor. This also allows us to use larger RF field amplitudes, which is an attractive prospect for exciting broad spectra. Ishii also recommended that, where applicable, heteronuclear decoupling sequences are not employed because it is best to rely on the MAS to average out the dipolar coupling interactions. The reason for this is that, except in cases where the paramagnetic interactions are relatively small, the improvement in resolution and coherence lifetimes obtained by heteronuclear decoupling is negligible at best, since the dipolar broadening is dominated by paramagnetic effects and the conventional decoupling sequences are not sufficiently broadband to be effective. In fact, in some cases the decoupling sequence can have a deleterious effect on the spectrum. An additional

advantage obtained by not using decoupling sequences is that the heating effects induced by the RF irradiation of the whole sequence are reduced considerably, and so the recycle delay needs only to allow complete longitudinal relaxation. For paramagnetic systems the longitudinal relaxation times T_1 experience a substantial PRE from the paramagnetic centre, and are usually of the order 100 μ s to 10 ms, allowing between 10s and 100s of scans to be acquired per second. Thus even though a broad distribution of spectral intensity renders a very low signal-to-noise ratio per scan, the short recycle delay means that a usable signal-to-noise ratio can be obtained with a practicable experiment time.

For many years cross-polarisation (CP) has been a staple NMR technique for heteronuclear coherence transfer by irradiation of both nuclei with spin-lock pulses with RF field amplitudes that satisfy that Hartmann–Hahn matching condition [28]. However CP is generally inefficient when applied to paramagnetic systems because the long contact pulses are not sufficiently broadband to spin lock effectively over the whole spectral bandwidth. For MAS frequencies up to 30 kHz, and for small-to-moderate paramagnetic shifts and SAs it has been shown that more efficient coherence transfer can be achieved by using sequences which employ short, high-power pulses with a greater bandwidth. Notable examples of pulse sequences that have been applied successfully are TEDOR [6], the dipolar INEPT [29], and the dipolar HSQC experiments [30]. However a general solution to the problem of heteronuclear coherence transfer for systems subject to large paramagnetic interactions under faster MAS conditions has so far proved elusive.

One of the most widely-used NMR experiments for paramagnetic materials is the spin echo [31], as it allows us to obtain uniform phase over the wide spectral range that cannot be obtained with the single-pulse experiment. However, as discussed in Section 6, the conventional 180° refocussing pulse is very intolerant of large chemical-shift dispersion and RF inhomogeneity effects making it ill-suited for broadband NMR. Recently alternative refocussing schemes have found widespread use such as those using short high-powered adiabatic pulses (SHAPs) [19]. Examples of applications can be found in the studies of organometallic lanthanide complexes [32], and battery materials [33–36]. This scheme is described in detail in Section 7.

3. What is broadband NMR?

Before we launch ourselves into a detailed discussion of the advantages and disadvantages of the various broadband NMR sequences that are available to date, we should first consider exactly what we mean by broadband NMR under MAS conditions.

For spin systems in isotropic environments, either in solution or in the solid state, the term broadband has a straightforward meaning; it refers to the range of isotropic shifts for which the spins can be excited, inverted, or refocussed with the same efficiency, which is preferably 100%. The ability of the pulse or pulse sequence to achieve this aim can be quantified by its *bandwidth*, which is the range of frequencies for which the efficiency of excitation, inversion, or refocussing is greater than a certain (pre-defined) fraction of the maximum, say 90%.

For static solids where the spins are also subject to anisotropic interactions, we must account for the effect of the anisotropic contribution to the shift in our definition of broadband. The anisotropic contribution to the shift is, by definition, dependent of the orientation of the crystallite with respect to the external magnetic field. In a powder sample there are contributions from different crystallite orientations, each of which gives a spectral line in a position that is the sum of the isotropic and anisotropic shifts, and so the observed spectrum is a broadened continuum of intensity over a range that is given by the size of the anisotropy of the shift tensor [37]. The definition of broadband must be extended to include not only excitation over the range of isotropic shifts, but also over the full range of the shift anisotropy. For static solids this extension to the definition is trivial as the isotropic and anisotropic shifts behave identically, and we define the bandwidth as the range of frequencies (rather than isotropic frequencies) over which the required degree of excitation, inversion, or refocussing is attained. The pulses and pulse sequences that we can use to achieve broadband NMR are then the same as those used for isotropic systems, with the difference that they must usually be parameterized for a larger bandwidth as the shift anisotropies may be larger than the range of isotropic shifts.

On the introduction of MAS the situation becomes more complicated [15]. The anisotropic contribution to the shift now behaves in a very different way to the isotropic

contribution. Whereas the former remains constant during the sample rotation, the latter is constantly changing as the MAS constantly changes the orientation of all the crystallites. The variation of anisotropic shift is periodic, which gives rise to the sidebands in the spectrum [38]. The time dependence of the anisotropic shift means that the considerations that apply when designing a sequence for broadband NMR over a range of isotropic shifts do not always apply to the anisotropic shift and vice versa.

Let us imagine a paramagnetic powder with a large anisotropic shift, to which we apply a conventional constant-amplitude pulse that is resonant with the centreband. For a crystallite with a given orientation the effective flip angle of the pulse is given by $\omega_1 A_0 \tau_p$, where ω_1 and τ_p are the RF field amplitude and duration of the pulse, and A_0 is the intensity of the centreband in the sideband manifold of that crystallite, which is normalised so that the sum of the squares of all the sideband intensities is unity [39].

For instance if we imagine a spin system subject to an axially-symmetric shift tensor, the crystallites where the shift tensor is orientated along the magic angle with respect to the external magnetic field are unaffected by MAS, and so give a spectrum with all the spectral intensity is located in the centreband, as shown in Fig. 2(a). On the other hand any crystallites with shift tensors not orientated at the magic angle will exhibit a time modulation of the shift tensor during MAS, and so give a manifold of sidebands as shown for an angle of 99.7° in Fig. 2(b). In the first case $A_0 = 1$ and so the optimum nominal flip angle for achieving perfect inversion is $\omega_1 \tau_p = \pi$, which is the same as the effective flip angle of $\omega_1 A_0 \tau_p$. By contrast crystallites with $A_0 = 0.5$ experience only an effective flip angle of $\pi/2$ which results in only 50% inversion. In order to achieve perfect inversion of the sideband manifold for this crystallite we must double the nominal flip angle $\omega_1 \tau_p$ to 2π with the result that the effective flip angle experienced by this crystallite is now π . However the effect of this new pulse on the first crystallite orientated along the magic angle is that the effective flip angle is now 2π , with the result that there is no net movement of the magnetization. We therefore have the interesting situation where a pulse that is calibrated to invert the sideband manifold for a particular crystallite cannot invert the sideband manifold of a second crystallite where the sidebands are spread over a smaller frequency range, in this case comprising only the centreband!

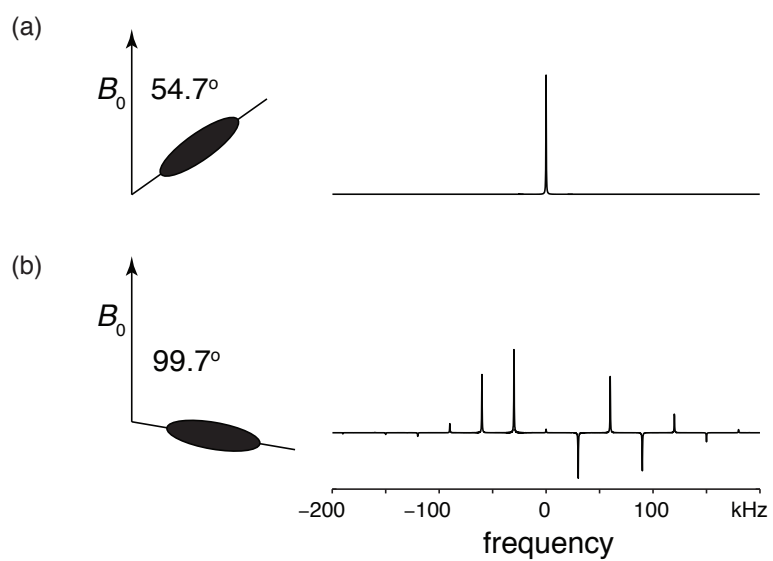


Figure 2: Schematic of the effect of tensor orientation on the MAS spectrum of a single crystallite with an axially-symmetric shift tensor. In (a) is shown a shift tensor orientated at the magic angle (54.7°) with respect to the external field, and the corresponding spectrum in which only the centreband is present. Changing the orientation of the tensor so that it is at 99.7° with respect to the field gives a complex sideband manifold as shown in (b). The shift tensor is represented by the filled ellipsoid.

It therefore follows that we have to think about broadband NMR in a different way to static samples. A broadband pulse or pulse sequence must achieve the following:

1. For different nuclear sites, the pulse must excite, invert, or refocus over a sufficient range of isotropic shifts;
2. For different nuclear sites, the pulse must excite, invert, or refocus over a sufficient range of shift anisotropies;
3. For each individual site, the pulse must achieve 100% excitation, inversion, or refocussing for all crystallite orientations.

All three conditions are equivalent when dealing with static systems, whereas condition 2 and condition 3 become distinct from condition 1 and each other when the sample is spinning.

4. Experimental and simulated examples

Some experimental and simulated examples are given to illustrate the different properties of the various broadband RF sequences that are discussed.

4.1. A paramagnetic benchmark material

The chosen paramagnetic system to illustrate the various concepts and properties of the broadband NMR sequences is the olivine $\text{LiFe}_{0.5}\text{Mn}_{0.5}\text{PO}_4$, which is a cathode material [40, 41], comprising TMO_6 octahedra and PO_4 tetrahedra, the crystal structure of which is shown in Figure 3. The transition metal (TM) sites are occupied either by Fe^{2+} or Mn^{2+} which are present as a solid solution in a 1:1 ratio. The Li atoms occupy the one-dimensional channels and form LiO_6 octahedra, the O atoms of which coordinate to six transition metal ions. Since each TM site can be occupied by either Mn or Fe there are a number of distinct Li sites with different paramagnetic shifts. The ^7Li chemical shifts are dominated by paramagnetic effects from the nearest-neighbour TMs with important contributions from the next-nearest neighbours [42]. The range of isotropic shifts is comparatively small at approximately 90 ppm centred at 0 ppm. There is also a significant inhomogeneous broadening of the sidebands of 90 ppm, which dominates their linewidths. This results in the isotropic shifts of the sites being unresolved in the

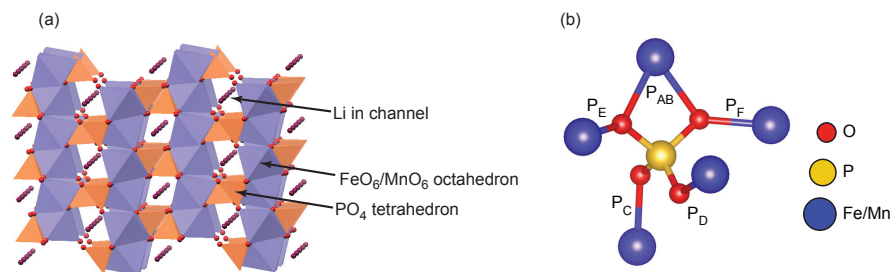


Figure 3: The structure of the olivine $\text{LiFe}_{0.5}\text{Mn}_{0.5}\text{PO}_4$. The olivine crystal structure is shown in (a) showing the TMO_6 octahedra, PO_4 tetrahedra, and one-dimensional channels occupied by Li. In (b) is shown the local structure of the P site, which is coordinating to five transition-metal ion sites AB–F, each the source of a pathway $\text{P}_{\text{AB}}\text{--P}_{\text{F}}$ which contributes to the total paramagnetic shift. Adapted with permission from Ref. [33]. Copyright 2012 American Chemical Society.

NMR spectrum. Each ^7Li site is also subject to a large shift anisotropy primarily due to the dipolar couplings to the unpaired electrons. The longitudinal relaxation times T_1 and coherence lifetimes T_2' are enhanced by paramagnetic effects, and take the bulk values of 1.88 ms and 1.59 ms at a magnetic field of 11.74 T.

The isotropic shifts of the ^{31}P nuclei are dominated by a contact interaction between the nucleus and the unpaired electrons of the five TM ions that coordinate via the bridging O atoms. Longer-range contributions to the paramagnetic shifts from more distant transition metals are negligible, and so there are 32 distinct sites. In contrast to ^7Li the range of shifts for ^{31}P is very large, ranging from 3500 ppm for the all-Fe site to 7900 ppm for the all-Mn site [33], and so the isotropic shifts are in principle resolvable. However in common with ^7Li the dipolar couplings between ^{31}P nuclei and electrons give rise to large shift anisotropies. There is also significant inhomogeneous broadening of the individual sidebands. The longitudinal relaxation times T_1 and coherence lifetimes T_2' for ^{31}P are significantly shorter than for ^7Li . The T_1 relaxation times at 11.74 T field vary for the different sites from 261 μs for the all-Mn site to 524 μs for the all-Fe site, and the T_2' values vary from 132 μs (all-Mn) to 334 μs (all-Fe) [33].

4.2. Experimental details

All experimental spectra were acquired on a Bruker Avance III 500 spectrometer at a field of 11.74 T, and operating at Larmor frequencies of 194 MHz and 202 MHz

for ${}^7\text{Li}$ and ${}^{31}\text{P}$ respectively. The one-dimensional ${}^7\text{Li}$ spectra were acquired using a double-adiabatic spin echo, as described in Section 6.5 with a peak RF field amplitude of 455 kHz for all pulses. The one-dimensional ${}^{31}\text{P}$ spectra were acquired using the same pulse sequence with a peak RF field amplitude of 417 kHz for all pulses. A standard 90° pulse was used for excitation, and refocusing was achieved using two tanh/tan short high-powered adiabatic pulses (SHAPs) [19, 43] that are swept through 5 MHz with a pulse duration of $50\ \mu\text{s}$. All other experimental details are as given in the figure captions.

4.3. Simulation details

All simulations were performed using SPINEVOLUTION version 3.4.5 [44]. The paramagnetic shift and SAs were modelled with a standard chemical shift tensor with an anisotropy of +200 kHz and asymmetry parameter of 0.3. Simulations of powder samples used (α, β) averaging according to the Lebedev octant scheme [45] in combination with γ -averaging, where α , β , and γ are the Euler angles describing the orientation of the crystallite in the rotor reference frame.

5. The chemical shifts of paramagnetic systems

Before reviewing the specific NMR methods used for the broadband excitation of paramagnetic systems we will provide a summary of the interactions that are present in these materials, and show why special care is needed when studying these systems. Firstly we will give an overview of the form of the paramagnetic shift, including a discussion on the size of the interactions, which is important when considering the range of frequencies over which we need to excite. The topic of paramagnetic shifts has been reviewed in detail by Bertini, Luchinat, and Parigi [46, 47], and by Kaupp and Köhler [48]. Secondly we will give a description of the paramagnetic interactions under magic-angle spinning (MAS) conditions [38]. This formalism will be presented in detail as it extremely important for the following description of pulse schemes applied to spinning solids.

5.1. Paramagnetic shifts

The electron paramagnetic resonance (EPR) Hamiltonian describing the interaction between a spin-1/2 nucleus I and a source of unpaired electrons with total spin S is given by the Hamiltonian $\hat{\mathcal{H}}_{\text{EPR}}$ in units of energy:

$$\hat{\mathcal{H}}_{\text{EPR}} = -\hbar\gamma_I \mathbf{B}_0 \cdot (\mathbf{1} - \boldsymbol{\sigma}_{\text{orb}}) \cdot \hat{\mathbf{I}} + \mu_B \mathbf{B}_0 \cdot \mathbf{g} \cdot \hat{\mathbf{S}} + \hat{\mathbf{S}} \cdot \mathbf{A} \cdot \hat{\mathbf{I}} + \hat{\mathbf{S}} \cdot \mathbf{D} \cdot \hat{\mathbf{S}}. \quad (1)$$

In Eq. (1) $\hat{\mathbf{I}}$ and $\hat{\mathbf{S}}$ are the angular momentum operators for the nuclear and total electronic spins, \mathbf{B}_0 is the external magnetic field, μ_B is the Bohr magneton, \hbar is Planck's constant divided by 2π , and γ_I is a nuclear gyromagnetic ratio. The Zeeman interaction of the bare nucleus is described by the coupling of $\hat{\mathbf{I}}$ with \mathbf{B}_0 through the identity matrix $\mathbf{1}$. This is modified by inclusion of the orbital contribution of the open shell to the chemical shielding $\boldsymbol{\sigma}_{\text{orb}}$, which is a generalisation of the chemical shielding that was calculated by Ramsey for closed-shell systems [49]. The spatial dependence of the electron Zeeman interaction is described by the g -tensor \mathbf{g} , and is analogous to the combination of the Zeeman interaction and chemical shielding used to describe the interaction of the nucleus with the field, but is given with different notation. The hyperfine coupling tensor \mathbf{A} describes the interaction between the nucleus and unpaired electrons. Note that both \mathbf{g} and \mathbf{A} have a non-zero isotropic part, and are not in general symmetric [48]. For $S > 1/2$ we also observe the zero-field splitting (ZFS) interaction, the spatial dependence of which is described by the symmetric and traceless tensor \mathbf{D} .

The Hamiltonian in Eq. (1) therefore gives a description of the EPR spectrum with the g -tensor giving the position of the resonance, and the ZFS and hyperfine interactions splitting this resonance into multiple lines, known as the fine structure and hyperfine structure respectively. However the description of the NMR spectrum is more complicated since the rate of electron relaxation is orders of magnitude greater than nuclear relaxation, with typical values of the electron longitudinal relaxation time T_{1e} being in the range 10^{-12} s– 10^{-8} s for the first-row transition metal ions, and 10^{-14} s– 10^{-12} s for the lanthanides (excluding Gd) [46]. The rapid electron relaxation results in an averaging of the electronic magnetic moment, with the result that the splitting due to the hyperfine interaction is averaged to give a shift in the resonance. The effective

NMR Hamiltonian can therefore be written as

$$\hat{\mathcal{H}}_{\text{NMR}} = -\hbar\gamma_I \mathbf{B}_0 \cdot (\mathbf{1} - \sigma_{\text{orb}} - \sigma_{\text{p}}) \cdot \hat{\mathbf{I}}, \quad (2)$$

where σ_{p} is the ‘‘paramagnetic’’ contribution to the chemical shielding. The first general formalism to include all the terms in the EPR Hamiltonian in Eq. (1) was published by Pennanen and Vaara [50] as an extension of an earlier effort by Moon and Patchkovskii [51]. Pennanen and Vaara proposed the following form for σ_{p} :

$$\sigma_{\text{p}} = -\frac{\mu_{\text{B}}}{\hbar\gamma_I kT} \mathbf{g} \cdot \langle \hat{\mathbf{S}} \hat{\mathbf{S}} \rangle_0 \cdot \mathbf{A}, \quad (3)$$

where k is the Boltzmann constant. The ZFS tensor is hidden in the symmetric tensor $\langle \hat{\mathbf{S}} \hat{\mathbf{S}} \rangle_0$, which is a Boltzmann average of the dyadic product of the Cartesian components of $\hat{\mathbf{S}}$ evaluated using the electronic energy levels $E_n(0, 0)$ at zero external field and zero nuclear magnetic moment. It is given by:

$$\langle \hat{\mathbf{S}} \hat{\mathbf{S}} \rangle_0 = \frac{\sum_n \langle n | \hat{\mathbf{S}} \hat{\mathbf{S}} | n \rangle \exp(-E_n(0, 0)/kT)}{\sum_n \exp(-E_n(0, 0)/kT)}. \quad (4)$$

In the absence of the ZFS splitting interaction $\langle \hat{\mathbf{S}} \hat{\mathbf{S}} \rangle_0$ simplifies to

$$\langle \hat{\mathbf{S}} \hat{\mathbf{S}} \rangle_0 = \frac{1}{3} S(S + 1). \quad (5)$$

If we also assume that the g -tensor is simply given by the free-electron g -factor $g_e = 2.0023$, the paramagnetic contribution to the chemical shielding is

$$\sigma_{\text{p}} = -\frac{\mu_{\text{B}} g_e S(S + 1)}{3\hbar\gamma_I kT} \mathbf{A}, \quad (6)$$

which follows the Curie temperature dependence of $1/T$.

In the absence of spin-orbit coupling effects, the hyperfine tensor can be written as the sum of an isotropic Fermi-contact term A_{con} and a traceless, anisotropic, and

symmetric dipolar coupling term \mathbf{A}_{dip} [48]:

$$\mathbf{A} = A_{\text{con}}\mathbf{1} + \mathbf{A}_{\text{dip}}. \quad (7)$$

Both A_{con} and \mathbf{A}_{dip} can be written in terms of the unpaired electron density [52]. For electrons that are approximately localised at the metal ion, the dipolar coupling can be parameterised in terms of the dipolar coupling constant b_{IS} which is given by

$$b_{IS} = \frac{\mu_0 \hbar \gamma_I \mu_B g_e}{4\pi r_{IS}^3}, \quad (8)$$

where r_{IS} is the distance between the nucleus and paramagnetic centre, and μ_0 is the permeability constant. The Fermi-contact term therefore provides a contribution to the isotropic shift of the nucleus, referred to as the Fermi-contact shift, and the dipolar-coupling term gives rise to an SA that is proportional to $2b_{IS}$. To give an idea of the sizes of the shifts and SAs that one can encounter consider the example of a ^{31}P ($\gamma_I = 10.841 \times 10^7 \text{ rads}^{-1}\text{T}^{-1}$) interacting with the five unpaired 3d-electrons of a Mn^{2+} ion ($S = 5/2$). A Fermi-contact interaction with $A_{\text{FC}}/h = 1 \text{ MHz}$ at 298 K will, according to Eq. (6), give an isotropic contribution to the shielding tensor of

$$\sigma_{\text{FC}} = -\frac{9.274 \times 10^{-24} \times 2.0023 \times \frac{5}{2} \times \frac{7}{2}}{3 \times 10.841 \times 10^7 \times 1.38 \times 10^{-23} \times 298} \times 2\pi \times 10^6 = -7.63 \times 10^{-4}, \quad (9)$$

which corresponds to a Fermi-contact shift of 763 ppm. The dipolar coupling constant for a separation of 3 Å is 1.19 MHz, which gives a contribution $\Delta\sigma$ to the SA of

$$\Delta\sigma = -\frac{9.274 \times 10^{-24} \times 2.0023 \times \frac{5}{2} \times \frac{7}{2}}{3 \times 10.841 \times 10^7 \times 1.38 \times 10^{-23} \times 298} \times 2 \times 2\pi \times 1.19 \times 10^6 = -1.8 \times 10^{-3}, \quad (10)$$

or –1800 ppm, which is responsible for a broad spinning sideband manifold. The range of shifts and SAs can therefore be of the order of 100 kHz to 10 MHz, depending on the material under study, and therefore such spins cannot be uniformly excited using practicable RF powers. Therefore it is necessary for the NMR spectroscopist to have an armoury of techniques available for the broadband excitation of such spin systems

in order to investigate paramagnetic materials under MAS.

5.2. Magic-angle spinning

5.2.1. Single crystallite spectra

Under MAS [15, 38, 53], with a rotation frequency of ω_r , the chemical shift Hamiltonian $\hat{\mathcal{H}}_{\text{CS}}(t)$ is the sum of two parts [37]:

$$\hat{\mathcal{H}}_{\text{CS}}(t) = \Omega_0 \hat{I}_z + \Omega_c^{\text{SA}}(\gamma; t) \hat{I}_z. \quad (11)$$

The isotropic frequency Ω_0 , which is observed in solution, is time independent and the same for all crystallites, while the anisotropic frequency $\Omega_c^{\text{SA}}(\gamma; t)$ is time dependent, periodic over the rotor period $\tau_r = 2\pi/\omega_r$, and is in general different for crystallites of different orientations. For a given crystallite these frequencies are given by:

$$\Omega_0 = -\omega_0 \sigma_0, \quad (12)$$

$$\Omega_c^{\text{SA}}(\gamma; t) = \sum_{k=-2, k \neq 0}^{+2} \omega_c^{(k)}(\gamma) \exp(-ik\omega_r t), \quad (13)$$

where ω_0 is the Larmor frequency, σ_0 is the isotropic nuclear shielding, and the coefficients $\omega_c^{(k)}(\gamma)$ are given by

$$\omega_c^{(k)}(\gamma) = -\sqrt{\frac{2}{3}} \omega_0 \sum_{l=-2}^{+2} \tilde{\sigma}_{2l} \exp(-ial) d_{lk}^{(2)}(\beta) d_{k0}^{(2)}(\theta_M) \exp(-ik\gamma), \quad (14)$$

where θ_M is the angle made by the rotor axis relative to the external magnetic field, which is usually set to the magic angle $\tan^{-1}(\sqrt{2})$, $d_{mn}^{(l)}(\theta)$ are the elements of the reduced Wigner rotation matrix of rank l , and the crystallite orientation is defined by the orientation of the principal axis frame (PAF) of the nuclear shielding tensor relative to the rotor. These orientations are parameterised by the three Euler angles α , β , and γ which transform from the former frame to the latter. The symmetric anisotropic part of the nuclear shielding tensor in the PAF is described by the five components of an

irreducible spherical tensor of rank $l = 2$, $\tilde{\sigma}_{2l}$, which are given by:

$$\tilde{\sigma}_{20} = \sqrt{\frac{1}{6}}(3\tilde{\sigma}_{zz} - \sigma_0) = \sqrt{\frac{3}{2}}\Delta\sigma, \quad (15)$$

$$\tilde{\sigma}_{2\pm 1} = 0, \quad (16)$$

$$\tilde{\sigma}_{2\pm 2} = \frac{1}{2}(\tilde{\sigma}_{xx} - \tilde{\sigma}_{yy}) = -\frac{1}{2}\eta\Delta\sigma, \quad (17)$$

where the isotropic shielding σ_0 , shielding anisotropy $\Delta\sigma$, and the asymmetry parameter η are given by:

$$\sigma_0 = \frac{1}{3}(\tilde{\sigma}_{xx} + \tilde{\sigma}_{yy} + \tilde{\sigma}_{zz}), \quad (18)$$

$$\Delta\sigma = \tilde{\sigma}_{zz} - \sigma_0, \quad (19)$$

$$\eta = \frac{\tilde{\sigma}_{yy} - \tilde{\sigma}_{xx}}{\Delta\sigma}. \quad (20)$$

The $\tilde{\sigma}_{ii}$ are the three principal Cartesian components of the tensor in the PAF.

We note from Eq. (13), there are sets of crystallites sharing the same Euler angles α and β , but which have different γ . The crystallites with a particular set occupy the same orientations, but at different times, during the sample rotation, and are referred to as carousels [54], and will be denoted by a subscript c throughout this paper. This carousel symmetry imposes the following periodicity onto the coefficients $\omega_c^{(k)}(\gamma)$:

$$\omega_c^{(k)}(\gamma) = \omega_c^{(k)}(0) \exp(-ik\gamma). \quad (21)$$

During a period of free precession between times t_1 and t_2 , the spin system evolves under the action of the Hamiltonian in Eq. (11). The isotropic and anisotropic contri-

butions to the overall phase $\Phi_0(t_2, t_1)$ and $\Phi_c^{\text{SA}}(\gamma; t_2, t_1)$ are given by:

$$\Phi_0(t_2, t_1) = \int_{t_1}^{t_2} \Omega_0 dt \quad (22)$$

$$= \Omega_0(t_2 - t_1), \quad (23)$$

$$\Phi_c^{\text{SA}}(\gamma; t_2, t_1) = \int_{t_1}^{t_2} \Omega_c^{\text{SA}}(\gamma; t) dt \quad (24)$$

$$= \sum_{k=-2, k \neq 0}^{+2} \frac{\omega_c^{(k)}(\gamma)}{-ik\omega_r} (\exp(-ik\omega_r t_2) - \exp(-ik\omega_r t_1)). \quad (25)$$

The signal component observed in an NMR experiment is simply the complex exponential $\exp(i(\Phi_0(t_2, t_1) + \Phi_c^{\text{SA}}(\gamma; t_2, t_1)))$. In the following we will focus on the anisotropic component of this phase factor $s_c(\gamma; t)$ which is periodic over the rotor period, and can be expanded as a Fourier series

$$s_c(\gamma; t) = \exp(i\Phi_c^{\text{SA}}(\gamma; t, 0)) \quad (26)$$

$$= \sum_{m=-\infty}^{+\infty} A_c^{(m)}(\gamma) \exp(i\phi_c^{(m)}(\gamma)) \exp(im\omega_r t), \quad (27)$$

where the Fourier coefficients have amplitudes $A_c^{(m)}(\gamma)$ and phases $\phi_c^{(m)}(\gamma)$, which are given by

$$A_c^{(m)}(\gamma) \exp(i\phi_c^{(m)}(\gamma)) = \frac{1}{\tau_r} \int_0^{\tau_r} dt \exp(i\Phi_c^{\text{SA}}(\gamma; t, 0)) \exp(-im\omega_r t). \quad (28)$$

We note that these Fourier coefficients are normalised as follows:

$$\sum_{m=-\infty}^{+\infty} [A_c^{(m)}(\gamma)]^2 = 1. \quad (29)$$

The factor $[A_c^{(m)}(\gamma)]^2$ can be interpreted as the fraction of the spectral intensity from the crystallite (α, β, γ) that is present in the sideband of order m [55]. Eq. (26) reveals the origin of the sideband pattern, in which the spectral resonances are split into a series of components which are separated in frequency by the MAS frequency. The label m is referred to as the sideband order, and $A_c^{(m)}(\gamma)$ and $\phi_c^{(m)}$ are referred to the intensity and

phase of this sideband for a crystallite orientation (α, β, γ) .

From Eq. (21) we immediately see that the anisotropic part of the chemical shift frequency under MAS has the following symmetry:

$$\Omega_c^{\text{SA}}(\gamma; t) = \Omega_c^{\text{SA}}(0; t + \gamma/\omega_r). \quad (30)$$

From here it is trivial to ascertain that the anisotropic contribution to the phase $\Phi_c^{\text{SA}}(\gamma; t, 0)$ can be written as

$$\Phi_c^{\text{SA}}(\gamma; t, 0) = \Phi_c^{\text{SA}}(0; t + \gamma/\omega_r, 0) - \Phi_c^{\text{SA}}(0; \gamma/\omega_r, 0). \quad (31)$$

Expanding the phase factors of both sides of Eq. (31) as a Fourier series we obtain the following equality:

$$\begin{aligned} & \sum_{m=-\infty}^{+\infty} A_c^{(m)}(\gamma) \exp(i\phi_c^{(m)}(\gamma)) \exp(im\omega_r t) \\ &= \sum_{m=-\infty}^{+\infty} A_c^{(m)}(0) \exp(i\phi_c^{(m)}(0)) \exp(im(\gamma + \omega_r t)) \exp(-i\Phi_c^{\text{SA}}(0; \gamma/\omega_r, 0)). \end{aligned} \quad (32)$$

On comparing terms of equal sideband order m we obtain the following identities for the sideband intensities and phases [54, 56, 57]:

$$A_c^{(m)}(\gamma) = A_c^{(m)}(0), \quad (33)$$

$$\phi_c^{(m)}(\gamma) = \phi_c^{(m)}(0) - \Phi_c^{\text{SA}}(0; \gamma/\omega_r, 0) + m\gamma. \quad (34)$$

We note that the sideband manifolds of crystallites in a particular carousel have the same intensities, but different phases, and that for a single crystallite the sidebands do not have the same phase. The three single-crystallite spectra in Fig. 4 illustrate this point.

5.2.2. Powder averaging

In a powder all crystallite orientations are present, and the resulting spectrum is the sum of the individual crystallite contributions. Conceptually this sum is computed from

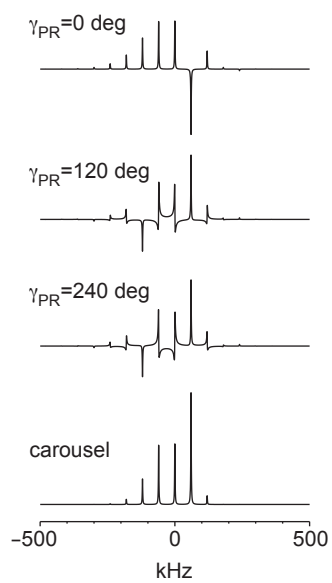


Figure 4: The difference between the NMR spectra of single crystallite, and a complete carousel. Three single-crystallite spectra from the same carousel are shown with γ angles spaced by 120° . Each spectrum exhibits sidebands of different phases, but we note that the pattern of intensities is the same for each crystallites. Averaging over γ gives the carousel spectrum in which all the sidebands have the same phase.

the average over all orientations, but practically this is done in two steps. Following Levitt [54] and Antzutkin et al. [58] we first average the spectra from the crystallites over γ to give the sideband patterns of the individual carousels $\overline{s_c}(t)$

$$\overline{s_c}(t) = \frac{1}{2\pi} \int_0^{2\pi} d\gamma s_c(\gamma; t), \quad (35)$$

and secondly we average over all carousels to obtain the sideband pattern for the full powder $s(t)$

$$s(t) = \frac{1}{4\pi} \int_0^{2\pi} d\alpha \int_0^\pi d\beta \sin(\beta) \overline{s_c}(t). \quad (36)$$

The first average over γ is performed by substituting the expressions for the sideband intensities and phases in Eq. (34) into Eq. (26):

$$s_c(\gamma; t) = \sum_{m=-\infty}^{+\infty} A_c^{(m)} \exp(i\phi_c^{(m)}(0)) \exp(im(\gamma + \omega_r t)) \exp(-i\Phi_c^{\text{SA}}(0; \gamma/\omega_r, 0)). \quad (37)$$

Noting that we can expand $\exp(-i\Phi_c^{\text{SA}}(0; \gamma/\omega_r, 0))$ as a Fourier series:

$$\exp(-i\Phi_c^{\text{SA}}(0; \gamma/\omega_r, 0)) = \sum_{n=-\infty}^{+\infty} A_c^{(n)} \exp[-i(\phi_c^{(n)}(0) + n\gamma)], \quad (38)$$

Eq. (37) becomes

$$s_c(\gamma; t) = \sum_{m,n} A_c^{(m)} A_c^{(n)} \exp[i(\phi_c^{(m)}(0) - \phi_c^{(n)}(0))] \exp[i(m-n)\gamma] \exp(im\omega_r t). \quad (39)$$

Finally, averaging over γ gives

$$\overline{s_c}(t) = \sum_m [A_c^{(m)}]^2 \exp(im\omega_r t), \quad (40)$$

where we see that all the sidebands have the same phase, which is shown for the carousel spectrum in Fig. 4, and that the intensity of the sideband of order m is given by the square of the single-crystallite intensity [54, 56, 57].

The second average stage of the powder averaging now gives the following expres-

sion:

$$s(t) = \sum_m I_m \exp(im\omega_r t), \quad (41)$$

in which the sideband intensities I_m are given by the following integral

$$I_m = \frac{1}{4\pi} \int_0^{2\pi} d\alpha \int_0^\pi d\beta \sin(\beta) [A_c^{(m)}]^2. \quad (42)$$

6. Radiofrequency pulse schemes

In this section we review the radio frequency (RF) pulse schemes that have been applied to the broadband NMR of paramagnetic systems. The pulse schemes herein introduced can all be generally described by the following RF Hamiltonian, which is given in the reference frame that is rotating synchronously with the transmitter frequency of the resonant component of the RF field [59]:

$$\hat{\mathcal{H}}_p(t) = \omega_1(t) \hat{R}_z(\phi_p(t)) \hat{I}_x \hat{R}_z(\phi_p(t))^{-1} \quad (43)$$

$$= \omega_1(t) [\cos(\phi_p(t)) \hat{I}_x + \sin(\phi_p(t)) \hat{I}_y], \quad (44)$$

where $\omega_1(t)$ and $\phi_p(t)$ are (in general time-dependent) amplitude and phase of the pulse. The effect of the time dependence of the phase modulation becomes more transparent if we transform the Hamiltonian $\hat{\mathcal{H}}_p(t)$ into the so-called modulated frame, which is the frame which precesses so that it follows the phase [60]:

$$\hat{\hat{\mathcal{H}}}_p(t) = -\frac{d\phi_p(t)}{dt} \hat{I}_z + \hat{R}_z(\phi_p(t))^{-1} \hat{\mathcal{H}}_p(t) \hat{R}_z(\phi_p(t)) \quad (45)$$

$$= -\omega_{\text{rf}}(t) \hat{I}_z + \omega_1(t) \hat{I}_x. \quad (46)$$

where a frequency offset $\omega_{\text{rf}}(t)$ appears which is given by

$$\omega_{\text{rf}}(t) = \frac{d\phi_p(t)}{dt}. \quad (47)$$

The transmitter offset is therefore modified by adding to it an additional term which is given by the time derivative of the phase.

The two magnetic field components in Eq. 46 combine to give an effective RF field of amplitude $\omega_{\text{eff}}(t)$ given by:

$$\omega_{\text{eff}}(t)^2 = \omega_{\text{rf}}(t)^2 + \omega_1(t)^2, \quad (48)$$

which is tilted with respect to the z -axis by an angle $\theta(t)$, which is given by

$$\tan(\theta(t)) = -\frac{\omega_1(t)}{\omega_{\text{rf}}(t)}. \quad (49)$$

6.1. Conventional constant-amplitude pulses applied to static systems

The conventional constant-amplitude pulse is the simplest form of RF irradiation that is available to NMR. The RF field amplitude is, by definition, constant during the pulse so that $\omega_1(t) \equiv \omega_1$. The phase varies as $\phi_p(t) = \phi_0 - \Omega t$ which results in the pulse having an effective transmitter offset that is different from the carrier by an amount $-\Omega$. The frequency Ω is usually referred to as the offset. In the absence of sample spinning the Hamiltonian in the modulated frame is calculated from Eq. 46, and is given by

$$\hat{\mathcal{H}}_p(t) = \Omega \hat{I}_z + \omega_1 \hat{R}_z(\phi_0) \hat{I}_x \hat{R}_z(\phi_0)^{-1}, \quad (50)$$

from which we immediately see that the magnitude and tilt angle of the effective field are given by:

$$\omega_{\text{eff}}^2 = \Omega^2 + \omega_1^2, \quad (51)$$

$$\tan(\theta) = \frac{\omega_1}{\Omega}. \quad (52)$$

During the pulse the magnetisation precesses about the effective field. If the transmitter is on resonance with the spin ($\Omega = 0$) the precession occurs about the magnetic field due to the pulse, and a flip angle β can be calibrated as $\beta = \omega_1 \tau_p$ where τ_p is the pulse length. The pulse can therefore be used for on-resonance excitation by setting $\beta = \pi/2$, or on-resonance inversion or refocussing with $\beta = \pi$.

When the transmitter is placed off-resonance, so that $\Omega \neq 0$, the precession about the effective field results in a retarded performance for both the 90° and 180° pulses.

It can be shown that 90% excitation for a 90° pulse is achieved only for spins whose offsets lie in the range $-1.58\omega_1 < \Omega < +1.58\omega_1$ [60]. The off-resonance inversion and refocussing performance of 180° pulses is particularly poor, with the range of offsets over which we obtain 90% efficiency being given by $-0.23\omega_1 < \Omega < +0.23\omega_1$ [61]. These shortcomings make it necessary to use more sophisticated RF pulse schemes with a better broadband response.

For spinning samples the theoretical treatment is considerably more complicated, as we must take into account the time dependence of the offset. This is the subject of Section 6.6.

6.2. Swept-frequency adiabatic inversion pulses

During a swept-frequency adiabatic pulse of duration τ_p the RF field amplitude and phase are both modulated so that the effective field rotates from $+z$ to $-z$. If the rate of change of $\theta(t)$ is, at all times, negligible with respect to the size of $\omega_{\text{eff}}(t)$, the magnetisation vector of the spins remains locked to the effective field throughout the pulse, and is thus also inverted [62]. In the last two decades a number of such pulse schemes have been proposed for solution NMR and MRI [43, 63–67]. The profiles of many of these pulses are symmetric to time reversal, and so that amplitude and phase have the following properties:

$$\omega_1(t) = \omega_1(\tau_p - t), \quad (53)$$

$$\phi_p(t) = \phi_p(\tau_p - t). \quad (54)$$

The size of $\omega_1(t)$ is generally increased from zero to its maximum value ω_1^{max} halfway through the pulse, and is then reduced symmetrically to zero during the second half of the irradiation. This ensures that the effective field is parallel to $\pm z$ at the beginning and end of the pulse. The symmetry of the phase results in variation of the transmitter offset so that

$$\omega_{\text{rf}}(t) = -\omega_{\text{rf}}(\tau_p - t). \quad (55)$$

This produces a frequency sweep from $-\Delta\omega/2$ to $+\Delta\omega/2$, where $\Delta\omega$ is the sweep width. The expressions of the amplitude and phase modulation of some of the most

pulse scheme	$\omega_1(t)$	$\phi_p(t)$	$\omega_{\text{rf}}(t)$
hyperbolic secant [63]	$\omega_1^{\text{max}} \text{sech}(\beta(2t/\tau_p - 1))$	$-\frac{\Delta\omega}{2\beta} \ln(\text{sech}(\beta(2t/\tau_p - 1)))$	$\frac{\Delta\omega}{2\beta} \tanh(\beta(2t/\tau_p - 1))$
tanh/tan [43]	$\omega_1^{\text{max}} \tanh\left(\frac{2\xi}{\tau_p}\right), \quad 0 \leq t \leq \tau_p/2$ $\omega_1^{\text{max}} \tanh\left(2\xi\left(1 - \frac{t}{\tau_p}\right)\right), \quad \tau_p/2 < t \leq \tau_p$	$-\frac{\Delta\omega\tau_p}{4\kappa \tan \kappa} \ln(\cos(\kappa(1 - 2t/\tau_p)))$	$-\frac{1}{2} \Delta\omega \cot \kappa \tan(\kappa(1 - 2t/\tau_p))$
WURST [66]	$\omega_1^{\text{max}} \left(1 - \left \sin\left(\pi\left(\frac{t}{\tau_p} - \frac{1}{2}\right)\right)\right ^n\right)$	$\frac{\Delta\omega}{2} \left(\frac{t^2}{\tau_p} - t + \frac{\tau_p}{4}\right)$	$\frac{\Delta\omega}{2} \left(\frac{2t}{\tau_p} - 1\right)$

Table 1: Amplitude $\omega_1(t)$, phase $\phi_p(t)$, and frequency sweep $\omega_{\text{rf}}(t)$ profiles for a selection of swept-frequency adiabatic pulses. For each scheme the transmitter offset is swept through a range of frequencies $\Delta\omega$ during the pulse length of τ_p with a maximum RF field amplitude of ω_1^{max} . For the hyperbolic secant pulse β is a dimensionless parameter given by $\beta = \text{sech} f$, where f is the fraction of ω_1^{max} at which the beginning and end of the amplitude profile are truncated. Typically this truncation factor is set to 1%, and so $\beta = \text{sech}^{-1} 0.01 = 5.2983$. For the tanh/tan pulse ξ and κ are dimensionless parameters which take values $\xi = 10$ and $\kappa = \tan^{-1} 20$. For the WURST pulse n is a factor controlling the rate at which the amplitude profile is smoothed from zero to ω_1^{max} at the start and end of the pulse. Typically $n = 20$.

widely-used pulse schemes are given in Table 1.

We will now formalize the adiabatic condition for inversion starting from the Hamiltonian $\hat{\mathcal{H}}(t)$ in the rotating frame, with reference axes (x, y, z) , which is a sum of the RF term $\hat{\mathcal{H}}_p(t)$ and a term due to the (possible) time dependence of the chemical shift:

$$\hat{\mathcal{H}}(t) = \Omega(t)\hat{I}_z + \hat{\mathcal{H}}_p(t) \quad (56)$$

$$= \Omega(t)\hat{I}_z + \omega_1(t)\hat{R}_z(\phi_p(t))\hat{I}_x\hat{R}_z(\phi_p(t))^{-1}, \quad (57)$$

where $\Omega(t)$ is the sum of the isotropic and anisotropic contributions to the shift. The time evolution of the $\omega_1(t)$ field in the rotating frame due to the pulse phase is shown in Fig. 5(a), with plots of $\omega_1(t)$ and $\omega_{\text{rf}}(t)$ versus time in Fig. 5(f). After transforming into the frequency-modulated frame, which has a new set of reference axes (x_0, y_0, z_0) , the Hamiltonian becomes

$$\hat{\mathcal{H}}^{(0)}(t) = [\Omega(t) - \omega_{\text{rf}}(t)]\hat{I}_z + \omega_1(t)\hat{I}_x \quad (58)$$

$$= \omega_{\text{eff}}^{(0)}(t)\hat{R}_y(\theta^{(0)}(t))\hat{I}_z\hat{R}_y(\theta^{(0)}(t))^{-1}, \quad (59)$$

where the effective field $\omega_{\text{eff}}^{(0)}(t)$ and its angle of tilt from the z -axis $\theta^{(0)}(t)$ are given by:

$$\omega_{\text{eff}}^{(0)}(t)^2 = [\Omega(t) - \omega_{\text{rf}}(t)]^2 + \omega_1(t)^2, \quad (60)$$

$$\tan(\theta^{(0)}(t)) = \frac{\omega_1(t)}{\Omega(t) - \omega_{\text{rf}}(t)}, \quad (61)$$

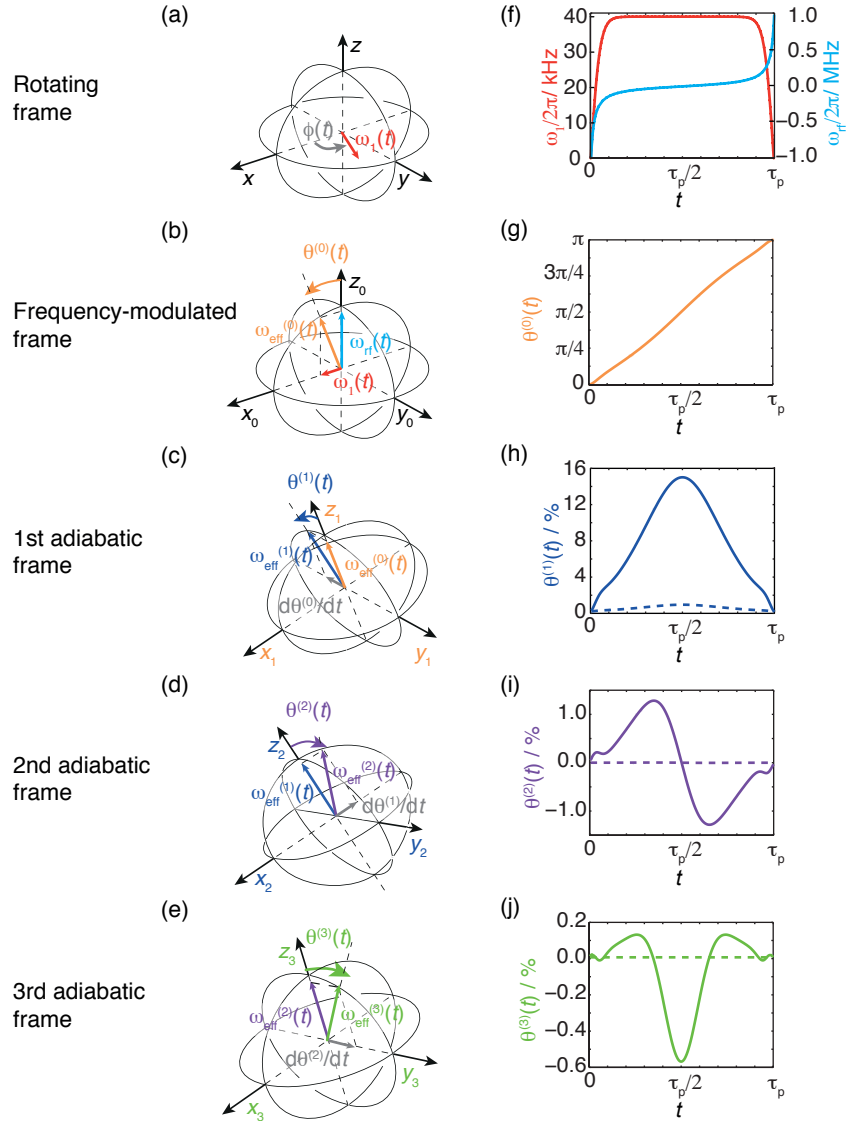


Figure 5: The various axis systems used to visualise swept-frequency adiabatic pulses. The standard rotating frame (x, y, z) is shown in (a). An appropriate change of axis system transforms the magnetic field components into the frequency-modulated frame (x_0, y_0, z_0) in (b), in which we can define an effective magnetic field $\omega_{\text{eff}}^{(0)}(t)$ and its angle of tilt $\theta^{(0)}(t)$ from the z_0 -axis. A further transformation into the first adiabatic frame (x_1, y_1, z_1) , shown in (c), can then be applied, in which the magnetic field components of the pulse can be expressed in terms of a new effective field and tilt angle from the z_1 -axis $\omega_{\text{eff}}^{(1)}(t)$ and $\theta^{(1)}(t)$. This latter transformation can then be repeated, and we can define a second and third adiabatic frame, (x_2, y_2, z_2) and (x_3, y_3, z_3) , which are illustrated in (d) and (e). In both frames the pulse can be described in terms of an effective field and tilt angle. The RF field amplitude $\omega_1(t)$ and the frequency sweep $\omega_{\text{rf}}(t)$ are plotted in (f), and the time variation of the tilt angle of the effective field in the frequency-modulated frame are shown in (f) and (g). The tilt angles of the effective fields in each of the first, second, and third adiabatic frames, as a percentage of the amplitude of the effective field, are plotted as a function of time in (h)–(j). The plots in (f)–(j) were computed for a tanh/tan pulse [43] of 40 kHz RF field amplitude, 2 MHz sweep width, and durations of 2 ms (dashed lines) and 100 μs (full lines). Adapted with permission from Ref. [68]. Copyright 2008 American Institute of Physics.

The orientation of the effective field relative to the axis system of the modulated frame is shown in Fig. 5(b), and the variation of the tilt angle during the pulse is plotted in Fig. 5(g).

A second transformation is now possible, in which the frame follows the path of the effective field. This gives

$$\hat{\mathcal{H}}^{(1)}(t) = \hat{R}_y(\theta^{(0)}(t))^{-1} \hat{\mathcal{H}}^{(0)}(t) \hat{R}_y(\theta^{(0)}(t)) - \dot{\theta}^{(0)}(t) \hat{I}_y \quad (62)$$

$$= \omega_{\text{eff}}^{(0)}(t) \hat{I}_z - \dot{\theta}^{(0)}(t) \hat{I}_y. \quad (63)$$

This frame is referred to as the *adiabatic frame*, the axis system (x_1, y_1, z_1) of which is shown in Fig. 5(c) [62]. The Hamiltonian in this frame is the sum of two terms, namely a ‘large’ magnetic field along z , and a ‘smaller’ field along $-y$. We note that both $\omega_{\text{eff}}^{(0)}(t)$ and $\dot{\theta}^{(0)}(t)$ are actually angular frequencies of precession due to magnetic fields of magnitudes $|\omega_{\text{eff}}^{(0)}(t)/\gamma_I|$ and $|\dot{\theta}^{(0)}(t)/\gamma_I|$, and so we will continue to use the common NMR convention of referring to the former as ‘fields’, in common with $\omega_1(t)$. If the rate of change of $\theta^{(0)}(t)$ is negligible with respect to the effective field $\omega_{\text{eff}}^{(0)}(t)$, that is if the so-called quality factor $Q^{(1)}$, given by

$$\frac{1}{Q^{(1)}} = \max \left| \frac{\dot{\theta}^{(0)}(t)}{\omega_{\text{eff}}^{(0)}(t)} \right| \quad (64)$$

$$= \max \left| \frac{\dot{\omega}_1(t) [\Omega(t) - \omega_{\text{rf}}(t)] - \omega_1(t) [\dot{\Omega}(t) - \dot{\omega}_{\text{rf}}(t)]}{\omega_{\text{eff}}^{(0)}(t)^3} \right|, \quad (65)$$

is much greater than 1, then the term in \hat{I}_y can be ignored, and the Hamiltonian becomes

$$\hat{\mathcal{H}}^{(1)}(t) \approx \omega_{\text{eff}}^{(0)}(t) \hat{I}_z. \quad (66)$$

For a spin in a crystallite of a particular orientation in a static sample (so that $\Omega(t)$ is time independent), the point at which the adiabatic condition is most likely to be violated is usually when the carrier frequency is exactly resonant with the spin as this is where the size of the effective field is at its lowest and where the tilt angle is changing most quickly, both of which will lead to a loss of spin lock efficiency. In this case

$\dot{\theta}^{(0)}(t) = \dot{\omega}_{\text{rf}}(t)/\omega_1^{\text{max}}$ and $\omega_{\text{eff}}^{(0)}(t) = \omega_1^{\text{max}}$, and so the quality factor is simply

$$\frac{1}{Q^{(1)}} = \frac{\dot{\omega}_{\text{rf}}(t)}{(\omega_1^{\text{max}})^2}. \quad (67)$$

The adiabatic condition is then $\dot{\omega}_{\text{rf}}(t) \ll (\omega_1^{\text{max}})^2$, i.e. the rate at which we sweep the carrier on resonance must be much lower than the square of the maximum RF field amplitude. Hence the quality factor can be improved simply by raising the RF power, or by sweeping the transmitter offset more slowly.

Under the action of the adiabatic Hamiltonian, the density operator in the adiabatic frame can now be calculated as

$$\hat{\rho}^{(1)}(t) = \exp\left(-i \int_0^t dt' \omega_{\text{eff}}^{(0)}(t') \hat{I}_z\right) \hat{I}_z \exp\left(+i \int_0^t dt' \omega_{\text{eff}}^{(0)}(t') \hat{I}_z\right) \quad (68)$$

$$= \hat{I}_z, \quad (69)$$

in which we see that the magnetisation remains locked to the effective field. The trajectory of the density operator in the rotating frame can now be recovered by transforming back into this frame:

$$\hat{\rho}(t) = \hat{R}_z(\phi_p(t)) \hat{R}_y(\theta^{(0)}(t)) \hat{\rho}^{(1)}(t) \hat{R}_y(\theta^{(0)}(t))^{-1} \hat{R}_z(\phi_p(t))^{-1} \quad (70)$$

$$= \sin(\theta^{(0)}(t)) [\cos(\phi_p(t)) \hat{I}_x + \sin(\phi_p(t)) \hat{I}_y] + \cos(\theta^{(0)}(t)) \hat{I}_z. \quad (71)$$

We see that as the tilt angle $\theta^{(0)}(t)$ increases from 0 at $t = 0$ to π at $t = \tau_p$, the z term changes from $+\hat{I}_z$ to $-\hat{I}_z$, and the z -magnetization is inverted.

The magnetization trajectories in the rotating frame, frequency-modulated frame, and the adiabatic frame are shown in Fig. 6(a)–(c) for a WURST pulse applied to an isotropic spin system.

6.3. Superadiabaticity

It has recently been shown that the adiabatic approximation cannot be rigorously made for many commonly-used pulses with low $Q^{(1)}$ adiabaticity factors [68]. Nevertheless in these pulses the magnetization trajectories do proceed smoothly to an exact

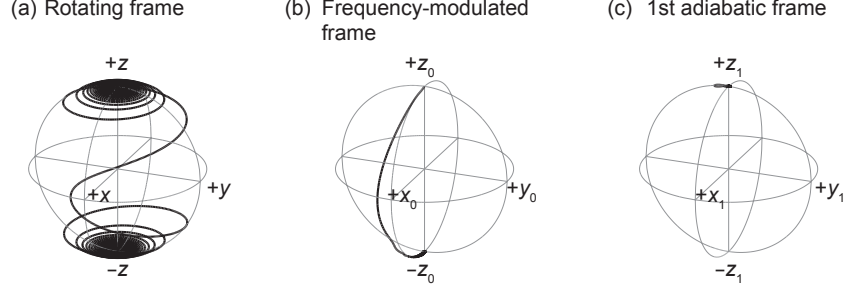


Figure 6: Magnetization trajectories resulting from the application of a WURST pulse to an isotropic spin system. The trajectory in the rotating frame, shown in (a), shows complete inversion of the magnetization vector from $+z$ to $-z$. In addition the vector exhibits a precessional motion about the z -axis resulting in an interchanging of the x - and y -components of the magnetization during the pulse. This precessional motion is removed on transforming to the frequency-modulated frame. The resulting magnetization trajectory, shown in (b), is close to the x_0z_0 plane, and shows a steady sweep of the vector from $+z_0$ to $-z_0$. The small deviation of the path from the x_0z_0 plane is due to deviation of the pulse from perfect adiabatic behaviour. This effect is also observed in the adiabatic frame (c) as a deviation of the magnetisation vector from the z_1 -axis; the deviation is due to the presence of the perturbing field $\dot{\theta}^{(0)}(t)$ along $-y_1$. The isotropic offset of the spin is 0. The WURST pulse swept through a 24 kHz frequency range in 24 ms, at an RF field amplitude of 1 kHz.

inversion. The reason becomes apparent after a careful analysis of the spin-system evolution during the pulse, which shows that magnetisation may be locked during the pulse, not by the effective field in the modulated frame, but rather by the effective field in the adiabatic frame itself. These pulses are dubbed *superadiabatic* [68]. If the $\dot{\theta}^{(0)}(t)$ in Eq. (63) is not negligible we can, instead of applying the adiabatic approximation of Eq. (66), rewrite the Hamiltonian as

$$\hat{\mathcal{H}}^{(1)}(t) = \omega_{\text{eff}}^{(1)}(t) \hat{R}_x(\theta^{(1)}(t)) \hat{I}_z \hat{R}_x(\theta^{(1)}(t))^{-1}, \quad (72)$$

where

$$\omega_{\text{eff}}^{(1)}(t)^2 = \omega_{\text{eff}}^{(0)}(t)^2 + \dot{\theta}^{(0)}(t)^2, \quad (73)$$

$$\tan(\theta^{(1)}(t)) = \frac{\dot{\theta}^{(0)}(t)}{\omega_{\text{eff}}^{(0)}(t)}, \quad (74)$$

where $\omega_{\text{eff}}^{(1)}(t)$ and $\theta^{(1)}(t)$ are the effective field and its tilt angle in the adiabatic frame. The Hamiltonian can then be diagonalised into a second time-dependent adiabatic ref-

erence frame (x_2, y_2, z_2) to give

$$\hat{\mathcal{H}}^{(2)}(t) = \omega_{\text{eff}}^{(1)}(t) \hat{I}_z - \dot{\theta}^{(1)}(t) \hat{I}_x. \quad (75)$$

The tilt angle is plotted as a function of time in Fig. 5(h). We can then define a new adiabatic quality factor $Q^{(2)}$ as

$$\frac{1}{Q^{(2)}} = \max \left| \frac{\dot{\theta}^{(1)}(t)}{\omega_{\text{eff}}^{(1)}(t)} \right|. \quad (76)$$

The scheme can be iterated with the Hamiltonian in the k th adiabatic frame (x_k, y_k, z_k) given by

$$\hat{\mathcal{H}}^{(k)}(t) = \omega_{\text{eff}}^{(k-1)}(t) \hat{I}_z + \dot{\theta}^{(k-1)}(t) \hat{I}_a, \quad (77)$$

with the following effective field and tilt-angle parameters

$$\omega_{\text{eff}}^{(k)}(t)^2 = \omega_{\text{eff}}^{(k-1)}(t)^2 + \dot{\theta}^{(k-1)}(t)^2, \quad (78)$$

$$\tan(\theta^{(k)}(t)) = \frac{\dot{\theta}^{(k-1)}(t)}{\omega_{\text{eff}}^{(k-1)}(t)}, \quad (79)$$

so that the magnetisation clings more closely to the evolving Hamiltonian. The positions of the effective field in the second and third adiabatic frames are shown in Fig. 5(d) and Fig. 5(e) respectively, and the variations of the tilt angles in these frames during the pulse are shown in Fig. 5(i) and Fig. 5(j). In the k th adiabatic frame we can define a quality factor $Q^{(k)}$ as

$$\frac{1}{Q^{(k)}} = \max \left| \frac{\dot{\theta}^{(k-1)}(t)}{\omega_{\text{eff}}^{(k-1)}(t)} \right|. \quad (80)$$

The adiabatic condition can now be restated in terms of a superadiabatic quality factor Q_s which quantifies the minimal rate of change $\dot{\theta}^{(n-1)}(t)$ of the tilt angle of the effective field from the z -axis in the n th adiabatic frame:

$$Q_s \equiv Q^{(n)} = \max(Q^{(k)}) = \max \left| \frac{\dot{\theta}^{(n-1)}(t)}{\omega_{\text{eff}}^{(n-1)}(t)} \right|. \quad (81)$$

If the condition $Q_s \gg 1$ is met, the Hamiltonian in the n th adiabatic frame can be approximated as

$$\hat{\mathcal{H}}^{(n)}(t) \approx \omega_{\text{eff}}^{(n-1)}(t) \hat{I}_z, \quad (82)$$

and therefore results in a perfect inversion.

6.4. Delays Alternating with Nutations for Tailored Excitation (DANTE) sequence

The DANTE sequence was designed originally to achieve selective excitation with high-power pulses in the early days of solution Fourier transform NMR when it was technologically challenging to switch between high- and low-power during the pulse sequence [69, 70]. However it has recently found an application in broadband excitation of both quadrupolar nuclei [25] and spin-1/2 nuclei in paramagnetic systems [71]. The DANTE sequence comprises a series of units, each of length τ_c , comprising a small flip-angle pulse of RF field amplitude ω_1^{max} and length τ_p followed by a delay $\tau_c - \tau_p$ during which the RF field is zero. The RF field amplitude of a single unit is described mathematically as:

$$\omega_1(t) = \begin{cases} \omega_1^{\text{max}}, & 0 \leq t \leq \tau_p \\ 0, & \tau_p < t \leq \tau_c. \end{cases} \quad (83)$$

A DANTE sequence is typically composed of N such units, and so has the following periodicity:

$$\omega_1(t + n\tau_c) = \omega_1(t), \quad (84)$$

where n is an integer.

A typical DANTE excitation profile is shown in Fig. 7(a). Here the DANTE sequence is designed with a cycle frequency of $\omega_c/2\pi = 60$ kHz, and so is able to generate transverse magnetization from spins with isotropic shifts ν_{iso} that are separated from the carrier frequency by multiples of 60 kHz. The magnetization trajectories are shown for a selection of isotropic chemical shifts in Fig. 7(b). For a spin that is on resonance with the carrier $\nu_{\text{iso}} = 0$ there is no chemical-shift evolution during the delays, and so the small-flip-angle pulses simply add together to give an overall excitation with a flip angle $N\omega_1\tau_p$ which can easily be tuned to 90° . As the isotropic shift increases,

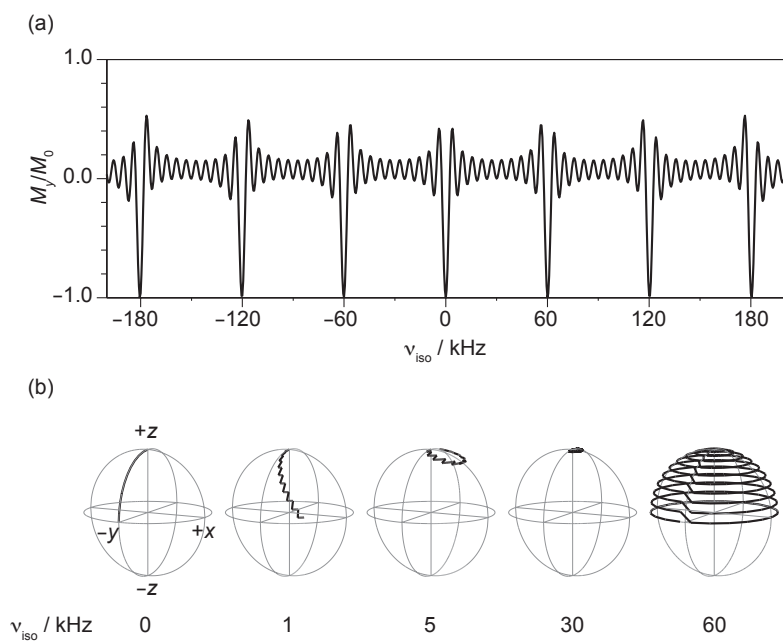


Figure 7: The excitation profile and magnetization trajectories of a DANTE excitation pulse applied to an isotropic spin system [69, 70]. The excitation profile, defined as the y -magnetization generated as a function of isotropic offset, is plotted in (a), and exhibited a ‘comb’ structure in which sidebands of 100% excitation are separated by the reciprocal of the DANTE cycle time, here 60 kHz. In (b) are shown the magnetisation trajectories for different isotropic offsets: 0 (on resonance), 1, 5, 30, and 60 kHz. The DANTE pulse comprises $N = 10$ units, each of cycle time $\tau_c = 16.67 \mu\text{s}$ and corresponding cycle frequency $\omega_c/2\pi = 60 \text{ kHz}$. During each unit the pulse is applied for $\tau_p = 0.5 \mu\text{s}$, at an RF field amplitude of 50 kHz, giving a 90° flip angle on resonance.

however, the chemical shift evolution during the delays interferes with the cumulative precession of the magnetization about the RF magnetic field, meaning that a smaller component of the final magnetization lies in the transverse plane, as can be seen in Fig. 7(b) for $\nu_{\text{iso}} = 1$ and 5 kHz. When $\nu_{\text{iso}} = 30$ kHz, so that the isotropic shift of the spin lies exactly halfway between two pulses in the comb, there is zero net movement of the magnetization vector. By contrast, when the isotropic shift is an integer multiple of the cycle frequency (here $60n$ kHz), the spin system evolves under the shift during each delay so that the magnetization rotates about the z -axis through an angle $2n\pi$ and returns to the position it occupied immediately after the previous pulse, as can be seen for $\nu_{\text{iso}} = 60$ kHz in Fig. 7(b). In these cases, the small-flip-angle pulses combine to give a cumulative excitation effect as if the spin were on resonance with the carrier.

The RF field amplitude function in Eq. (83) can be expanded as a Fourier series

$$\omega_1(t) = \sum_{n=-\infty}^{+\infty} C_n \exp(i(\zeta_n + n\omega_c t)), \quad (85)$$

where $\omega_c = 2\pi/\tau_c$ and the complex coefficients $C_n \exp(i\zeta_n)$, containing an amplitude C_n and phase ζ_n , can be calculated to be

$$C_n \exp(i\zeta_n) = \frac{1}{\tau_c} \int_0^{\tau_c} dt \omega_1(t) \exp(-in\omega_c t) \quad (86)$$

$$= \frac{\omega_1^{\text{max}}}{\tau_c} \int_0^{\tau_p} dt \exp(-in\omega_c t) \quad (87)$$

$$= \begin{cases} \frac{i\omega_1^{\text{max}}}{2n\pi} (\exp(-in\omega_c \tau_p) - 1), & n \neq 0 \\ \frac{\omega_1^{\text{max}} \tau_p}{\tau_c} = \bar{\omega}_1, & n = 0, \end{cases} \quad (88)$$

where $\bar{\omega}_1 = \omega_1^{\text{max}} \tau_p / \tau_c$ is the average RF field amplitude over the whole DANTE sequence. Explicit expressions for the amplitudes and phases can be calculated from Eq. (88), giving:

$$C_n = \begin{cases} \left| \frac{\omega_1^{\text{max}}}{n\pi} \sin\left(\frac{1}{2}n\omega_c \tau_p\right) \right|, & n \neq 0 \\ \bar{\omega}_1, & n = 0 \end{cases} \quad (89)$$

$$\zeta_n = -\frac{1}{2}n\omega_c \tau_p, \quad \text{for all values of } n. \quad (90)$$

The DANTE sequence therefore comprises a comb of RF pulses applied at frequencies $n\omega_c$ with amplitudes that decrease with increasing n according to a sinc function, and phases that are linear in the effective carrier frequency $n\omega_c$.

Of particular interest for broadband excitation are DANTE sequences with pulses of very short duration, so that $\omega_c\tau_p \ll 1$. Applying this condition to Eq. (88) and expanding the complex exponential as a Taylor series, we obtain the following expressions for the coefficient amplitudes and phases:

$$C_n \approx \bar{\omega}_1, \quad \text{for all values of } n \quad (91)$$

$$\zeta_n \approx 0, \quad \text{for all values of } n, \quad (92)$$

which represent a comb of RF pulses applied at frequencies $n\omega_c$ with the same amplitude $\bar{\omega}_1$ and phase. The application of such a sequence to a spin system with a large spinning sideband manifold clearly presents the possibility of uniform excitation of the spin system, as discussed further in Section 7.5.

Alternatively we can consider the case where the RF field is applied constantly during the DANTE sequence, so that $\tau_p = \tau_c$. This example is clearly the same as a single constant-amplitude pulse applied on resonance, as can be seen when we apply this condition to Eq. (88) whence we obtain:

$$C_n = \begin{cases} 0, & n \neq 0 \\ \omega_1^{\max}, & n = 0 \end{cases} \quad (93)$$

$$\zeta_n = 0, \quad \text{for all values of } n, \quad (94)$$

remembering that $\omega_c\tau_c = 2\pi$.

Finally the notion of the DANTE sequence being equivalent to a comb of pulses of amplitudes C_n and phases ζ_n applied at frequencies $n\omega_c$ can be formalised as follows. The time-dependent Hamiltonian $\hat{\mathcal{H}}_p(t)$ representing the sequence of pulses is:

$$\hat{\mathcal{H}}_p(t) = \omega_1(t)\hat{I}_x \quad (95)$$

$$= \sum_{m=-\infty}^{+\infty} C_m \exp(i(\zeta_m + m\omega_c t)) \hat{I}_x. \quad (96)$$

From Eq. (89) and Eq. (90) it is evident that the Fourier coefficient amplitudes and phases have the symmetry $C_{-n} = C_n$ and $\zeta_{-n} = -\zeta_n$ (note that ζ_0 is zero), and so the infinite sum of complex exponentials can be replaced by a sum of cosines:

$$\hat{\mathcal{H}}_p(t) = \sum_{m=-\infty}^{+\infty} C_m \cos(\zeta_m + m\omega_c t) \hat{I}_x. \quad (97)$$

This expression can be rewritten as

$$\hat{\mathcal{H}}_p(t) = \sum_{m=-\infty}^{+\infty} C_m [\cos(\zeta_m + m\omega_c t) \hat{I}_x + \sin(\zeta_m + m\omega_c t) \hat{I}_y], \quad (98)$$

since the symmetry of the Fourier coefficients means that the sum of the sines is zero. The entire sum can now be written as a sum of ‘sandwich’ operator expressions, which gives

$$\hat{\mathcal{H}}_p(t) = \sum_{m=-\infty}^{+\infty} C_m \hat{R}_z(\zeta_m + m\omega_c t) \hat{I}_x \hat{R}_z(\zeta_m + m\omega_c t)^{-1}. \quad (99)$$

This expression describes a sum of pulses each with carrier frequency $m\omega_c$, amplitude C_m , and phase ζ_m , which explains the form of the excitation profile in Fig. 7(a). This expression is therefore the one we will use when formally describing the application of DANTE to spinning solids (see Section 7.5).

6.5. Broadband inversion and refocussing

We have described a number of pulses and pulse sequences that can be used for broadband *inversion* of the z -magnetization of a spin system, and we will now turn our attention to broadband *refocussing* which is more demanding to achieve. In this section we will describe and prove how any element designed to achieve population inversion also be used for the refocussing of the evolution of isotropic and anisotropic chemical shifts under both static and MAS conditions.

Inversion corresponds to the density operator transformation $\hat{I}_z \rightarrow -\hat{I}_z$, which is a relative simple operation to achieve. When a pulse designed to achieve perfect inversion is applied to refocussing of coherences, the transformation may be described as $\hat{I}_+ \rightarrow \hat{I}_- \exp(i\phi)$ which corresponds to a change in coherence order of +1 to -1. In

general, this change in coherence order is accompanied by accrument of a phase ϕ , which is undesirable as the phase may be frequency dependent so that the spectrum is unphasable or, for experiments under MAS conditions, orientation dependent so that the sideband manifolds from different crystallites cancel, giving zero signal from the entire powder. The design of a single broadband refocussing pulse therefore requires the additional constraint that the acquired phase is zero.

Although this condition is generally not met for many classes of RF pulse schemes, including adiabatic pulses, it is always possible to use a pulse designed for inversion to achieve refocussing with uniform phase by employing the idea of excitation sculpting [26]. In solution NMR or the solid-state NMR of static samples the principle is as follows. We first apply the refocussing element once, so that the coherence order changes sign from +1 to -1 and vice versa. The resulting coherence also obtains a frequency-dependent phase as discussed above. However this unwanted phase can be cancelled by apply *exactly the same refocussing element* a second time so that it induces the opposite change in coherence order to the first element. If the element S is part of a spin-echo sequence τ - S - τ , the second element can be incorporated either at the beginning of the echo to give S - τ - S - τ , or as an additional spin echo to give a double spin echo experiment τ - S - τ - τ - S - τ . Even in cases where the pulse-sequence element does not achieve perfect inversion or refocussing, a uniform phase can be achieved over an excitation bandwidth by using appropriate coherence-order-selection methods, such as pulsed-field gradients or phase cycling, independently to each of the elements.

The excitation sculpting principle has been described previously [26], but we will restate it here, generalised to spinning systems, as it is a very important concept to bear in mind when designing new experiments for broadband excitation. The time-dependent Hamiltonian describing the pulse-sequence element S applied to a spin system, which may be static or spinning is $\hat{\mathcal{H}}(t)$. The corresponding propagator $\hat{U}(t_2, t_1)$ describing the effect on the density operator between times t_1 and t_2 has the general form

$$\hat{U}(t_2, t_1) = \hat{\mathcal{T}} \exp \left\{ -i \int_{t_1}^{t_2} \hat{\mathcal{H}}(t) dt \right\}, \quad (100)$$

where $\hat{\mathcal{T}}$ is the Dyson time-ordering operator. The transformation induced by the se-

quence as a whole can be described by an overall rotation operator parameterized by three angles. For example, if the sequence starts at time t_0 and has duration τ_S , the propagator can be written as the following double sandwich of rotation operators:

$$\hat{U}(\tau_S + t_0, t_0) \equiv \hat{V}_S(\xi_S, \theta_S, \phi_S) = \hat{R}_z(\phi_S)\hat{R}_y(\theta_S)\hat{R}_z(\xi_S)\hat{R}_y(\theta_S)^{-1}\hat{R}_z(\phi_S)^{-1}, \quad (101)$$

where ξ_S is the net angle of precession of the magnetization about the net effective magnetic field, the orientation of which is given by a net tilt angle θ_S and phase ϕ_S . Alternatively, the overall transformation of the density operator can be described by a net rotation given by three Euler angles α_S , β_S , and γ_S :

$$\hat{U}(\tau_S + t_0, t_0) \equiv \hat{W}_S(\alpha_S, \beta_S, \gamma_S) = \hat{R}_z(\alpha_S)\hat{R}_y(\beta_S)\hat{R}_z(\gamma_S). \quad (102)$$

In the following we use this second description as it is convenient to describe the rotations in terms of irreducible spherical tensors [72]. Before proceeding, we note that the Euler angles are functions not only of the RF pulse sequence, but also of the parameters describing the chemical shift tensor under MAS, including the isotropic shift, shift anisotropy, asymmetry, the Euler angles describing the orientation of the principal axis frame (PAF) relative to the rotor frame, and the MAS frequency. The Euler angles $(\alpha_S, \beta_S, \gamma_S)$ are therefore dependent on the crystallite orientation.

A propagator of the form given in Eq. (102) transforms an irreducible spherical tensor \hat{T}_{lm} of rank l and order m according to the following relation:

$$\hat{W}_S(\alpha_S, \beta_S, \gamma_S)\hat{T}_{lm}\hat{W}_S(\alpha_S, \beta_S, \gamma_S)^{-1} = \sum_{m'=-l}^{+l} \hat{T}_{lm'}D_{m'm}^{(l)}(\alpha_S, \beta_S, \gamma_S) \quad (103)$$

$$= \sum_{m'=-l}^{+l} \hat{T}_{lm'} \exp(-im'\alpha_S)d_{m'm}^{(l)}(\beta_S) \exp(-im\gamma_S), \quad (104)$$

where $D_{m'm}^{(l)}(\alpha, \beta, \gamma)$ are the elements of the Wigner rotation matrices, and can be written in terms of the reduced Wigner rotation matrix elements as

$$D_{m'm}^{(l)}(\alpha, \beta, \gamma) = \exp(-im'\alpha)d_{m'm}^{(l)}(\beta) \exp(-im\gamma). \quad (105)$$

We see that the rank of the tensor is invariant under the rotation, but the order is not. Firstly we will calculate a general expression for the inversion of z -magnetization by an arbitrary pulse-sequence unit. In the spherical tensor basis the density operator representing magnetization along $+z$ is proportional to $\hat{T}_{10} = \hat{I}_z$. The transformation of this operator under the propagator in Eq. (102) is given by applying Eq. (104) to give

$$\begin{aligned}
\hat{W}_S(\alpha_S, \beta_S, \gamma_S) \hat{T}_{10} \hat{W}_S(\alpha_S, \beta_S, \gamma_S)^{-1} &= \exp(+i\alpha_S) d_{-10}^{(1)}(\beta_S) \hat{T}_{1-1} + d_{00}^{(1)}(\beta_S) \hat{T}_{10} \\
&+ \exp(-i\alpha_S) d_{+10}^{(1)}(\beta_S) \hat{T}_{1+1} \quad (106) \\
&= \cos \beta_S \hat{T}_{10} \\
&+ \sqrt{\frac{1}{2}} \sin \beta_S (\exp(+i\alpha_S) \hat{T}_{1-1} - \exp(-i\alpha_S) \hat{T}_{1+1}).
\end{aligned}$$

The result is a mixture of terms representing z -magnetization (first term) and transverse coherences (second and third terms). We can see immediately that the condition for perfect inversion is for $\beta_S = \pi$ for *all* the crystallite orientations of *all* the chemical sites of interest. If this condition is satisfied the density operator at the end of the sequence is $-\hat{T}_{10}$ and the inversion is complete.

We now turn our attention to the refocussing of the chemical shift evolution. We assume that at the start of the sequence the density operator contains terms only of coherence order -1 , which are proportional to the irreducible spherical tensor $\hat{T}_{1-1} = \hat{I}_- / \sqrt{2}$. The pulse sequence element S transforms this operator as follows:

$$\begin{aligned}
&\hat{W}_S(\alpha_S, \beta_S, \gamma_S) \hat{T}_{1-1} \hat{W}_S(\alpha_S, \beta_S, \gamma_S)^{-1} \\
&= \exp(+i\alpha_S) d_{-1-1}^{(1)}(\beta_S) \exp(+i\gamma_S) \hat{T}_{1-1} + d_{0-1}^{(1)}(\beta_S) \exp(+i\gamma_S) \hat{T}_{10} \\
&+ \exp(-i\alpha_S) d_{+1-1}^{(1)}(\beta_S) \exp(+i\gamma_S) \hat{T}_{1+1} \quad (107)
\end{aligned}$$

$$\begin{aligned}
&= \exp(+i(\alpha_S + \gamma_S)) \frac{1}{2} (1 + \cos \beta_S) \hat{T}_{1-1} - \exp(+i\gamma_S) \sqrt{\frac{1}{2}} \sin \beta_S \hat{T}_{10} \\
&+ \exp(-i(\alpha_S - \gamma_S)) \frac{1}{2} (1 - \cos \beta_S) \hat{T}_{1+1}. \quad (108)
\end{aligned}$$

We see that if the element is designed to give perfect inversion, so that $\beta_S = \pi$ the only term left in Eq. (108) is $\exp(-i(\alpha_S - \gamma_S)) \hat{T}_{1+1}$, which represents pure coherence order

of +1. Therefore if the sequence S gives perfect inversion, it will also give perfect conversion of coherence order -1 to $+1$. In general, however, the conversion efficiency is given by the factor $\frac{1}{2}(1 - \cos\beta_S)$ which is orientation dependent. Even if this conversion is not perfect, the term in \hat{T}_{1+1} can still be selected unambiguously by appropriate phase cycling. Therefore the density operator $\hat{\sigma}_1$ that is present immediately at the end of the sequence is

$$\hat{\sigma}_1 = \exp(-i(\alpha_S - \gamma_S)) d_{+1-1}^{(1)}(\beta_S) \hat{T}_{1+1} \quad (109)$$

$$= \exp(-i(\alpha_S - \gamma_S)) \frac{1}{2}(1 - \cos\beta_S) \hat{T}_{1+1}. \quad (110)$$

We note that, whether or not the conversion to coherence order $+1$ is complete, the term has also acquired a phase of $-(\alpha_S - \gamma_S)$, which is orientation dependent, and so the refocussing is not complete.

We now apply the pulse sequence element S a second time. The transformation of $\hat{\sigma}_1$ by the propagator gives a new density operator $\hat{\sigma}_2$. Phase cycling this second element to select the change in coherence order of -1 to $+1$ gives

$$\hat{\sigma}_2 = \exp(-i(\alpha_S - \gamma_S)) d_{+1-1}^{(1)}(\beta_S) \exp(+i(\alpha_S - \gamma_S)) d_{-1+1}^{(1)}(\beta_S) \hat{T}_{1-1} \quad (111)$$

$$= \frac{1}{4}(1 - \cos\beta_S)^2 \hat{T}_{1-1}, \quad (112)$$

in which the orientation-dependent phase factor has now been eliminated. The amplitude of this term $\frac{1}{4}(1 - \cos\beta_S)^2$ is simply the square of the refocussing efficiency of the sequence, which reflects the fact that it has been applied twice.

This principle has been applied to isotropic systems and to static solids in areas of NMR such as water suppression [26], selective one-dimensional nuclear Overhauser effect (NOE) measurements [27], to adiabatic pulses in MRI [73], and to WURST-CPMG experiments for ultra-wideline NMR [13].

Under MAS conditions, the same principle still holds with the additional constraint that the two elements must be applied so that the rotor is in exactly the same position at the start of the two elements. For example if we consider the double-spin-echo sequence $(n\tau_r - \tau_S/2)-S-(n\tau_r - \tau_S/2)-(n\tau_r - \tau_S/2)-S-(n\tau_r - \tau_S/2)$ where τ_S is the

length of S , we see that the starting points of the two pulse-sequences S are separated by $2n\tau_r$, which is independent of τ_S . Therefore the phase errors of the double echo self-compensate when n is an integer or half-integer. This criterion shows that the sequence S need *not* have a length equal to an integer number of rotor periods, thus allowing the use of sequences that are shorter than a rotor period. In situations where the coherence decay time T'_2 is not much longer than the rotor period, this property allows such pulse sequences to be used without a prohibitive loss in sensitivity. The excitation sculpting principle is also valid under faster MAS conditions, where τ_S is an integer multiple m of the rotor period. For example we can choose $n = m/2 + 1$ to give the following “standard” double-spin-echo sequence: $\tau_r-S-\tau_r-\tau_r-S-\tau_r$, where the starting points of the two sequences S are separated by $m + 2$ rotor periods [19]. However we can improve on this by setting $n = (m + 1)/2$ which gives the shorter double-spin-echo sequence $\tau_r/2-S-\tau_r/2-\tau_r/2-S-\tau_r/2$, where the starting points of the two sequences S are separated by $m + 1$ rotor periods. This latter sequence is preferable in situations where T'_2 is short compared to the rotor period. This sequence can be given a little more versatility by shifting the position of the pulse sequence S of the first spin-echo element so that it no longer falls in the centre of the original spin echo. The first half echo is shortened by an arbitrary delay δ and the second half echo is lengthened by the same amount. Of course according to the excitation sculpting principle we must apply exactly the same change to the second spin echo to compensate for the possible phase errors to give $(\tau_r/2 - \delta)-S-(\tau_r/2 + \delta)-(\tau_r/2 - \delta)-S-(\tau_r/2 + \delta)$. The fact that this sequence refocuses both the isotropic shift and SA can be verified by an explicit calculation the same as that performed by Antzutkin et al. for the PASS experiment [58].

The idea of excitation sculpting under MAS has been applied to SHAPs employed in double adiabatic spin echo experiments [19] and adiabatic magic-angle turning experiments [33], SHAP-CPMG experiments [74], and to trains of crystallite-selective (XS) pulses designed to select a subset of crystallite orientations [75]. In particular we note that, when applying the principle of excitation sculpting to adiabatic pulses in double spin echo experiments, the second pulse must be identical to the first, and in particular must sweep the carrier frequency in the *same* direction.

6.6. Selective radiofrequency pulses applied to spinning solids: the jolting frame

Low-power frequency-selective excitation and inversion schemes have emerged recently as a promising method of manipulating spins subject to large shift anisotropies and quadrupolar interactions. In order to understand how these methods work it is useful to describe them in the “jolting reference frame”, which was first introduced by Caravatti et al [39]. Generally most NMR experiments are described in the standard rotating frame, which is the frame of reference that rotates about the z -axis of the laboratory frame at the RF carrier frequency ω_{rf} . This is convenient because the resonant component of the RF field ω_1 is stationary, and the magnetisation appears to evolve under a reduced magnetic field at an offset $\Omega_0 + \Omega_c^{\text{SA}}(\gamma; t)$. In a solid-state experiment under MAS the sample rotation modulates the anisotropic part of the offset $\Omega_c^{\text{SA}}(\gamma; t)$, which gives rise to a periodic oscillation of the motion of the magnetization about z , so that the magnetization acquires a periodic phase $\Phi_c^{\text{SA}}(\gamma; t_2, t_1)$ in addition to the phase due to the isotropic shift $\Omega_0(t_2 - t_1)$. The former oscillatory part results in a spectrum containing a spinning sideband manifold, in which the sidebands are separated by ω_r as discussed in Section 5.2. This is shown in Fig. 8(a)–(c). In this reference frame the periodic variation of the chemical shift during MAS means that a low-power pulse is resonant with the spin for only a fraction of the time of the rotor period, and so the magnetization nutates about the RF field only for this fraction of time. The pulse length is therefore effectively scaled down. By contrast the jolting frame is a rotating frame that follows the evolution of the magnetization during a period of free precession. In this frame the apparent chemical shift is zero at all times, and the RF field acquires a phase $-\Omega_0(t_2 - t_1) - \Phi_c^{\text{SA}}(\gamma; t_2, t_1)$, and so appears to evolve at minus the chemical shift that is measured in the rotating frame, as shown in Fig. 8(d). The representation of ω_1 in the jolting frame Fig. 8(e) corresponds to a time reversal of the FID in Fig. 8(b), and its Fourier transform in Fig. 8(f) gives a sideband pattern which is equivalent to that in Fig. 8(c) following the reversal of the frequency axis. In this frame the transmitter offset of the pulse undergoes a periodic variation during MAS, and so is resonant with the spin system for only a fraction of the rotor period, leading to the same scaling down of the effective pulse length as in the rotating frame.

This idea can be formalised by starting from the Hamiltonian which describes the

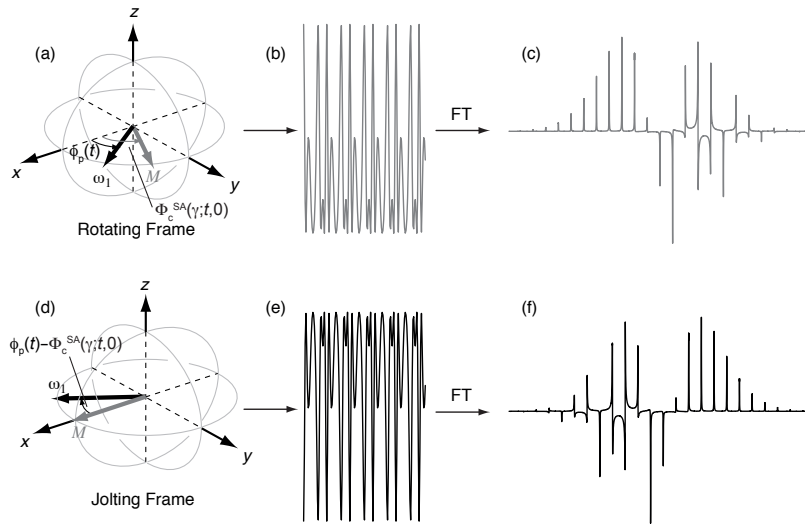


Figure 8: Illustration of the transformation of the magnetic field and magnetisation vector under MAS into the jolting reference frame. In (a) are shown the trajectories of both the $\omega_1(t)$ field and the magnetization vector of a single crystallite M in the rotating frame. Both reside in the xy -plane and accrue time-dependent phases $\phi_p(t)$ and $\Phi_c^{SA}(\gamma; t, 0)$ respectively. The time dependence of the magnetization vector under MAS $\exp(i\Phi_c^{SA}(\gamma; t, 0))$ gives the FID shown in (b). The motion is periodic, and so the corresponding spectrum in (c) exhibits sidebands separated by the spinning frequency. The jolting frame follows the evolution of M , and so in this frame the magnetization is stationary along the x -axis, and the $\omega_1(t)$ field acquires a time-dependent phase that is offset by $-\Phi_c^{SA}(\gamma; t, 0)$, giving $\phi_p(t) - \Phi_c^{SA}(\gamma; t, 0)$, as shown in (d). The Fourier transformation of (d) gives the sideband manifold in (e), which is the same as the spectrum in (c) with the frequency axis reversed. Therefore the RF field splits into a series of components of amplitudes that phases that match the complex conjugate of the sidebands in the spectrum. Adapted with permission from Ref. [24]. Copyright 2011 American Institute of Physics.

RF irradiation in the presence of a CSA under MAS. In the rotating frame this Hamiltonian is

$$\begin{aligned}\hat{\mathcal{H}}(t) &= \Omega_0 \hat{I}_z + \Omega_c^{\text{SA}}(\gamma; t) \hat{I}_z + \omega_1(t) \hat{R}_z(\phi_p(t) + \omega_{\text{tx}} t) \hat{I}_x \hat{R}_z(\phi_p(t) + \omega_{\text{tx}} t)^{-1} \quad (113) \\ &= \Omega_0 \hat{I}_z + \Omega_c^{\text{SA}}(\gamma; t) \hat{I}_z + \omega_1(t) \left[\hat{I}_x \cos(\phi_p(t) + \omega_{\text{tx}} t) + \hat{I}_y \sin(\phi_p(t) + \omega_{\text{tx}} t) \right],\end{aligned}$$

where ω_{tx} is the fixed carrier frequency of the RF pulse, and $\phi_p(t)$ is an additional phase modulation of the irradiation. At this point we make no assumptions about the form of this phase modulation, but we note that everything that follows is valid for any amplitude and phase profile of the pulse. We now perform the transformation into the jolting frame, as described previously [24]. Mathematically the jolting frame is simply the interaction representation of the time-dependent chemical shift interaction. This transformation may be written as

$$\begin{aligned}\hat{\mathcal{H}}(t) &= \exp\left[+i\left(\Omega_0 t + \Phi_c^{\text{SA}}(\gamma; t, 0)\right) \hat{I}_z\right] \hat{\mathcal{H}}(t) \exp\left[-i\left(\Omega_0 t + \Phi_c^{\text{SA}}(\gamma; t, 0)\right) \hat{I}_z\right] \\ &\quad - \left(\Omega_0 + \Omega_c^{\text{SA}}(\gamma; t)\right) \hat{I}_z.\end{aligned} \quad (114)$$

Writing the operator exponentials in terms of rotation operators we obtain:

$$\begin{aligned}\hat{\mathcal{H}}(t) &= \hat{R}_z(\Omega_0 t + \Phi_c^{\text{SA}}(\gamma; t, 0))^{-1} \hat{\mathcal{H}} \hat{R}_z(\Omega_0 t + \Phi_c^{\text{SA}}(\gamma; t, 0)) - \Omega_c^{\text{SA}}(\gamma; t) \hat{I}_z - \Omega_0 \hat{I}_z \quad (115) \\ &= \omega_1(t) \hat{R}_z(\phi_p(t) + \omega_{\text{tx}} t - \Omega_0 t - \Phi_c^{\text{SA}}(\gamma; t, 0)) \hat{I}_x \hat{R}_z(\phi_p(t) + \omega_{\text{tx}} t - \Omega_0 t - \Phi_c^{\text{SA}}(\gamma; t, 0))^{-1} \\ &= \omega_1(t) \left[\hat{I}_x \cos(\phi_p(t) + \omega_{\text{tx}} t - \Omega_0 t - \Phi_c^{\text{SA}}(\gamma; t, 0)) + \hat{I}_y \sin(\phi_p(t) + \omega_{\text{tx}} t - \Omega_0 t - \Phi_c^{\text{SA}}(\gamma; t, 0)) \right],\end{aligned}$$

which shows that, in the jolting frame, the RF field evolves under minus the isotropic chemical shift and CSA interactions. At first sight Eq. (115) appears to be complicated, and one could question whether the use of the jolting frame gives us any additional insight into the spin dynamics of low-power RF irradiation applied to spinning solids. However a significant simplification is facilitated when we remember that the evolution under the shift anisotropy gives rise to a sideband manifold. From Eq. (26) we have the

following relation:

$$\begin{aligned} & \hat{R}_z(\Phi_c^{\text{SA}}(\gamma; t, 0)) \hat{I}_x \hat{R}_z(\Phi_c^{\text{SA}}(\gamma; t, 0))^{-1} \\ &= \sum_{m=-\infty}^{+\infty} A_c^{(m)} \hat{R}_z(\phi_c^{(m)}(\gamma) + m\omega_r t) \hat{I}_x \hat{R}_z(\phi_c^{(m)}(\gamma) + m\omega_r t)^{-1}, \end{aligned} \quad (116)$$

which, when applied to Eq. (115), gives the result

$$\begin{aligned} \hat{\mathcal{H}}(t) &= \omega_1(t) \hat{R}_z(\phi_p(t) + \omega_{\text{tx}} t - \Omega_0 t) \\ &\times \left\{ \sum_{m=-\infty}^{+\infty} A_c^{(m)} \hat{R}_z(\phi_c^{(m)}(\gamma) + m\omega_r t)^{-1} \hat{I}_x \hat{R}_z(\phi_c^{(m)}(\gamma) + m\omega_r t) \right\} \hat{R}_z(\phi_p(t) + \omega_{\text{tx}} t - \Omega_0 t)^{-1}, \end{aligned} \quad (117)$$

for a single crystallite.

Eq. (117) is valid for any arbitrary pulse amplitude and phase profile, but can be difficult to apply in most cases. Nevertheless it is extremely useful for describing the effect of low-power irradiations such that $\omega_1(t) \ll \omega_r$ at all times. We will now give a concrete example, and investigate the effect of a low-power, constant-amplitude, and constant phase ($\phi_p(t) \equiv 0$) pulse, on a spin system with a large CSA. We start by writing the carrier frequency as $\omega_{\text{tx}} = \Omega_0 + n\omega_r$, where n is an integer. This means that the transmitter is resonant with the n -order sideband in the spectrum. Eq. (117) then becomes

$$\hat{\mathcal{H}}(t) = \omega_1 \sum_{m=-\infty}^{+\infty} A_c^{(m)} \hat{R}_z(\phi_c^{(m)}(\gamma) + (m-n)\omega_r t)^{-1} \hat{I}_x \hat{R}_z(\phi_c^{(m)}(\gamma) + (m-n)\omega_r t). \quad (118)$$

We can now apply average Hamiltonian theory and calculate the first-order average Hamiltonian over one rotor period, which gives a valid description of the spin dynamics provided that (1) the low-power approximation $\omega_1 \ll \omega_r$ is observed, and (2) the observation times of the density operator are restricted to integer multiples of the rotor

period [76]. The first-order average Hamiltonian $\hat{\mathcal{H}}$ is:

$$\hat{\mathcal{H}} = \frac{1}{\tau_r} \int_0^{\tau_r} dt \hat{\mathcal{H}}(t) \quad (119)$$

$$= \omega_1 A_c^{(n)} \hat{R}_z(\phi_c^{(n)}(\gamma))^{-1} \hat{I}_x \hat{R}_z(\phi_c^{(n)}(\gamma)). \quad (120)$$

Only one term in the sum is non-zero, which is the term representing the n th-order sideband that is being irradiated. The result is simply a Hamiltonian describing an RF pulse that is applied on resonance with RF field amplitude $\omega_1 A_c^{(n)}$ and phase $-\phi_c^{(n)}(\gamma)$. For each crystallite the RF field amplitude is effectively scaled down by the intensity of the irradiated sideband $A_c^{(n)}$, which is a direct result of the pulse, as observed in the rotating frame, being resonant only with the spin system for a fraction of each rotor period, meaning that the magnetization nutates about the RF field only for the same fraction of time. This fraction of time during which the pulse exerts its nutating effect is strongly dependent on the crystallite orientation, with crystallites in which the irradiated sideband has a larger intensity nutating more quickly. The non-uniformity of this response is a complicating factor that must be addressed when designing broadband pulses. However this same property is extremely useful if we wish to select a subset of crystallite orientations from a powder sample [75], or to select individual sidebands within a broad spinning sideband manifold [18] (see Section 7.2).

It is also possible to applying the jolting frame formalism to study the effects of higher-power pulses for which the low-power approximation begins to break down. In these cases the first-order average Hamiltonian no longer provides an accurate description of the spin dynamics, and it is necessary to calculate higher order terms. Alternatively one can also calculate the series of terms in an effective Hamiltonian by Floquet theory [77–80], which is necessary when the pulse waveform contains an inherent time dependence, such as the phase profile of adiabatic pulses [81]. The details of the calculation are complicated, and are reproduced in full elsewhere [24], and only a brief summary is given here. The second- and third-order Hamiltonians $\hat{\mathcal{H}}^{(2)}$ and $\hat{\mathcal{H}}^{(3)}$ are

each a sum of terms $\Gamma^{(2)}$ and $\Gamma^{(3)}$ which have the form:

$$\Gamma^{(2)} = \frac{\omega_1^2}{\omega_r} \{A^2\} \hat{I}_z \quad (121)$$

$$\Gamma^{(3)} = \frac{\omega_1^3}{\omega_r^2} \{A^3\} \hat{R}_z(\phi^{(3)})^{-1} \hat{I}_x \hat{R}_z(\phi^{(3)}), \quad (122)$$

where the notation $\{A^n\}$ represents a product of n sideband intensities. We can see that the second-order term is proportional to \hat{I}_z , and so gives rise to a Bloch–Siegert shift of the resonance frequency in the jolting frame [59]. By contrast the third-order term is an operator that lies in the transverse plane, and so is an RF field which modifies the first-order field in Eq. (120). The higher-order terms scale inversely with the spinning frequency, either as ω_r^{-1} or ω_r^{-2} , and so become less important as we reduce the RF field amplitude, eventually returning to the low-power approximation.

7. Pulse schemes applied to spinning paramagnetic solids

In this Section we review the methods that have been published for obtaining a broadband NMR spectrum of nuclear species in a paramagnetic material. For each method there will also be a brief discussion on whether the various pulse schemes can be incorporated into more complex experiments designed to extract structural or electronic information.

7.1. The spin echo

The most widely used pulse sequence in paramagnetic NMR is the spin echo, sometimes referred to as the Hahn echo after Erwin Hahn [31]. The basic sequence takes the form

$$90^\circ - \tau - 180^\circ - \tau - \text{acq.}, \quad (123)$$

with EXORCYCLE applied to the 180° refocussing pulse so as to select a change in coherence order of $+1$ to -1 , so that coherences of these orders evolve during the first and second delays τ respectively. This results directly in the most important property of the spin echo, namely that the evolution of the isotropic chemical shift is refocussed at the end of the second delay τ . For solid samples under MAS, it is vital that each

half-echo τ be set to an integer number of rotor periods, usually one, so that the sample rotation refocusses the evolution of the anisotropic interactions within each half echo. This is particularly important for paramagnetic systems with large SAs, as any small miscalibration in the delays can lead to significant errors due to net evolution of the SA. Therefore if we begin acquisition immediately after this echo the resulting spectrum contains no frequency-dependent phase errors due to evolution of the chemical shift or SA. Both errors would lead to peaks at different positions in the spectrum having different phases. Phase errors due to the SA are particularly serious as they are orientation dependent, and so the spectrum of the powder would exhibit cancellation of intensity from the summation of the crystallites with no signal being seen at all in extreme cases. An additional beneficial property of the spin echo is that signal losses during the echo are not as serious as one would expect given the linewidths in the spectrum. The one-dimensional linewidths are dominated by inhomogeneous broadening, which is due to a distribution of isotropic chemical shifts caused by different local magnetic fields in different parts of the sample. This source of broadening is refocussed by the spin echo, as it behaves as a chemical shift, and so the only sources of signal decay during the echo are from homogeneous effects, such as relaxation and coherent dephasing, which contribute to the time constant T_2' .

These frequency dependent phase errors are often seen in the one-pulse spectra as a result of the receiver dead time δ_{de} , typically of a few μs , that is required between the pulse and acquisition to switch over from transmit to detect mode. In the absence of the dead time, assuming the pulse is of infinite power and zero duration, the beginning of the free-induction decay (FID) is captured during the detection period as shown in Fig. 9(a) for an SA under MAS. The Fourier transform then yields the spectrum in Fig. 9(c) in which the spinning sidebands have the same phase. However if we introduce a dead time during which there is no acquisition, one or more of the data points will be missing from the FID as shown in Fig. 9(b). This is particularly problematic if we employ a large spectral width $\Delta\omega$, which is often needed to capture the full spectra of paramagnetic species, as the sampling interval Δt between data points in the time domain is given by the Nyquist condition $\Delta t = 2\pi/\Delta\omega$ [60], and more points are lost in the dead time. For example if we have a spectral width of 1 MHz, the sampling interval

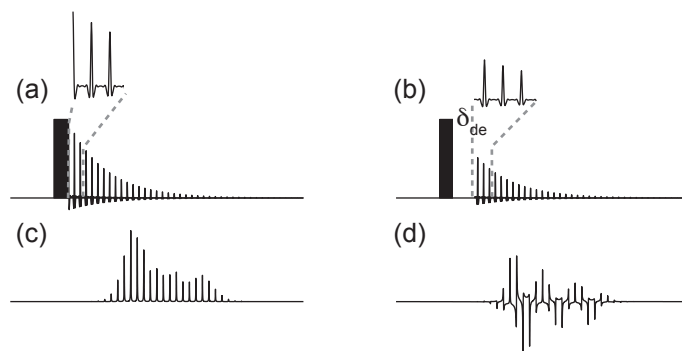


Figure 9: Illustration of the effect of the receiver dead time δ_{de} on broad spectra. In (a) is shown the FID acquired immediately following excitation. The Fourier transform yields the spectrum in (c) in which the sidebands have uniform phase. If we now insert a delay between the pulse and detection period of a few μs , as shown in (b), the resulting spectrum (d) cannot be phased.

is $1.0 \mu s$, and so six points are cut from the beginning of the FID during a dead time of $6.5 \mu s$. The resulting Fourier transform in Fig. 9(d) then shows a large frequency dependent phase error across the spectrum that cannot be removed using a first-order phase correction. The advantage of the spin echo is that the dead time is absorbed into the second half-echo delay τ and so we can acquire the first point of the FID as if δ_{de} were zero.

The shortcomings of the one-pulse sequence are illustrated experimentally on the ${}^7\text{Li}$ and ${}^{31}\text{P}$ spectra of the cathode material $\text{LiFe}_{0.5}\text{Mn}_{0.5}\text{PO}_4$ at 60 kHz MAS shown in Fig. 10(a) and Fig. 10(c). Both spectra exhibit large frequency-dependent phase errors, and the ${}^{31}\text{P}$ spectrum also has a very low signal-to-noise ratio. In the spin echo experiment the dead time is absorbed into the second half-echo delay, and so we see a substantial improvement for ${}^7\text{Li}$ as shown by the spectrum in Fig. 10(b) which can be phased so that the sidebands have the same phase. In addition the sideband manifold has been excited uniformly as will be discussed in more detail below and in subsequent sections. The spin-echo spectrum of ${}^{31}\text{P}$ in Fig. 10(d) also shows improvement in the form of a much higher signal-to-noise ratio better phase properties. However the excitation window has been reduced by the inclusion of the 180° pulse which has a comparatively narrow bandwidth compared to the 90° pulse as discussed in Section 6.1. Simulations of the excitation and inversion profiles of the excitation and refo-

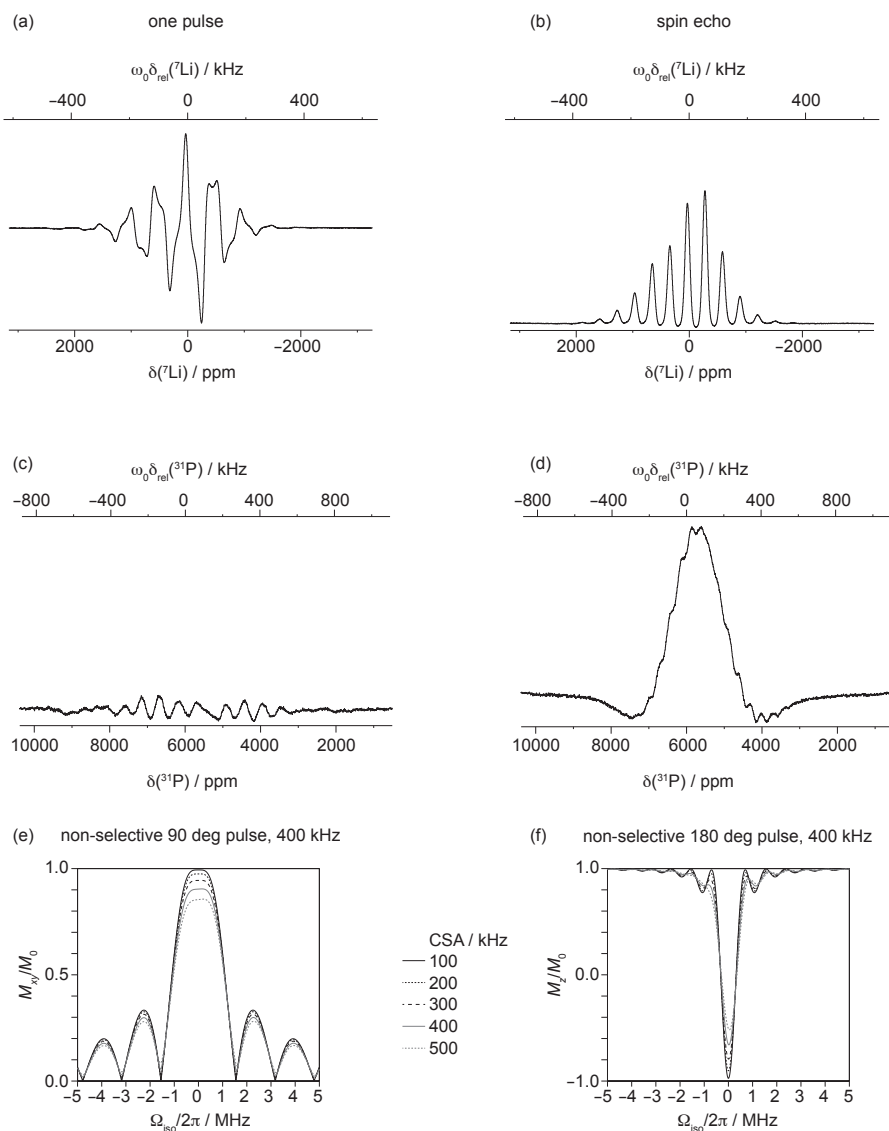


Figure 10: Experimental one-pulse and spin-echo spectra of the cathode material $\text{LiFe}_{0.5}\text{Mn}_{0.5}\text{PO}_4$ at 11.74 T and 60 kHz MAS. The one-pulse ($0.55 \mu\text{s}$ at 455 kHz RF field amplitude) ${}^7\text{Li}$ spectrum with 8192 scans is shown in (a), and exhibits poor phase. Using a spin-echo pulse sequence gives the spectrum in (b) with uniform phase. The reduced excitation bandwidth of the spin echo presents no problems because the isotropic chemical shifts of the different sites lie within a range of 60 kHz. The one-pulse ($0.60 \mu\text{s}$ at 417 kHz RF field amplitude) ${}^{31}\text{P}$ spectrum with 32768 scans has very poor sensitivity and phase, as shown in (c). Use of the spin echo gives some improvement in the phase across the spectrum, and a much better signal-to-noise ratio, but at the expense of excitation bandwidth as the isotropic shifts cover a range of 800 kHz. The spectra in (a)–(d) have been plotted against both chemical shift and frequency scales. For the latter the frequency is calculated as $\omega_0 \delta_{\text{rel}}$, where δ_{rel} is the chemical shift measured relative to 0 ppm for ${}^7\text{Li}$ and 6000 ppm for ${}^{31}\text{P}$. In (e) and (f) are shown simulations of the excitation profile of a 400 kHz 90° pulse, and the inversion profile of a 400 kHz 180° pulse at 60 kHz MAS for a range of CSAs.

Excitation pulses of 400 kHz RF field amplitude are shown in Fig. 10(e) and Fig. 10(f) respectively. In the absence of an SA the bandwidths are, respectively, $3.16\omega_1$ and $0.46\omega_1$. On including a progressively larger SA, from 100 kHz to 500 kHz, the excitation and inversion profiles maintain the same shape with the most efficient response on resonance with the isotropic shift, but with an overall reduction in the degree of excitation and inversion. For example the excitation of a spin with a 100 kHz SA at 60 kHz MAS with a 400 kHz pulse gives transverse magnetisation M_{xy} that is equal to close its maximum value of the equilibrium magnetisation M_0 . Likewise inversion results in the longitudinal magnetisation M_z close to $-M_0$, i.e. almost 100% inversion. However on increasing the SA to 500 kHz the excitation and inversion efficiencies drop with M_{xy} and M_z being equal to $0.8M_0$ and $-0.5M_0$ respectively.

These simulations illustrate two properties that are observed on comparing conventional excitation and inversion pulses under MAS conditions. Firstly the inversion pulse is less tolerant of a large shift anisotropy than the 90° excitation pulse with the on-resonance inversion efficiency of the former dropping off more rapidly with increasing SA. Secondly we see that both pulses perform better in the presence of an increasing SA, if the isotropic shift is resonant with the carrier, than in the presence of an increasing isotropic offset of comparable magnitude. This intriguing effect arises because the anisotropic component of the shift oscillations back and forth during MAS, passing into and out from the pulse bandwidth. The pulse therefore exerts a procession effect on the spin for a fraction of the time we see some excitation or inversion, which is exactly the effect we quantified in the jolting frame in Section 6.6 [39].

The poor performance of the conventional inversion pulses means that they are the weak link in the spin-echo sequence, and so must be replaced in order to have an experiment that can deliver the broadband excitation properties that we require. Various choices of refocussing pulse are discussed in the following sections, many of which make use of the excitation sculpting principle in the form of a double spin echo. First we will see how the conventional spin echo can be employed to acquire a broadband spectrum by acquiring a number of spectra with different carrier frequencies, a method that is referred to as frequency stepping.

7.2. Frequency stepping

One comparatively simple solution to the problem of broadband excitation is to record a series of spectra in which the carrier frequency is varied with a step size that is smaller than the RF field amplitude. The individual sub-spectra are then summed to give the whole spectrum. This is a method that has been extensively employed both for the NMR of paramagnetic materials and quadrupolar nuclei, and has been referred to a variety of names including “spin-echo mapping” [82–89], “variable offset cumulative spectroscopy” (VOCS) [90–92], and “frequency stepping” [12, 13, 93, 94], and is currently the most widely applicable solution to situations where the anisotropic interaction is sufficiently large to broaden the spectrum so that it is wider than the bandwidth of the probe. Frequency stepping is applicable to static samples, as there is a straightforward relationship between the orientation of a particular crystallite and the chemical shift it gives. There are far fewer examples of its application to spinning samples however, probably because the sample rotation complicates the theoretical treatment of the spin dynamics [38], and special care must be taken to ensure that the final spectrum is an accurate representation of the “true” spectrum. Nevertheless it is possible to apply frequency stepping successfully to spinning samples [17, 95].

The concept of frequency stepping under MAS conditions is illustrated in Fig. 11, where the aim is to acquire the spinning sideband manifold in the reference spectrum in Fig. 11(a) by recording a series of sub-spectra with the carrier frequency tuned to different frequencies as indicated by the arrows. The arrows could either represent single-sideband-selective excitation pulses that are applied to each sideband in turn, or to higher-power selective pulses applied with a larger frequency step size. The sub spectra in Fig. 11(b) are then summed to give a sum spectrum that should ideally be in excellent agreement with the reference spectrum.

Recently a complete theoretical treatment of frequency stepping applied to spinning solids has been published which is based on the jolting frame formalism presented in Section 6.6 [18]. Frequency stepping by applying single-sideband-selective excitation pulses, which satisfy the low-power condition $\omega_1 \ll \omega_r$, was first analysed as the treatment is relatively straightforward. The concept was then extended to higher-power pulses, such that several sidebands lie within the excitation bandwidth of the pulse,

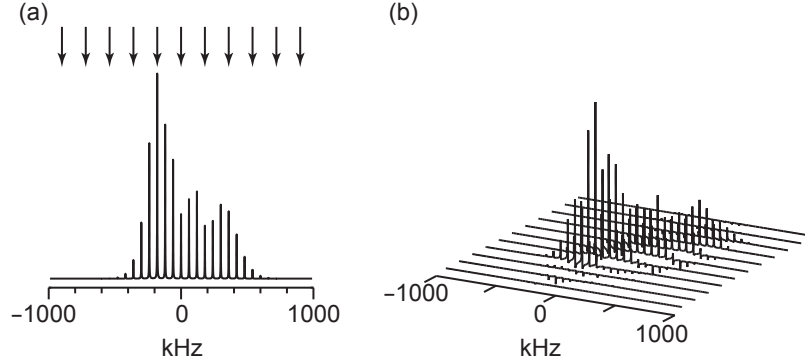


Figure 11: Illustration of the concept of frequency stepping under MAS. The aim is to acquire a spectrum exhibiting a broad spinning-sideband manifold, such as that in (a), in a series pieces for which the carrier frequency is tuned to different spectral positions, which are indicated by the arrows. The arrows represent either single-sideband-selective pulses, or higher-power selective pulses with bandwidths containing more than one sideband. The sub-spectra are shown in (b).

which is the usual way of applying frequency stepping in practice. The formalism is summarised below.

The concept of frequency stepping using low-power single-sideband-selective excitation pulses is based on Eq. (120) in Section 6.6, which is repeated here for convenience:

$$\widehat{\mathcal{H}} = \omega_1 A_c^{(n)} \hat{R}_z(\phi_c^{(n)}(\gamma))^{-1} \hat{I}_x \hat{R}_z(\phi_c^{(n)}(\gamma)). \quad (124)$$

This is simply a pulse of RF field amplitude $\omega_1 A_c^{(n)}$ and phase $-\phi_c^{(n)}(\gamma)$. The effect of such a pulse of length τ_p on the equilibrium state of the spin system in a single crystallite is given by applying the propagator of the Hamiltonian in Eq. (120) to the operator \hat{I}_z . The result is calculated from a series of well-known transformation relations [96], giving

$$\hat{I}_z \cos(\omega_1 \tau_p A_c^{(n)}) - \hat{I}_y \sin(\omega_1 \tau_p A_c^{(n)}) \cos(\phi_c^{(n)}(\gamma)) - \hat{I}_x \sin(\omega_1 \tau_p A_c^{(n)}) \sin(\phi_c^{(n)}(\gamma)). \quad (125)$$

The part that is observable under quadrature detection has coherence order -1 , and is represented by the operator \hat{I}_- . From Eq. (125) the observable term, for a single

crystallite, following irradiation with a single-sideband-selective pulse is therefore

$$-\frac{1}{2}i \sin(\omega_1 \tau_p A_c^{(n)}) \exp(-i\phi_c^{(n)}(\gamma)) \hat{I}_-, \quad (126)$$

where we note that the coherence has acquired an orientation-dependent phase $-\phi_c^{(n)}(\gamma)$.

This observable evolves during acquisition to give a sideband manifold:

$$\begin{aligned} s_c^{\text{ssb}}(\gamma; t) &= \sin(\omega_1 \tau_p A_c^{(n)}) \exp(-i\phi_c^{(n)}(\gamma)) \exp(i\Phi_c^{\text{SA}}(\gamma; t, 0)) \\ &= \sin(\omega_1 \tau_p A_c^{(n)}) \sum_{m=-\infty}^{+\infty} A_c^{(m)} \exp[i(\phi_c^{(m)}(\gamma) - \phi_c^{(n)}(\gamma))] \exp(im\omega_r t), \end{aligned} \quad (127)$$

where we have ignored the factor of $-\frac{1}{2}i$ and expanded the phase factor $\exp(i\Phi_c^{\text{SA}}(\gamma; t, 0))$ as a Fourier series following Eq. (26). The sideband intensities are the same as those following non-selective excitation, and the sideband phases are offset by minus the phase of the irradiated sideband. This means that the irradiated sideband is always excited with zero phase which has very important consequences for the spectrum arising from the powder as we will now see.

Ultimately we are interested in whether the frequency stepping method is able to faithfully reproduce the proper sideband intensities in the manifold of a powder sample. This can be calculated in a straightforward manner by following the protocol outlined in Section 5.2. We firstly substitute the expressions for the sideband intensities and phases in Eq. (34) to obtain

$$s_c^{\text{ssb}}(\gamma; t) = \sin(\omega_1 \tau_p A_c^{(n)}) \sum_{m=-\infty}^{+\infty} A_c^{(m)} \exp[i(\phi_c^{(m)}(0) - \phi_c^{(n)}(0))] \exp[i(m-n)\gamma] \exp(im\omega_r t), \quad (129)$$

and average over γ to obtain the spectrum from the carousel, which is

$$\overline{s_c^{\text{ssb}}(t)} = \sin(\omega_1 \tau_p A_c^{(n)}) A_c^{(n)} \exp(in\omega_r t). \quad (130)$$

We see that only the irradiated sideband is present, with intensity $\sin(\omega_1 \tau_p A_c^{(n)}) A_c^{(n)}$ and phase zero. The factor of $\sin(\omega_1 \tau_p A_c^{(n)})$ in the intensity is simply due to the effective flip angle of the pulse $\omega_1 \tau_p A_c^{(n)}$ which, as we have already pointed out, is scaled by

$A_c^{(n)}$. If the pulse is calibrated so that this flip angle is $\pi/2$, then the intensity of the sideband is $A_c^{(n)}$ rather than $[A_c^{(n)}]^2$ which we obtain following non-selective excitation. As already intimated, this is a consequence of the irradiated sideband being excited with the same phase for each crystallite, whereas all the other sidebands are excited with different phases that cancel on summing over the whole carousel. Finally the powder average is obtained by summing over all the carousels, giving

$$s^{\text{ssb}}(t) = I_n^{\text{ssb}} \exp(in\omega_c t), \quad (131)$$

where

$$I_n^{\text{ssb}} = \frac{1}{4\pi} \int_0^{2\pi} d\alpha \int_0^\pi d\beta \sin(\beta) \sin(\omega_1 \tau_p A_c^{(n)}) A_c^{(n)}. \quad (132)$$

In order to obtain the entire sideband manifold, one simply tunes the RF carrier frequency to each sideband in turn, acquires each single-sideband sub-spectrum following single-sideband irradiation with a low-power pulse, and then sums the result to obtain the “sum spectrum”. The question now remains as to whether the sideband manifold in the sum spectrum is a faithful reproduction of what would be obtained in the “true spectrum”. A simulated comparison is shown in Fig. 12 for nominal flip angles $\omega_1 \tau_p$ of 90° , 50° , and 10° . The single-sideband sub spectra in Fig. 12(a) are summed to give the sum spectra in Fig. 12(b). It can be seen that each sum spectrum shown matches the reference spectrum, also shown in Fig. 12(b), to a very good approximation, which can also be appreciated from the difference between the sum and reference spectra, following a scaling of the former so that the global intensities match in Fig. 12(c). It can be seen that there is better agreement when one uses a smaller flip angle, an observation that can be rationalised as follows. We have already seen that the intensity of the n th-order sideband in carousel c is $C_n = [A_c^{(n)}]^2$, whereas in the sum spectrum it is $C_n^{\text{ssb}} = \sin(\omega_1 \tau_p A_c^{(n)}) A_c^{(n)}$. The quality of the agreement between the two spectra depends on how good a match C_n^{ssb} is to C_n . If the combination of the sideband intensity and nominal flip angle satisfies $\omega_1 \tau_p A_c^{(n)} \ll 1$ the sine function can be approximated as

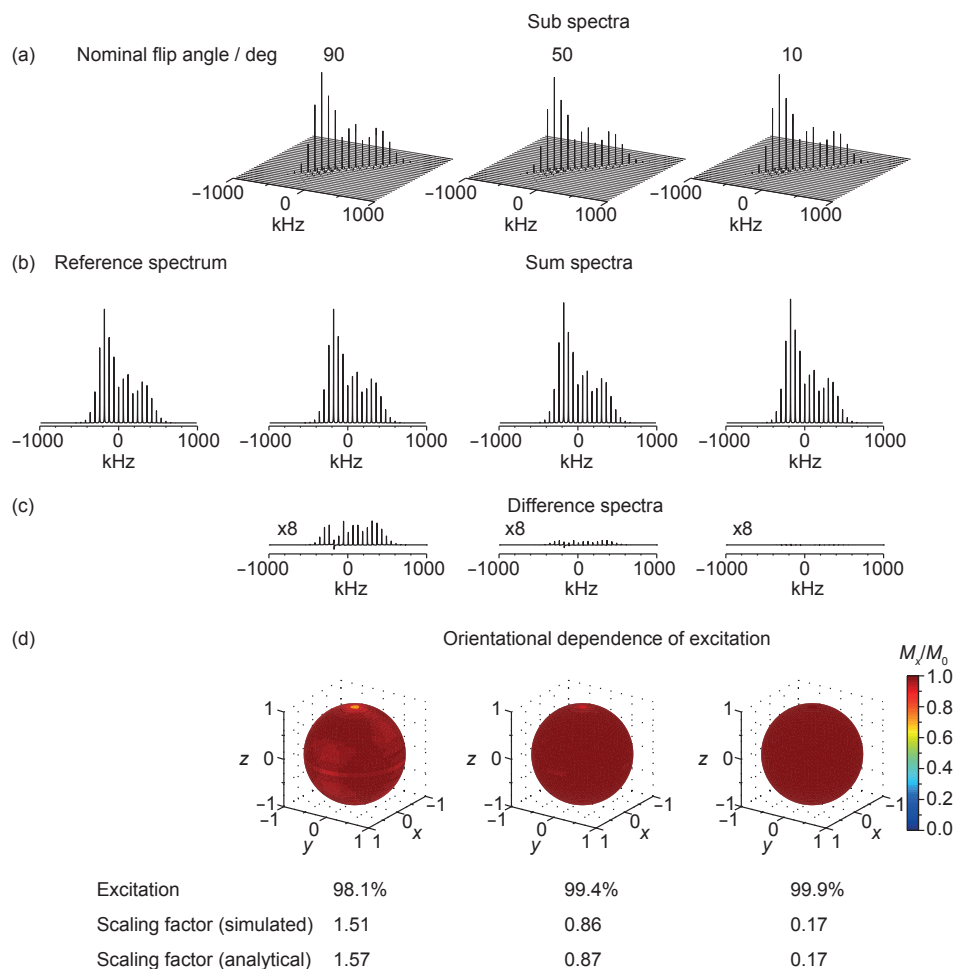


Figure 12: Simulation of single-sideband-selective frequency stepping. Shown in (a) are the 32 sub-spectra that were simulated using a single excitation pulse of length $125 \mu\text{s}$ for three nominal flip angles of 90° , 50° , and 10° . The nominal flip angle was varied by scaling the RF field, which took the values 2.00, 1.11, and 0.22 kHz, respectively. The spectra formed by summing the sub-spectra are shown in (b) with the reference spectrum that was simulated with non-selective excitation. The differences between the reference and sum spectra are illustrated in (c) which shows the difference spectra (sum spectrum–scaled reference spectrum) for each case. Note that the vertical scale in these three plots is expanded by a factor of 8. The orientational variation of excitation efficiency is shown by the sphere plots below each difference spectrum in (d). Each point on the surface of the sphere corresponds to the orientation of a particular carousel with Euler angles (α, β) , and the axis labels (x, y, z) are the spatial Cartesian coordinates corresponding to these Euler angles, and do not refer to the axis of the magnetization. The colour of each point on the surface gives the size of the x -magnetization that is generated overall for each carousel of this orientation on summing the sub-spectra (the y -magnetization is zero in all cases). The calculated expectation values of \hat{I}_x were normalized by dividing by the greatest value of the scaling factor F_c , the values of which are given below each sphere. The normalized expectation values were then summed to give the total percentage excitation obtained with each of the three flip angles. For comparison analytical value of the maximum scaling factor (θ in radians) is also given. The shift tensor parameters are: isotropic shift 0 kHz, CSA +500 kHz, asymmetry parameter 0.3, with an MAS frequency of 60 kHz. Reproduced with permission from Ref. [18]. Copyright 2013 American Institute of Physics.

a Taylor series giving

$$C_n^{\text{ssb}} \approx \omega_1 \tau_p [A_c^{(n)}]^2 \quad (133)$$

$$= \omega_1 \tau_p C_n. \quad (134)$$

From this we would expect the pattern of *relative* sideband intensities to match those in the reference spectrum if $\omega_1 \tau_p A_c^{(n)} \ll 1$ is satisfied for all the sidebands in the manifold for each carousel, hence the better agreement for a smaller nominal flip angle $\omega_1 \tau_p$. One can also define a scaling factor F_c which is a measure of the size of the transverse magnetisation represented by the sum spectrum as compared to a reference spectrum requiring the same acquisition time as each sub spectrum. For a particular carousel this scaling factor is given by

$$F_c = \frac{\sum_m C_m^{\text{ssb}}}{\sum_m C_m} \quad (135)$$

$$= \sum_m C_m^{\text{ssb}}, \quad (136)$$

recalling that $\sum_m C_m = \sum_m [A_c^{(m)}]^2 = 1$ as the Fourier coefficients are normalised. If the small flip angle approximation is met the scaling factor becomes

$$F_c \approx \omega_1 \tau_p \sum_m C_m \quad (137)$$

$$= \omega_1 \tau_p, \quad (138)$$

which is simply the value of the nominal flip angle in radians. Fig. 12 shows the comparison between the scaling factor calculated from the simulations and the value expected from Eq. 138. The agreement for flip angles below 50° is excellent, and even for a flip angle of 90° the error is less than 4%.

The extent of the agreement between the relative sideband intensities is related to the uniformity of the size of the excited transverse magnetisation as a function of crystallite orientation. Fig. 12(d) shows the size of the transverse magnetisation vector, that is excited for each carousel as a function of the Euler angles (α, β) . The plots have

been normalised by dividing the size of the magnetisation by the scaling factor so that the results lie between 0 and 1. It can be seen that the uniformity increases with decreasing flip angle, and that we have a small increase in the the degree of excitation from 98.1% to 99.9% on reducing the flip angle from 90° to 10° , which matches the better agreement of the relative sideband intensities with the reference spectrum. Nevertheless the overall signal-to-noise ratio decreases as we reduce the nominal flip angle from 90° , and since we still see an impressive result for a 90° pulse, it is preferable to use a large flip angle in order to maximize the sensitivity. This approach has been used successfully on the battery material LiMnPO_4 [18].

The use of single-sideband-excitation pulses for frequency stepping has a number of disadvantages that render the method impractical. Firstly, one has to be able to obtain near-baseline resolution of the individual sidebands in the spectrum so that only a limited degree of inhomogeneous broadening can be tolerated. This condition may not be met for many paramagnetic samples as effects such as anisotropic bulk magnetic susceptibility (ABMS) [97] and temperature gradients may lead to a large degree of broadening. Secondly, for large SAs giving rise to a large number of sidebands, stepping through the spectrum one sideband at a time will be time consuming and tedious. Thirdly, for samples containing more than one crystallographic site it may be necessary to step through each spinning sideband manifold independently. Fortunately these problems can be circumvented by using pulses with higher RF field amplitudes which are no longer sideband selective. These so-called “selective pulses” (as opposed to single-sideband selective) excite a portion of the spectrum containing a number of spinning sidebands within the excitation profile of the pulse. The higher RF field amplitude allows one to increase the step size of the carrier frequency and obtain a sum spectrum with fewer sub spectra. In this regime the intensities of the sidebands in each sub-spectrum matches the sinc excitation profile of the pulse as shown by the simulation in Fig. 13. The reference spectrum in Fig. 13(a) is compared with the spectrum acquired using frequency stepping with an RF field amplitude of 200 kHz, and a step size of the carrier frequency of 180 kHz corresponding to every third sideband. The eleven sub-spectra are shown in Fig. 13(b), and were summed to give the sum-spectrum in Fig. 13(c). The arrows in Fig. 13(c) show the positions of the carrier for each sub-

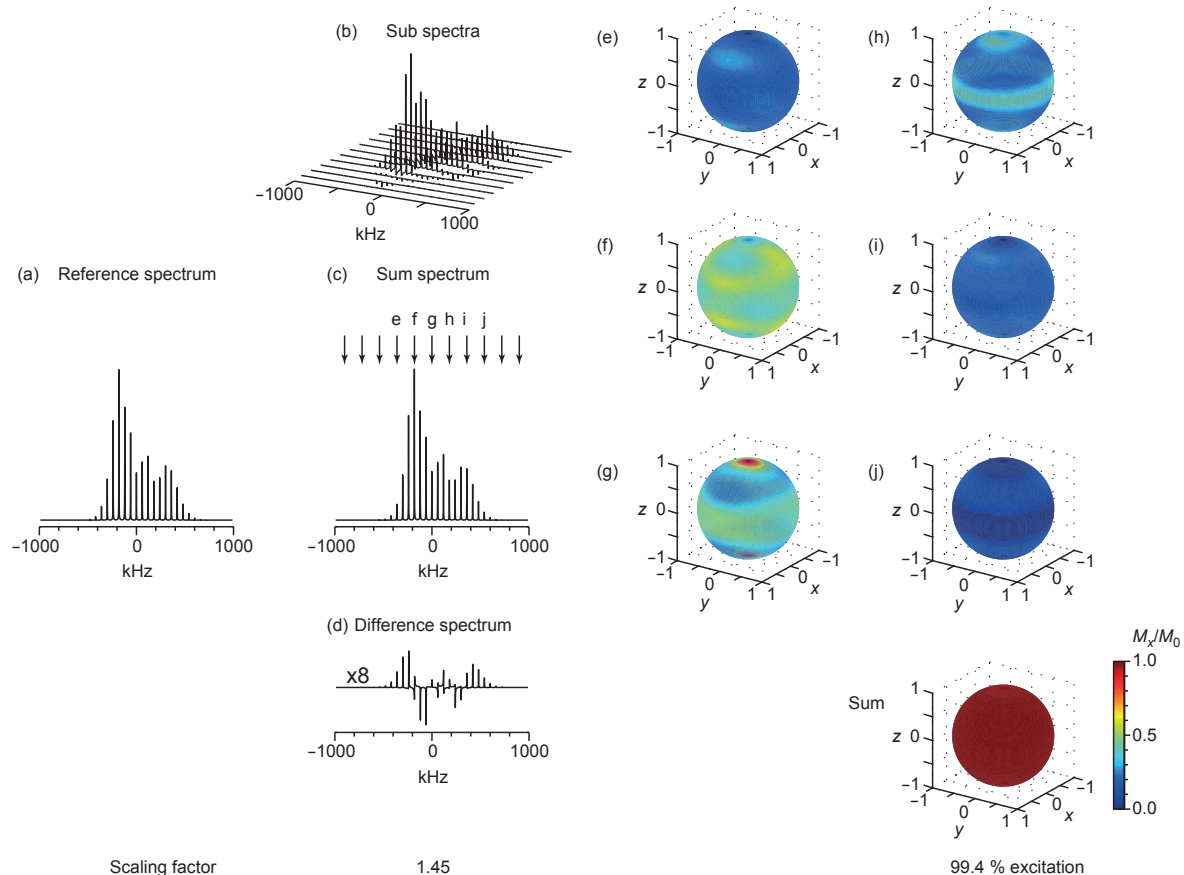


Figure 13: Simulations illustrating the method of frequency stepping under ultra-fast MAS conditions. The reference spectrum is shown in (a). Frequency stepping was performed using a spin-echo pulse sequence of the form $90^\circ(y) - \tau - 180^\circ(x) - \tau$, with EXORCYCLE applied to the second pulse, in which the RF field of the pulses was 200 kHz, and τ was $48.75 \mu\text{s}$ (so that the sum of τ and half the 180° pulse length was three rotor periods.) The eleven sub-spectra shown in (b) were simulated with the RF carrier frequency being varied from -900 to $+900$ kHz in steps of 180 kHz (every three sidebands), and were summed to give the sum-spectrum in (c). The intensity of the sum-spectrum is scaled by a factor of 1.45 due to the overlap between the sub-spectra of the neighbouring steps. The arrows on the spectrum in (c) indicate the positions of the carrier frequency for each experiment; those labelled (e)–(j) correspond to the experiments in which part of the resonance was excited. The differences between the reference and sum spectra are illustrated in (d) which shows the difference spectrum (sum spectrum–scaled reference spectrum). Note that the vertical scale in this plot is expanded by a factor of 8. The degree of excitation as a function of (α, β) is shown for each with a spherical intensity plot, which shows the x -magnetization generated for each orientation (the y -magnetization was zero for all cases). Below is the plot indicating the total excitation for the sum of all the spheres (e)–(j). The shift tensor parameters are: isotropic shift 0 kHz, CSA +500 kHz, asymmetry parameter 0.3, and the MAS frequency was 60 kHz. Adapted with permission from Ref. [18]. Copyright 2013 American Institute of Physics.

spectrum. The sum-spectrum shows a greater degree of deviation from the reference spectrum compared to those acquired using single-sideband-selective excitation pulses, as shown by the difference which is plotted in Fig. 13(d). Nevertheless the agreement in the pattern of sideband intensities is still excellent.

One must take great care when summing the sub-spectra. If one attempts to phase each individual sub-spectrum by applying a frequency-dependent phase correction the resulting sum is a poor representation of the true sideband manifold. This is because in order to sum the sinc-function envelopes properly there must be some cancellation of the negative and positive intensities in the ‘wiggles’ flanking the lobe part of the function. This effect can be obtained simply by applying a *frequency-independent* phase correction to phase the part of the spectrum that is resonant with the carrier and then summing.

The extent to which the different crystallite orientations were excited at each carrier frequency is shown by the six sphere plots in (e)–(j), where each point on the sphere represents the x -magnetization excited from each carousel with Euler angles (α, β) . The sum of these spheres shows that the sum spectrum represents an overall excitation of 99.4% uniformity.

In summary, frequency stepping is a valuable technique for obtaining a one-dimensional spectrum in cases where the range of shifts and SAs is too large to be excited with practicable RF field amplitudes, and especially when they are broader than the bandwidth of the probe. The increased complexity of the frequency stepping method when applied to spinning systems, including the correct way to sum the individual sub-spectra, has resulted in a comparative paucity of applications in the literature. However it is not always straightforward to incorporate this method into more sophisticated experiments as firstly we are not able to manipulate the entire spin system in a single experiment, and secondly the time-consuming nature of the method means that its inclusion in two- and three- dimensional pulse sequences would create an experiment that is prohibitively long. Nevertheless there are several notable examples [17, 18, 36, 95] and it is expected that, with the increasing interest in the NMR of paramagnetic systems, that there will be more applications in the future.

7.3. *Broadband inversion and refocussing with Short, High-power Adiabatic Pulses (SHAPs)*

In order to use more sophisticated two- and three-dimensional experiments it is necessary to have a pulse scheme that manipulates the entire spin system, which can be incorporated into more complex experiments. In the last few years adiabatic pulses have been employed both for broadband inversion and refocussing of spin systems subject to large paramagnetic interactions under MAS. In this section we shall look at the class of pulses referred to as Short, High-Power Adiabatic Pulses (SHAPs) [19]. These pulses are designed to achieve broadband inversion with a “brute force” approach in which the carrier is swept through the entire spectrum in a relatively short time using a high RF field amplitude to satisfy the adiabatic condition $Q^{(1)} \gg 1$, where the quality factor $Q^{(1)}$ is defined in Eq. (64).

There are two important criteria that need to be fulfilled for a successful SHAP: (1) the carrier must sweep through a range of frequencies that is greater than the width of the spectrum, (2) the RF field amplitude must be sufficiently large to ensure that the pulse is adiabatic. If the above conditions are met we can shorten the pulse length to reduce losses through relaxation and coherence dephasing, which is particularly important when the system is subject to a large PRE. The reason behind criterion (1) is that the large offsets are needed at the edges of the sweep to dominate the SA interaction as this is where the RF field amplitude is lowest. This is usually achieved by choosing a sweep width that is much greater than the width of the spectrum but still within the probe bandwidth, for example in the range 1–10 MHz [19]. For all adiabatic pulses the large increase in bandwidth compared to the RF field amplitude must be bought at the price of a pulse length that is longer than conventional high-power pulses.

The RF field amplitudes that are needed to adiabatically invert a spin system exhibiting a large SA are typically larger under MAS compared to static conditions. A wide range of adiabatic pulse forms can be adapted to serve as successful SHAPs including, but not limited to, those given in Table 1. The pulse that has so far been used most extensively and successfully is the tanh/tan of Hwang et al. [43] which is already used in MRI to invert over a large frequency range in a short time [62]. The tanh/tan pulse is certainly more suited for fast broadband inversion and refocusing over

a wide range of frequencies than either the WURST or hyperbolic secant pulses, as we can appreciate when we note that a tanh/tan pulse requires a minimum peak RF field amplitude of 70 kHz to achieve adiabatic inversion with a 5 MHz sweep in 50 μ s under static conditions, compared to 400 kHz for a WURST pulse. Nevertheless we do not exclude other pulse waveforms as being possible candidates for SHAPs in future applications.

The theoretical description of a swept-frequency adiabatic pulse applied to a spin with a varying chemical shift has already been completely set down in Section 6.2 where, it must be remembered, we made no assumptions about the form of the time-dependence of the chemical shift. In order to describe the effect of *any* adiabatic pulse applied to a spinning solid we simply take all the equations in that section and replace the time-dependent offset $\Omega(t)$ with the explicit expression for an SA subject to MAS as given in Eq. (13). The offset $\Omega(t)$ is the sum of the isotropic and SA terms which, when combined with the RF field, results in an effective field $\omega_{\text{eff,c}}^{(0)}(\gamma; t)$ and tilt angle $\dot{\theta}_c^{(0)}(\gamma; t)$ equal to

$$\omega_{\text{eff,c}}^{(0)}(\gamma; t) = \sqrt{\left(\Omega_{\text{iso}} + \Omega_c^{\text{SA}}(\gamma; t) - \omega_{\text{rf}}\right)^2 + \omega_1(t)^2}, \quad (139)$$

$$\dot{\theta}_c^{(0)}(t) = \frac{\dot{\omega}_1(t) \left[\Omega_{\text{iso}} + \Omega_c^{\text{SA}}(\gamma; t) - \omega_{\text{rf}}(t) \right] - \omega_1(t) \left[\dot{\Omega}_c^{\text{SA}}(\gamma; t) - \dot{\omega}_{\text{rf}}(t) \right]}{\omega_{\text{eff,c}}^{(0)}(\gamma; t)^2}. \quad (140)$$

In order to determine the inversion performance of the SHAP we must determine the point during the pulse where the ratio $\left| \dot{\theta}_c^{(0)}(\gamma; t) / \omega_{\text{eff,c}}^{(0)}(\gamma; t) \right|$ is largest, as this is where the adiabatic condition is most likely to be violated, giving the value of $1/Q^{(1)}$:

$$\frac{1}{Q^{(1)}} = \max \left| \frac{\dot{\omega}_1(t) \left[\Omega_{\text{iso}} + \Omega_c^{\text{SA}}(\gamma; t) - \omega_{\text{rf}}(t) \right] - \omega_1(t) \left[\dot{\Omega}_c^{\text{SA}}(\gamma; t) - \dot{\omega}_{\text{rf}}(t) \right]}{\omega_{\text{eff,c}}^{(0)}(\gamma; t)^3} \right|. \quad (141)$$

Compared to the static case described in Section 6.2, for a solid subject to large paramagnetic interactions under MAS we must consider the effect of the time-dependent SA

$\Omega(t)$, which is given by $\Omega_c^{\text{SA}}(\gamma; t)$ in Eq. (13), and its derivative, which is given by

$$\dot{\Omega}_c^{\text{SA}}(\gamma; t) = -i\omega_r \sum_{k=-2, k \neq 0}^{+2} k\omega_c^{(k)}(\gamma) \exp(-ik\omega_r t). \quad (142)$$

Both of these factors are extremely important when we determine whether or not the pulse is adiabatic, as the modulation of the SA will cause both the magnitude and tilt angle of the effective field to change rapidly which will have the effective of reducing $Q^{(1)}$ and thus weaken the adiabaticity. In particular we would expect the rapid oscillation of the SA to dominate the z -component of the effective field when the carrier is on resonance with the isotropic shift. These effects can be seen in Fig. 14 which show simulations of the magnetisation trajectories of a spin subject to a 200 kHz SA during application of a SHAP at 60 kHz MAS for a single crystallite, the carousel, and the whole powder. The single crystallite spectrum is shown in Fig. 14(a). During the pulse the z -component of the magnetisation vector, shown in Fig. 14(b) exhibits the expected oscillations due to the modulation of the SA by MAS which are superimposed upon the inversion. The resulting magnetisation pathway, shown in Fig. 14(c), is rather complicated, and exhibits a number of crossings through the xy plane, five in this case, rather than the single one that would be observed in the absence of the sample rotation. When we perform the average over γ , giving the spectrum in Fig. 14(d), we see that the oscillations in the magnetisation trajectory are cancelled, as shown in the plots in Fig. 14(e) and Fig. 14(f). This is because each crystallite in the carousel has the same time variation of the chemical shift, but with different initial phases that depend on γ , which follows directly from Eq. (21) and Eq. (30). The trajectories for the full powder are also shown in Fig. 14(h) and Fig. 14(i). That the adiabaticity of the pulse is weakened by MAS can be seen from the necessity of using an RF field amplitude of 400 kHz for inversion rather than the 70 kHz required for the same pulse on a static system. This is illustrated by Fig. 15 where the inversion trajectories of crystallites with different β values, their respective carousels, and the whole powder is illustrated in for two SHAPs with RF field amplitudes of 150 and 400 kHz respectively. The magnetization pathways at 150 kHz RF field amplitude show, in many cases, imperfect inversion indicating a

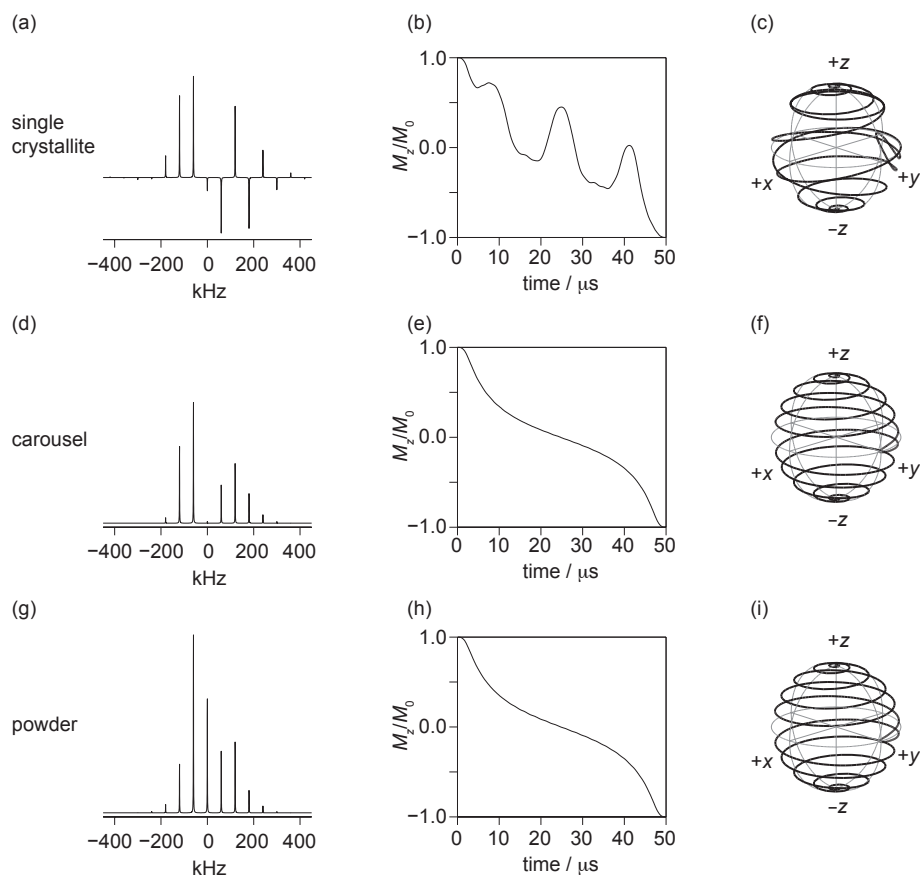


Figure 14: Simulation of the magnetization trajectory of a spin subject to a large shift anisotropy under MAS during a SHAP [19]. Trajectories are shown for a single crystallite (a)–(c), the average over a whole carousel (d)–(f), and the entire powder (g)–(i). The simulated spectrum of the single crystal at orientation $(\alpha, \beta, \gamma) = (0^\circ, 50^\circ, 0^\circ)$ is shown in (a). The z -component of the magnetization during the SHAP is shown in (b), exhibiting perturbations away from the usual smooth inversion pathway due to the modulation of the CSA during MAS. In (c) is shown the entire trajectory in three-dimensional space. The spectrum of the carousel $(\alpha, \beta) = (0^\circ, 50^\circ)$, representing the average over the angle γ is shown in (d). The corresponding z -magnetization and magnetization trajectory are shown in (e) and (f) respectively. The oscillations that were present in the single crystal plots (b) and (c) have now been averaged out, leaving the smooth inversion pathways. Finally, the simulated spectrum of the powder is shown in (g), with the plots of the z -magnetization and magnetization trajectory in (h) and (i). The shift tensor parameters are: isotropic shift 0 kHz, CSA +200 kHz, asymmetry parameter 0.3, and the MAS frequency was 60 kHz. The SHAP [19] was a tanh/tan pulse [43] which swept through 5 MHz in 50 μ s at an RF field amplitude of 400 kHz.

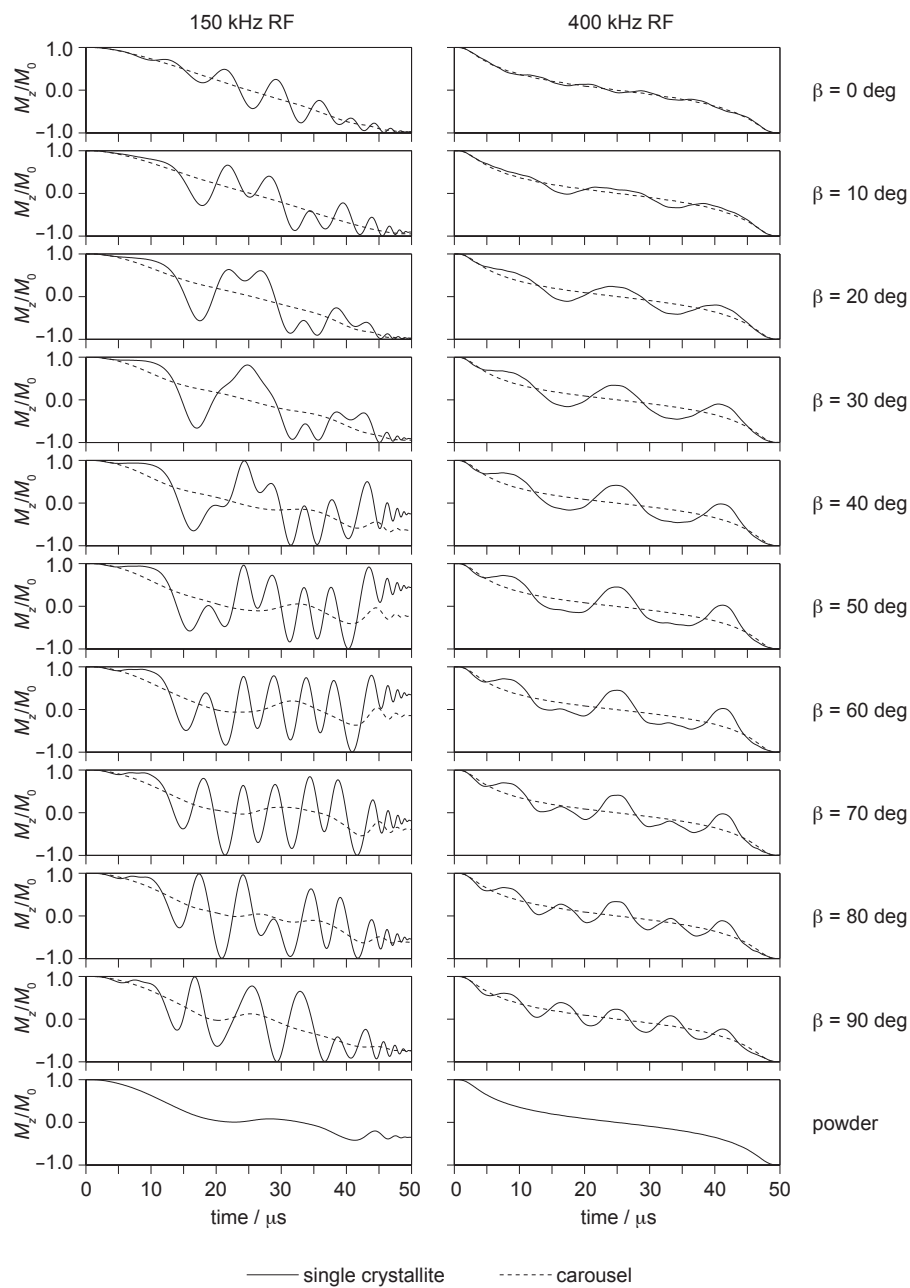


Figure 15: Comparison of simulated inversion trajectories due to a SHAP under MAS at two different RF field amplitudes and for different crystallite orientations. The shift tensor parameters are: isotropic shift 0 kHz, CSA +200 kHz, asymmetry parameter 0.3, and the MAS frequency is 60 kHz. The SHAP is a tanh/tan pulse which sweeps through 5 MHz in 50 μ s at an RF field amplitude of 150 kHz (left-hand column) and 400 kHz (right-hand column). Simulated results are shown for a range of ten values of β from 0° to 90° in steps of 10°; $\alpha = \gamma = 0^\circ$. The inversion pathways are shown for the single crystallite (full line), and the carousel (dashed line).

breakdown of the adiabatic approximation. This results in a powder spectrum which is incompletely inverted, and therefore a distorted spectrum. However, on increasing the RF field amplitude to 400 kHz we observe 100% inversion for all crystallites.

Fast MAS also weakens the adiabaticity of the pulse, as can be seen from Fig. 16. For each of five values of the SA, ranging from 100 to 500 kHz, is shown a contour plot giving the extent of inversion following a tanh/tan SHAP as a function of RF field amplitude and MAS frequency. These show that, for a given SA under a low MAS frequency inversion can be achieved for a relatively low RF field amplitude that is close to the value under static conditions. In addition for faster MAS, or larger SA, a greater RF power is needed for adiabatic inversion. This is shown clearly in the cross sections below the contour plots. The graph in Fig. 16(b) gives the RF field profile of the pulse at 60 kHz MAS for the five values of the SA, and the plot in Fig. 16(c) shows that, for a given RF field amplitude of 400 kHz the degree of inversion becomes lower at higher MAS frequencies, and that the deterioration is greater as the SA increases. This behaviour is expected if we consider Eq. (142) which indicates that the rate of change of the SA frequency during MAS is proportional to the product of the spinning frequency and anisotropy $|\omega_r \omega_0 \Delta\sigma|$, and so we would expect the weakening of the adiabaticity of the pulse to be exacerbated for large SAs and faster MAS. For example, for a 200 kHz CSA it can be seen that the RF field amplitude required to achieve adiabatic inversion increases from 210 kHz at 20 kHz MAS to 550 kHz at 100 kHz MAS.

The magnetisation trajectories can be calculated accurately in the first adiabatic frame from Eq. (71). This can be seen in Fig. 17 which shows a comparison of the simulated and analytical variation of the x -, y -, and z -components of the magnetisation during a SHAP at 20, 40, 60, 80, and 100 kHz MAS for a single crystallite containing a spin subject to a 200 kHz SA. This proves that the inversion is adiabatic and can be described in the first adiabatic frame for a sufficiently large RF field amplitude.

We give an experimental example of the application of SHAPs to the NMR of paramagnetic materials from the field of energy storage. Fig. 18 shows confirmation of the performance of a tanh/tan SHAP when applied to the battery cathode material $\text{LiFe}_{0.5}\text{Mn}_{0.5}\text{PO}_4$. The ^7Li spectrum in Fig. 18(a) was acquired following a conventional spin echo $90^\circ(x) - \tau_r - 180^\circ(x) - \tau_r - \text{aqu.}$ at 60 kHz MAS and an RF field

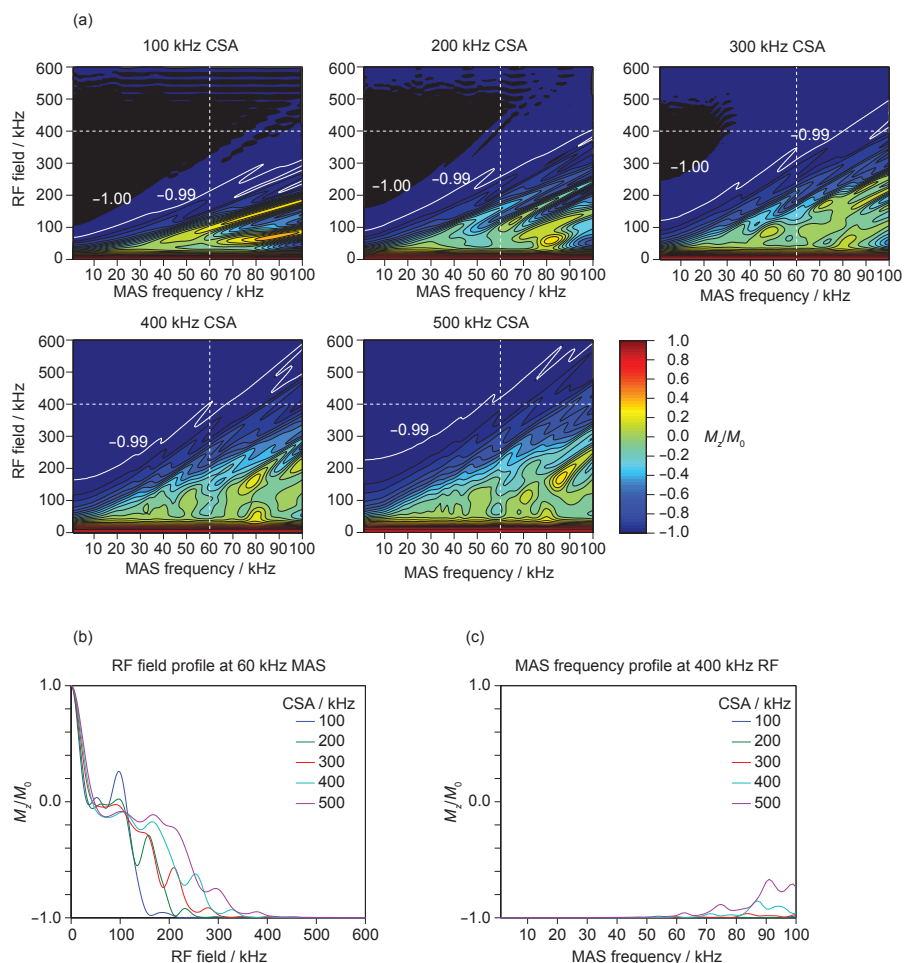


Figure 16: Simulated contour plots showing the inversion performance of a SHAP applied to a spin subject to a large CSA, as a function of RF field amplitude and MAS frequency. In (a) are shown five contour plots for shift anisotropies of 100, 200, 300, 400, and 500 kHz. The contours coloured white indicate exactly 99% inversion, with the inversion performance in the regions at lower MAS frequency and greater RF field amplitude (top left) being better than 99% efficient. The regions exhibiting 100% inversion are coloured black. The vertical white dashed lines indicate where the cross sections in (b) were taken. The cross sections show the dependence of the inversion on the RF field amplitude at 60 kHz MAS for all five values of the shift anisotropy. The cross sections in (c) show the corresponding dependence of the inversion on the MAS frequency at an RF field amplitude of 400 kHz, and are indicated on the contour plots in (a) by the horizontal white dashed lines.

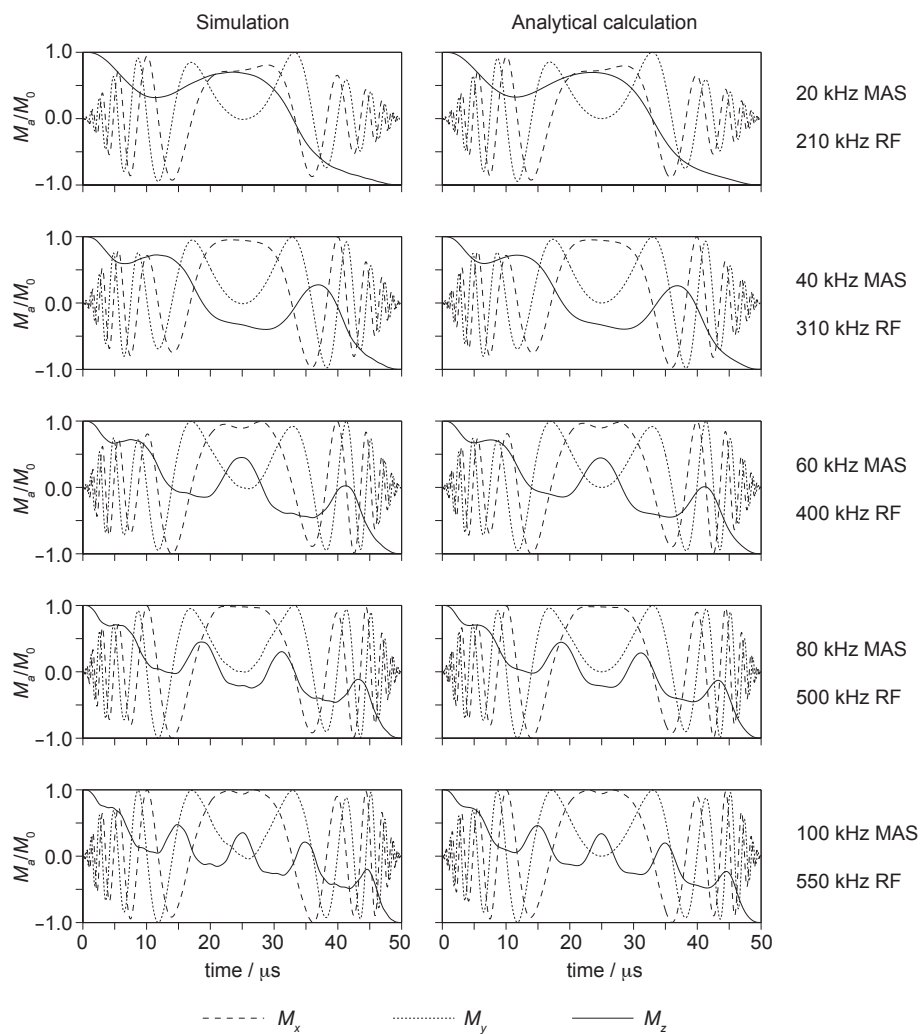


Figure 17: Comparison of simulation and analytical calculation of the inversion trajectories due to a SHAP for a particular crystallite under different MAS frequencies. The shift tensor parameters are: isotropic shift 0 kHz, CSA +200 kHz, asymmetry parameter 0.3, and the MAS frequency takes five values from 20 kHz to 100 kHz in steps of 20 kHz. The SHAP is a tanh/tan pulse which sweeps through 5 MHz in 50 μ s at RF field amplitudes of 210 kHz (20 kHz MAS), 310 kHz (40 kHz MAS), 400 kHz (60 kHz MAS), 500 kHz (80 kHz MAS), and 550 kHz (100 kHz MAS). On the left are shown the simulated trajectories of the x - (dashed line), y - (dotted line), and z -magnetization (full line) of a single crystallite with orientation $(\alpha, \beta, \gamma) = (0^\circ, 50^\circ, 0^\circ)$. The corresponding trajectories calculated from Eq. (71) are shown on the right.

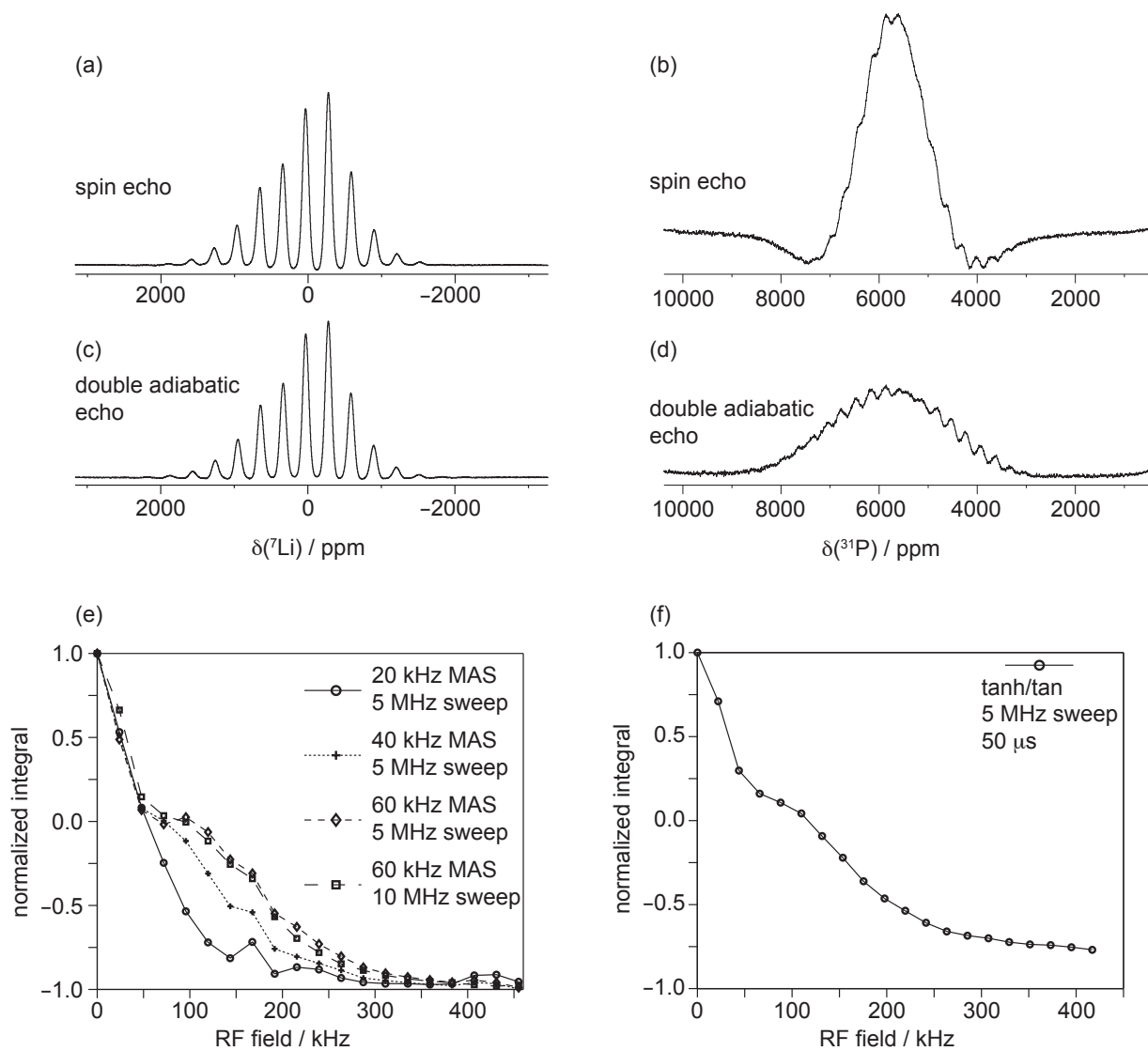


Figure 18: Experimental verification of the inversion and refocussing performance of SHAPs applied to paramagnetic materials. In (a) and (b) are shown the conventional ${}^7\text{Li}$ and ${}^{31}\text{P}$ spin-echo spectra of the cathode material $\text{LiFe}_{0.5}\text{Mn}_{0.5}\text{PO}_4$ at 11.74 T. The RF field amplitudes are 455 kHz for ${}^7\text{Li}$ and 417 kHz for ${}^{31}\text{P}$. The ${}^7\text{Li}$ and ${}^{31}\text{P}$ double SHAP spin echo spectra are shown in (c) and (d), with the latter in particular showing increased excitation bandwidth. The SHAP is a tanh/tan adiabatic pulse sweeping through 5 MHz in 50 μs at RF field amplitudes of 455 kHz for ${}^7\text{Li}$ and 417 kHz for ${}^{31}\text{P}$. Panel (e) shows the integrated intensity of the ${}^7\text{Li}$ spectrum in (c) as a function of RF field amplitude following inversion by a SHAP under different MAS frequencies. The four combinations of SHAP and MAS frequency are: 5 MHz sweep in 50 μs under 20 kHz MAS, 5 MHz sweep in 50 μs under 40 kHz MAS, 5 MHz sweep in 50 μs under 60 kHz MAS, and 10 MHz sweep in 50 μs under 60 kHz MAS. The integrated intensity of the ${}^{31}\text{P}$ spectrum in (d) following SHAP inversion at different RF field amplitudes is shown in panel (f), where the integral represents the sum over all 32 sites over a range of 800 kHz. The SHAP is a tanh/tan adiabatic pulse sweeping through 5 MHz in 50 μs .

amplitude of 455 kHz. It is essentially the same as the spectrum acquired with a double SHAP echo pulse sequence $90^\circ(x) - \tau_r - \text{SHAP} - 2\tau_r - \text{SHAP} - \tau_r - \text{acq.}$ in Fig. 18(c) with the same RF field amplitude. This is because, although there are multiple Li sites, their isotropic shifts are coincident within the inhomogeneous broadening and, with the carrier frequency placed on the centreband, the RF field amplitude of the conventional pulses is sufficient to dominate this distribution. The RF field amplitude is also larger than the SA, and so the excitation bandwidth is sufficient for the efficient excitation of the entire spinning sideband manifolds. In addition the relatively long value of T'_2 of 1.59 ms for ^7Li means that, despite the double SHAP echo pulse sequence being longer than the standard spin echo, there are no additional losses in sensitivity. This is a consequence of the fast spinning frequency of 60 kHz which allows refocusing of the SA time modulation with a short rotor period of 16.67 μs . The experimental RF inversion profiles of SHAPs with 5 and 10 MHz sweep ranges are compared at MAS frequencies of 20, 40, and 60 kHz in Fig. 18(e). These profiles provide experimental confirmation of the observation in the simulations of Figure 16 that faster MAS requires higher RF field amplitudes to achieve inversion. Secondly Fig. 18(e) shows that a 10 MHz sweep at 60 kHz MAS requires the same RF field amplitude as a 5 MHz sweep for inversion despite the sweep rate being twice as large in the former. This has been confirmed by simulation and is ascribed to the rate of change of the tilt angle of the effective field being dominated by the time modulation of the SA and not to the rate at which the carrier frequency is swept as is the case under static conditions.

The real power of the SHAP becomes apparent when we compare the standard spin-echo and double SHAP spin-echo spectra of ^{31}P in Fig. 18(b) and Fig. 18(d). Here there are thirty-two distinct sites with isotropic shifts covering a range of 1 MHz [33] which cannot be efficiently refocussed by the conventional 180° pulse used of 417 kHz RF field amplitude. When we use the SHAPs for refocussing we see a much improved excitation response. The apparent loss in sensitivity is due to the short T'_2 values of between 100 and 300 μs leading to increased dephasing during the longer SHAP sequence. Nevertheless this can be tolerated in exchange for the broadband excitation of the full spectral range with uniform phase. The bulk RF inversion profile in Fig. 18(f) shows that we obtain 90% inversion at 400 kHz. The incomplete inversion can

be explained, once again, the short T_2' leading to relaxation and coherence dephasing during the pulse.

These SHAPs have proved to be very successful when applied to paramagnetic materials as shown by the variety of systems to which they have been applied. For example SHAPs have been used in spin-echo experiments for the ^1H NMR of lanthanide-containing organometallic complexes [32], the ^1H and ^{13}C NMR of paramagnetic chromocene adducts [9], and the ^7Li NMR of orthosilicate cathode materials Li_2MSiO_4 ($\text{M} = \text{Fe}, \text{Mn}$) [34]. The pulses have also been incorporated into the CPMG experiment [74]. Most recently they have been used in a more sophisticated adiabatic magic-angle turning (aMAT) experiment used to separate the individual isotropic sites in the spectrum. To date this experiment has been successfully applied for elucidating the structural and electronic properties of the solid-solution cathode materials LiMPO_4 ($\text{M} = \text{Fe}, \text{Mn}$) [33] and ($\text{M} = \text{Fe}, \text{Co}$) [36], and to the Na-battery cathode material $\text{P2-Na}_x[\text{Li}_y\text{Ni}_z\text{Mn}_{1-y-z}]\text{O}_2$ ($0 < x, y, z < 1$) [35].

7.4. Broadband inversion and refocussing using frequency-selective irradiation by Single-Sideband-Selective Adiabatic Pulses ($S^3\text{APs}$)

Having reviewed the application of adiabatic pulses in the high-power regime, we will now turn our attention to the possibility of applying adiabatic pulses in the low-power regime where $\omega_1 \ll \omega_r$. As will be seen in this section these pulses are *frequency-selective to a single sideband*, and so can be analysed in the jolting frame presented in Section 6.6. This scheme has been applied by Wasylishen et al. [20, 22, 23] and Grandinetti et al. [21] to the inversion of the satellites of half-integer spin quadrupoles in order to enhance the signal corresponding to the central transition. More recently these pulse schemes have been applied to paramagnetic species, and a theoretical framework proposed to describe the mechanism of inversion. These pulses were referred to as single-sideband-selective adiabatic pulses ($S^3\text{APs}$) [24].

Before considering the theory in detail we shall first examine the magnetisation trajectories of a spin system subject to a large CSA of 200 kHz at 60 kHz MAS as shown in Fig. 19. The pulse in question is a 1ms WURST-20 [66] sweeping through the +2-order sideband with an RF field amplitude of 50 kHz. When applied to a single

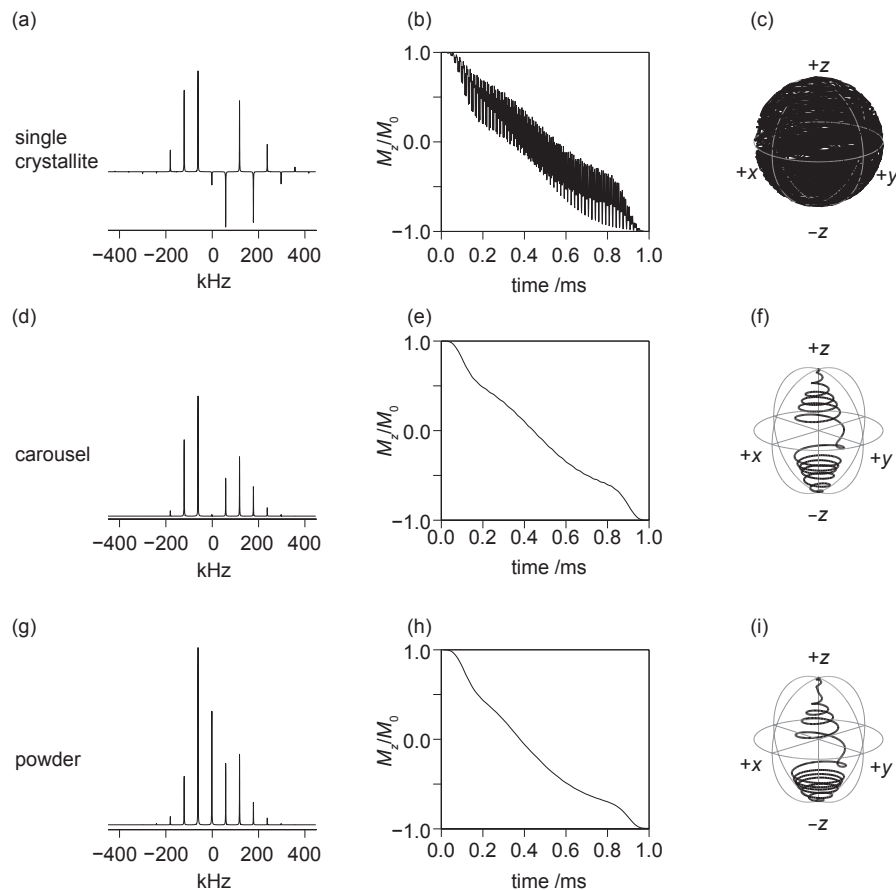


Figure 19: Simulation of the magnetization trajectory of a spin subject to a large shift anisotropy under MAS during an S^3AP [24]. Trajectories are shown for a single crystallite (a)–(c), the average over a whole carousel (d)–(f), and the entire powder (g)–(i). The simulated spectrum of the single crystal at orientation $(\alpha, \beta, \gamma) = (0^\circ, 50^\circ, 0^\circ)$ is shown in (a). The z -component of the magnetization during the SHAP is shown in (b), exhibiting large oscillations superimposed on the usual smooth inversion pathway because of the modulation of the CSA during MAS. In (c) is shown the entire trajectory in three-dimensional space. The magnetization vector oscillates during the pulse and so the trajectory crosses itself several times, resulting in the crowded appearance of the plot in (c). The spectrum of the carousel $(\alpha, \beta) = (0^\circ, 50^\circ)$, representing the average over the angle γ is shown in (d). The corresponding z -magnetization and magnetization trajectory are shown in (e) and (f) respectively. The oscillations that were present in the single crystal plots (b) and (c) have now been averaged out, leaving the smooth inversion pathways. Finally, the simulated spectrum of the powder is shown in (g), with the plots of the z -magnetization and magnetization trajectory in (h) and (i). The shift tensor parameters are: isotropic shift 0 kHz, CSA +200 kHz, asymmetry parameter 0.3, and the MAS frequency was 60 kHz. The S^3AP [24] is a WURST-20 [66] pulse applied to the +2-order sideband which sweeps through 60 kHz in 1 ms at an RF field amplitude of 50 kHz.

crystallite, the spectrum of which is shown in Fig. 19(a), the magnetisation trajectory in Fig. 19(c) exhibits a large number of violent oscillations due to the modulation of the SA by MAS. These oscillations are most clearly seen in the plot of the z -magnetization shown in Fig. 19(b). The resulting quality factor $Q^{(1)}$ is much less than unity, indicating that the magnetisation is not spin-locked to the effective field, and so the pulse is not adiabatic. However we will see in this section that both the effective field and the magnetisation trajectory can be separated into a smooth inversion pathway, which is adiabatic, upon which the rapid oscillations are superimposed. The fact that there *is* a smooth adiabatic component to the inversion of the magnetisation is hinted at when we examine the magnetisation trajectories of the carousel (Fig. 19(d)) and the full powder (Fig. 19(g)). For both cases the plot of the z -magnetization during the pulse, shown in Fig. 19(e) and Fig. 19(h) respectively, shows no oscillations indicating that they are cancelled on averaging over γ , in the same way as for the trajectories during the SHAP in Fig. 14. The full trajectories in Fig. 19(f) and Fig. 19(i) have a form that is similar to those obtained when applying adiabatic pulses to isotropic spin systems, albeit with reduced transverse components which can also be ascribed to the effect of γ averaging.

We will now address these observations with a theoretical treatment of the pulse in the jolting frame. Following the transformation into the jolting frame, the Hamiltonian describing a pulse applied to the n th-order sideband is given by Eq. (118). If we account for both the amplitude profile $\omega_1(t)$ and the phase profile $\phi_p(t)$ being time-dependent, and having the properties in Eq. (53) and Eq. (54) as required for adiabatic pulses, the jolting-frame Hamiltonian $\hat{\mathcal{H}}(t)$ is

$$\hat{\mathcal{H}}(t) = \omega_1(t)\hat{R}_z(\phi_p(t)) \left\{ \sum_{m=-\infty}^{+\infty} A_c^{(m)}\hat{R}_z(\phi_c^{(m)}(\gamma) + (m-n)\omega_r t)^{-1} \hat{I}_x\hat{R}_z(\phi_c^{(m)}(\gamma) + (m-n)\omega_r t) \right\} \hat{R}_z(\phi_p(t))^{-1}. \quad (143)$$

Once again we see that the Hamiltonian can be described as a superposition of RF fields whose carrier frequencies are separated by the spinning frequency, and with relative amplitudes and phases given by the sideband amplitudes and phases. More specifically the field that is applied with carrier frequency $(m-n)\omega_r$ relative to the n th-order sideband has an RF field amplitude $\omega_1(t)A_c^{(m)}$ and a phase that is offset from $\phi_p(t)$ by a

constant $-\phi_c^{(m)}(\gamma)$. The Hamiltonian can therefore be separated into a sum of terms with $m \neq n$ that exhibit oscillations at frequencies $(m - n)\omega_r$ superimposed upon the smooth phase variation of the sweep, and a single term with $m = n$ that does not oscillate. It is the former fields that give rise to the large oscillations in the single-crystallite magnetisation trajectory shown in Fig. 19(b) and Fig. 19(c), and the latter which gives the smooth inversion that is superimposed. For a conventional constant-amplitude pulse this last term is given by the first-order average Hamiltonian. However average Hamiltonian theory is not applicable in this case as the variation of phase and amplitude of the adiabatic pulse are not negligible on the timescale of the rotor period [79] and we must use Floquet theory [80]. The first-order effective Floquet Hamiltonian $\widehat{\mathcal{H}}(t)$ describes the smooth part of the inversion trajectory in the low-power regime, and is given by the term with $m = n$:

$$\widehat{\mathcal{H}}(t) = \omega_1(t) A_c^{(n)} \hat{R}_z \left(\phi_p(t) - \phi_c^{(n)}(\gamma) \right) \hat{I}_x \hat{R}_z \left(\phi_p(t) - \phi_c^{(n)}(\gamma) \right)^{-1}. \quad (144)$$

This simply has the form of an adiabatic pulse applied on resonance with an RF field amplitude scaled by $A_c^{(n)}$ and a constant phase $-\phi_c^{(n)}(\gamma)$ that is added to the time-dependent phase that gives the frequency sweep.

Now we are able to see that whether or not we achieve inversion of a given crystallite depends on whether the pulse described by the Hamiltonian in Eq. (144) satisfies an adiabatic condition of the form set out in Section 6.2. To derive the quality factor we transform the Hamiltonian into the frequency-modulated frame, and then into the first adiabatic frame, as described in Section 6.2, to give $\widehat{\mathcal{H}}^{(1)}(t)$:

$$\widehat{\mathcal{H}}^{(1)}(t) = \omega_{\text{eff}}^{(0)}(t) \hat{I}_z - \dot{\theta}^{(0)}(t) \hat{I}_y. \quad (145)$$

As we have seen before the Hamiltonian is now a sum of a field along z_1 , and a field along $-y_1$ whose amplitudes are given by the size $\omega_{\text{eff}}^{(0)}(t)$ and the rate of change of the tilt angle $\theta^{(0)}(t)$ of the effective field in the frequency-modulated frame. Both quantities are given by expressions that are analogous to those in Section 6.2 with the difference

that the RF field amplitude is scaled down by the intensity of the irradiated sideband:

$$\omega_{\text{eff}}^{(0)}(t)^2 = \omega_{\text{rf}}(t)^2 + \left[\omega_1(t) A_c^{(n)} \right]^2, \quad (146)$$

$$\tan(\theta^{(0)}(t)) = -\frac{\omega_1(t) A_c^{(n)}}{\omega_{\text{rf}}(t)}. \quad (147)$$

From these expressions the quality factor $Q^{(1)}$ in the first adiabatic frame is given by

$$\frac{1}{Q^{(1)}} = \max \left| \frac{\dot{\theta}^{(0)}(t)}{\omega_{\text{eff}}^{(0)}(t)} \right| \quad (148)$$

$$= \max \left| \frac{\omega_1(t) \dot{\omega}_{\text{rf}}(t) - \dot{\omega}_1(t) \omega_{\text{rf}}(t)}{\left[\omega_{\text{rf}}(t)^2 + \left(\omega_1(t) A_c^{(n)} \right)^2 \right]^{3/2}} \right| A_c^{(n)}. \quad (149)$$

This condition is most likely to be violated, as in the isotropic case, when the transmitter is on resonance in the jolting frame and the effective field is at its minimum, whilst the tilt angle changes most rapidly. In this case the $\theta^{(0)}(t) = \dot{\omega}_{\text{rf}}(\tau_p/2) / (A_c^{(n)} \omega_1^{\text{max}})$ and $\omega_{\text{eff}}^{(0)}(t) = A_c^{(n)} \omega_1^{\text{max}}$. The adiabatic condition thus becomes simply $\dot{\omega}_{\text{rf}}(\tau_p/2) \ll (A_c^{(n)} \omega_1^{\text{max}})^2$, which is the identical to the expression obtained in the isotropic/static case, but with the RF field amplitude scaled down by the intensity of the irradiated sideband $A_c^{(n)}$.

As in the case of the SHAP the presence of the SA under MAS conditions weakens the adiabaticity of the pulse compared to both static conditions and isotropic systems. However whereas for the SHAP this weakening effect can be understood by the rapid oscillation of the effective field due to the sample spinning, for the S³AP the explanation is simply that the RF field is lower than the nominal value as it is scaled down by the intensity of the irradiated sideband (remembering that the rapid oscillation effects are effectively removed in the low-power regime). In the standard rotating reference frame the scaling of the effective field is a consequence of the variation of the chemical shift during MAS causing the spin to be on resonance with the pulse for only a fraction of the pulse duration. The equally valid description in the jolting frame is that the RF field amplitude is scaled down *directly*. When the quality factor is sufficiently large and the adiabatic condition is satisfied, the Hamiltonian in Eq. (145) can be approximated

by

$$\widehat{\mathcal{H}}^{(1)}(t) \approx \omega_{\text{eff}}^{(0)}(t) \hat{I}_z, \quad (150)$$

and adiabatic inversion is achieved for the crystallite in question.

The effective field, and hence the quality factor, depends on the intensity of the irradiated sideband and so the inversion performance is strongly orientation dependent. At this point it is worth emphasising that the sideband *intensity* depends only on the Euler angles α and β , and not on γ which only affects the sideband *phase*. Therefore each member of a particular carousel is inverted to the same extent and with the same quality factor, but different carousels may experience different inversion performances. These properties are illustrated by the simulations in Fig. 20. The chosen S³AP is a WURST-20 pulse of 1 ms duration, which is applied to the centreband ($n = 0$) of the sideband manifold which is a consequence of a 200 kHz SA at 60 kHz MAS. The z -magnetization from the trajectories are shown for ten carousels with $\alpha = 0^\circ$ and values of β between 0° and 90° in steps of 10° at RF field amplitudes of 10 and 50 kHz. The RF amplitude of 10 kHz is sufficient to invert an isotropic spin system, and is also able to invert the crystallites with Euler angles $\beta = 0^\circ, 10^\circ, 80^\circ,$ and 90° which have centreband intensities greater than 0.71, corresponding to a scaled RF field of more than 7.1 kHz. However for smaller centrebands, including those with very low intensities of 0.07 for $\beta = 40^\circ$ and 50° , the scaled RF fields are too small to satisfy the adiabatic condition and incomplete inversion is observed. Some low-intensity oscillations superimposed upon the smooth parts of the trajectories are also seen, and are due to the residual effects of the oscillating RF fields that we excluded in the first-order effective Floquet Hamiltonian. These oscillations are of much lower intensity compared to those in Fig. 19 as the RF field is lower and is within the low-power approximation. However, as before, these oscillations are cancelled on computation of the trajectory of the whole carousel. Also shown for comparison are simulations of the trajectories on an isotropic spin system for which the RF field of the pulse is scaled down directly by an amount equal to the intensity of the irradiated sideband. The agreement between the model and exact simulations is excellent, thus validating the theoretical description of these S³APs in the low-power regime.

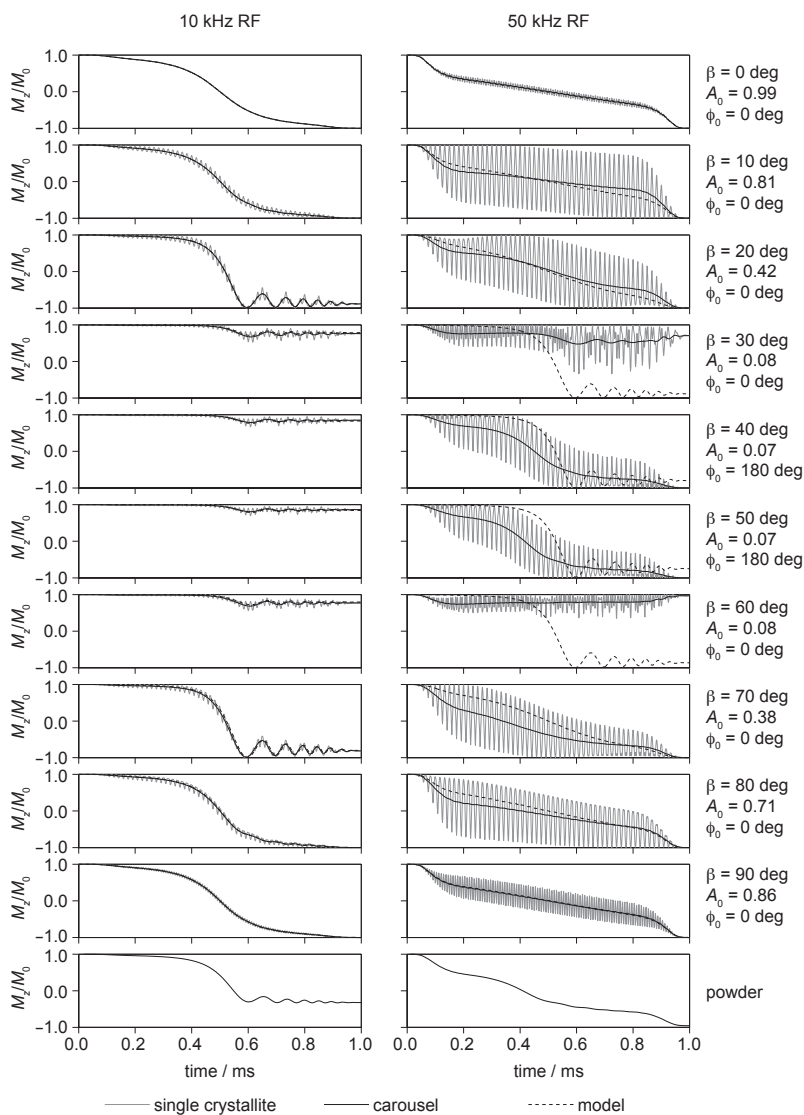


Figure 20: Comparison of exact simulation of the inversion trajectories produced by a S^3 AP under MAS with a simple isotropic model for different crystallite orientations. The shift tensor parameters are: isotropic shift 0 kHz, CSA +200 kHz, asymmetry parameter 0.3, and the MAS frequency is 60 kHz. The S^3 AP is a WURST-20 pulse applied to the centreband which sweeps through 60 kHz in 1 ms at RF field amplitudes of 10 kHz (left-hand column) and 50 kHz (right-hand column). Simulated results are shown for a range of ten values of β from 0° to 90° in steps of 10° ; $\alpha = \gamma = 0^\circ$. The inversion pathways are shown for the single crystallite (grey full line) and the carousel (black full line), and are shown with the inversion pathways simulated assuming an isotropic spin system in which the RF field amplitude is scaled down by the centreband intensity $A_c^{(0)}$ as shown in Eq. (145) (black dashed line). The match between the exact simulated and model for the WURST pulse at the RF field amplitude of 10 kHz (left-hand column) is excellent. However, only partial inversion is seen for the powder resulting from the effective scaling down of the RF field as discussed in the text. Raising the RF field amplitude to 50 kHz delivers 100% inversion, but the inversion trajectories for some of the crystallites depart from those calculated in the low-power approximation.

The inversion trajectory for the whole powder at 10 kHz RF field amplitude is also shown in Fig. 20. The overall inversion performance is rather poor, but can be improved by the simple expedient of raising the RF field amplitude in order to give a better spin-locking performance for the crystallites. The single-crystallite and carousel magnetisation trajectories at a higher RF field amplitude of 50 kHz are shown in the right-hand column. Firstly we notice that the oscillations in the trajectory have increased in amplitude, and that the results for the carousel are no longer in good agreement with the model simulations. Both of these observations can be ascribed to the pulse no longer being in the lower power regime as the RF field amplitude of 50 kHz is close in magnitude to the spinning frequency of 60 kHz, and that the pulse is now also irradiating the neighbouring sidebands. In particular we have to include higher-order terms in the effective Floquet Hamiltonian expansion in order to determine the smooth part of the magnetisation trajectory. For example we see that for $\beta = 30^\circ$ and 60° the inversion is worse than expected with the low-power model, whereas for $\beta = 40^\circ$ and 50° we actually see an improved performance. The form of the second- and third-order effective Hamiltonians $\hat{\mathcal{H}}^{(2)}$ and $\hat{\mathcal{H}}^{(3)}$ are given in Eq. (121) and Eq. (122). Each effective Hamiltonian is a sum of terms $\Gamma^{(2)}$ and $\Gamma^{(3)}$ which have the form:

$$\Gamma^{(2)} = \frac{\omega_1^2}{\omega_r} \{A^2\} \hat{I}_z, \quad (151)$$

$$\Gamma^{(3)} = \frac{\omega_1^3}{\omega_r^3} \{A^3\} \hat{R}_z(\phi^{(3)})^{-1} \hat{I}_x \hat{R}_z(\phi^{(3)}), \quad (152)$$

where the notation $\{A^n\}$ represents a product of n sideband intensities. Full forms of these expressions for an axially-symmetric SA tensor are given in Ref. [24]. The second-order effective Hamiltonian represents a magnetic field along z , and has the effect of shifting the isotropic shift in the jolting frame away from zero, playing the same role as a Bloch–Siegert shift [59]. Whilst this term can, in principle, shift the isotropic frequency outside the bandwidth of the S³AP, this has hitherto never been observed and so it has been postulated that it merely changes the point at which the magnetisation vector crosses the xy plane and does not alter the inversion performance. The third-order effective Hamiltonian is more important as it represents an RF field in the

transverse plane that will combine with the field of the first-order effective Hamiltonian to either reinforce or reduce it. If the first-order field is reinforced the overall inversion performance will be better than expected from the low-power model, which is what is observed for $\beta = 40^\circ$ and 50° , but if the field is reduced we will see a worse than expected performance, which is why the magnetisation vectors of the crystallites with $\beta = 30^\circ$ and 60° are not inverted. The inversion properties for the individual crystallites are complicated, but for the whole powder we see a much improved performance with close to 100% inversion.

It is important to consider the effects that must be taken into account when optimising an S^3AP on a powder sample, as the majority of solid-state NMR is performed on such samples. We now consider how the interplay between the parameters of the pulse shape, the RF amplitude, the MAS frequency, and the carrier frequency affect the inversion performance. Following the above discussion on the orientational dependence of the inversion on single crystallites, one could expect that elucidating the effect on a full powder would be extremely complicated. Nevertheless the important considerations are easy to deduce and can be summarised readily from the simulations shown in Fig. 21. Fig. 21(a) shows contour plots of the value of the z -magnetization following an S^3AP as a function of both the carrier frequency relative to the isotropic shift, and the RF field amplitude for five different MAS frequencies between 20 and 100 kHz in steps of 20 kHz. The pulse is a WURST-20 of 1 ms duration with a sweep width that is equal to the spinning frequency. For each spinning frequency the regions of best inversion occur when the carrier frequency is placed such that one of the sidebands lies within the bandwidth of the pulse, as expected from the analysis in the jolting frame. In addition when the carrier is placed between two sidebands or outside the range of the sideband manifold the inversion performance is poor, again as expected.

Cross sections from the contour plots showing the inversion and RF field profiles are also shown. The inversion profiles as a function of the carrier frequency are shown in Fig. 21(b), and were calculated at the lowest RF field amplitude which gives the best performance. The profiles exhibit the “sideband” structure in which each lobe has a bandwidth that is characteristic of the WURST-20 pulse that was used. We note that for higher spinning frequencies, the greater separation of the sidebands allows us

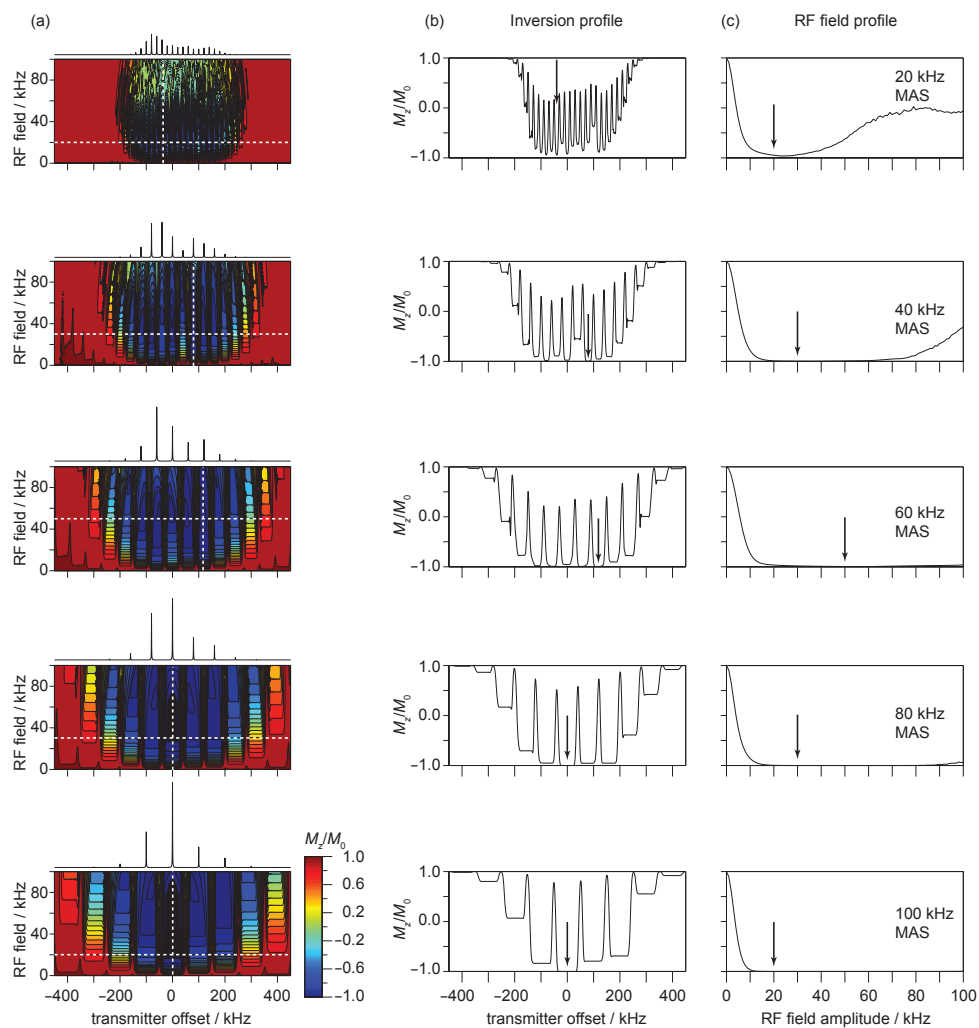


Figure 21: Simulated inversion performance of the S^3 APs under MAS. In (a) are shown contour plots of the inversion of the powder sample as a function of RF field amplitude and transmitter offset at MAS frequencies of 20, 40, 60, 80, and 100 kHz. In each case, the S^3 AP is a WURST-20 pulse of duration 1 ms with a sweep width equal to the spinning frequency. The best inversion occurs when the transmitter is resonant with one of the sidebands and the RF field amplitude is sufficiently high to satisfy the adiabatic condition in Eq. (149) for all crystallites. In (b) are shown horizontal cross sections through the contour plots, taken at the positions shown by the horizontal white dashed lines. The plots show the inversion as a function of transmitter offset. The RF amplitude profiles in (c) are cross sections taken at the positions of the vertical white dashed lines in the contour plots. The arrows in the plots in (b) and (c) indicate the transmitter offset and lowest RF field amplitude at which the best inversion performance is obtained for each MAS frequency. Each pair of optimum values is also indicated by the intersection of the two white dashed lines in each contour plot in (a). The optimum values of (sideband order, RF field amplitude) for the five MAS frequencies are: $(-2, 20 \text{ kHz})$ at 20 kHz MAS, $(+2, 30 \text{ kHz})$ at 40 kHz MAS, $(+2, 50 \text{ kHz})$ at 60 kHz MAS, $(0, 30 \text{ kHz})$ at 80 kHz MAS, and $(0, 20 \text{ kHz})$ at 100 kHz MAS. The shift tensor parameters are: isotropic shift 0 kHz, CSA +200 kHz, asymmetry parameter 0.3.

to use a WURST pulse with a greater sweep width, and therefore a greater bandwidth. The carrier frequency that gave the best inversion is, for each MAS frequency, indicated with an arrow. For the MAS frequencies up to and including 60 kHz, the optimal results were obtained by irradiating one of the second-order sidebands (-2 for 20 kHz MAS, and $+2$ for both 40 and 60 kHz MAS). There are clearly some orientations for which a large fraction of the spectral intensity is located in the centreband, and which would only be completely inverted by a pulse that is applied to the centreband, for example crystallites with $\beta = 0^\circ$. However these represent a very low proportion of the total number of crystallites in the powder, and the fact that they are only partially inverted does not compromise the overall performance for the whole powder. For the higher MAS frequencies, 80 kHz and 100 kHz, 100% inversion is obtained by irradiating the centreband. This is because as we increase the spinning frequency, a greater amount of the spectral intensity for each crystallite is located in the centreband at the expense of the other sidebands, as can be seen by the centreband becoming the most intense sideband in the simulated powder spectra in Fig. 21(a), and so the RF field amplitude in the jolting frame is scaled down to a lesser extent and all orientations can be inverted.

The RF field profiles are shown in Fig. 21(c). Generally the total extent of inversion increases from 0 kHz until we reach a threshold RF field amplitude above which the adiabatic condition holds for most of the crystallites. For the low MAS frequency of 20 kHz we note that there is a very narrow range of RF fields above the threshold of approximately 20 kHz before we see the degree of inversion decrease with increasing RF field amplitude. This degradation in performance at higher RF fields can be ascribed mainly to the larger part played by the higher-order terms in the effective Floquet Hamiltonian in the description of the spin dynamics now that we are no longer in the low-power regime. As we saw above, the higher order effects can either aid or retard the inversion for different crystallites, but overall they degrade the inversion of the powder as a whole. At higher MAS frequencies there is a larger window in which we obtain complete inversion, which is simply because the wider spacing of the sidebands allows us to use larger RF field amplitudes before the higher-order terms exert a significant effect. Increasing the MAS frequency allows us to use more intense RF fields, but we can also see that they may not be needed as complete inversion at high

spinning frequencies, such that the centreband is the most intense sideband in the manifold, is often possible with lower RF fields than at lower spinning frequencies. This is observed for 80 kHz and 100 kHz MAS in Fig. 21(c) where 30 kHz and 20 kHz RF field amplitudes respectively are sufficient, compared to 20 kHz, 40 kHz, and 50 kHz at 20 kHz MAS, 40 kHz MAS, and 60 kHz MAS respectively.

The simulations indicate that the S³APs present an attractive low-power alternative to the SHAPs when applied to a system either with a single spinning-sideband manifold, or with multiple sideband manifolds whose isotropic shifts satisfy the condition

$$-\frac{1}{2}\Delta\Omega \leq \Omega_{\text{iso}} + n\omega_r \leq +\frac{1}{2}\Delta\Omega, \quad (153)$$

i.e. that one of the sidebands of each manifold lies within the bandwidth $\Delta\Omega$ of the pulse. In addition to those already given above this is another reason why the pulses are particularly efficacious at high MAS frequencies. The principle disadvantage of the S³AP is the length required to achieve adiabatic inversion, which is usually of the order of milliseconds, which can lead to significant signal losses for paramagnetic species because of the large relaxation rates. This is seen in the experimental RF field profiles of two WURST-20 S³APs applied to the ⁷Li NMR of LiFe_{0.5}Mn_{0.5}PO₄ at 60 kHz MAS, as shown in Fig. 22. The isotropic shifts of the different ⁷Li sites, and therefore the centrebands of the sideband manifolds, are coincident, within the inhomogeneous broadening [33], and so the spectrum can be manipulated using single-sideband-selective pulses. Thirteen RF field profiles for each pulse were acquired in which the transmitter was resonant with each of the sidebands from -6 to $+6$ in turn. In Fig. 21(a) are shown the RF profiles obtained with a sweep of 60 kHz in 1 ms. The best inversion is obtained by irradiating the -2 -order sideband with an RF field amplitude of 35 kHz in which the inverted intensity is 50% of the maximum. This is significantly less than expected from simulation, and so we ascribe it to the losses incurred by relaxation and possible coherent dephasing during the pulse, which is expected from the short relaxation times of 1.88 ms and 1.59 ms for T_1 and T_2' respectively. This is confirmed in Fig. 21(b) which shows the RF field profiles for a 60 kHz sweep of 0.5 ms duration in which we see increased inversion for a number of the curves despite the faster sweep rendering

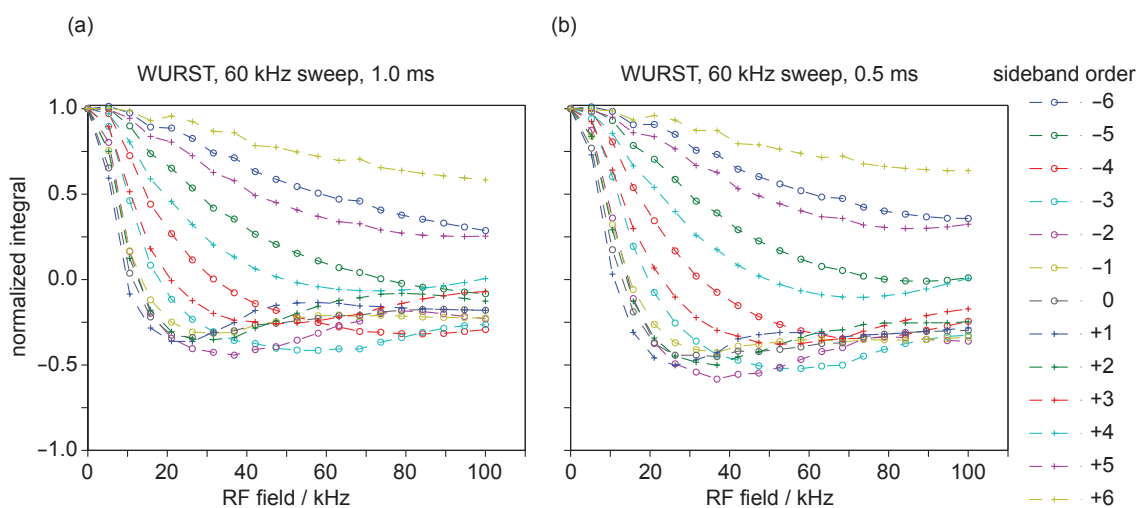


Figure 22: Experimental illustration of the inversion performance of the S^3 APs applied to the ${}^7\text{Li}$ spectrum of the paramagnetic cathode material $\text{LiFe}_{0.5}\text{Mn}_{0.5}\text{PO}_4$ at 11.74 T and 60 kHz MAS. In (a) are shown the RF field amplitude profiles of a 1.0 ms WURST-20 pulse sweeping through a single sideband. The different curves represent the integrated intensity of the ${}^7\text{Li}$ spectrum following irradiation of each sideband. The best result occurs with irradiation of the -2 -order sideband at 40 kHz RF field amplitude. In (b) is shown the corresponding set of RF field amplitudes giving the inversion performance of a shorter 0.5 ms WURST-20 pulse.

the pulse ‘less adiabatic’.

It is clear that shorter pulses will have to be developed for this scheme to become widely used, even for systems exhibiting a single sideband manifold, or manifolds with coincident sidebands. However it is clear from the theoretical treatment presented above that these pulses are destined to become powerful alternatives to SHAPs for experiments at MAS frequencies of 100 kHz and above. Moreover the jolting frame formalism describing the effect of low power irradiation in the presence of a large CSA under MAS is expected to be a useful tool in the development of this area.

7.5. DANTE

We now turn our attention to the application of the DANTE sequence to the NMR of spinning paramagnetic powders. Unlike the adiabatic pulse schemes, in which the RF field amplitude and phase are changed “slowly” according to the adiabatic condition, in DANTE the RF field amplitude is changed “suddenly” as the transmitter is turned on for a short time, and off for the remainder of the cycle time. Also in contrast to adiabatic pulse schemes, DANTE can readily be applied to excitation and inversion of spin systems. However it will also be seen that the approach is not generally applicable to all possible systems with the NMR spectrum having to satisfy certain restraints: namely that either only a single site is present or that, if multiple sites are present the isotropic shifts are spread over a range that is either smaller than the spinning frequency; and that the sidebands are not inhomogeneously broadened. The reasons for these restrictions will be expanded upon below when the sequence has been analysed in more detail.

The application of DANTE to broadband NMR was first proposed by Vitzthum et al [25] for the excitation of a single ^{14}N site that is broadened by the quadrupolar coupling interaction. The transmitter was set to be resonant with the centrebands of the two satellite transitions with the cycle time of the sequence ω_c , as defined in Section 6.4, set to an integer multiple K of the spinning frequency $\omega_c = K\omega_r$ so that K short flip-angle pulses are applied per rotor period. The sequences with $K > 1$ have been referred to as overtone DANTE sequences [25]. In effect this results in *only the sidebands of order nK* being irradiated, where n is an integer. If the total number of short flip-angle

pulses applied is N the sequence can be denoted as D_K^N [98]. Following the application to quadrupolar nuclei, the same scheme was then applied to the broadband excitation of spin-1/2 nuclei in paramagnetic systems [71, 99].

To date there has been some work aimed at elucidating the precise mechanism by which DANTE achieves broadband inversion and excitation [25, 71, 98, 100], but such studies have been limited by failing to account for the full complexity of the theoretical treatment needed when applying a selective pulse scheme to a spinning solid, and have thus not been able to account for the effects encountered when using a sequence D_K^N with $K > 1$.

The Hamiltonian describing the DANTE sequence applied to an isotropic system was derived in Section 6.4, and is given in Eq. (99). When applied to a spinning solid with a large SA due to a paramagnetic interaction we must include an additional term describing the MAS modulation of the shift. Then, following Section 6.6 we can simplify the description by applying the jolting frame transformation as follows:

$$\begin{aligned} \hat{\mathcal{H}}(t) &= \sum_{m=-\infty}^{+\infty} \sum_{n=-\infty}^{+\infty} A_c^{(m)} C_n \hat{R}_z \left((\omega_{\text{tx}} - \Omega_0)t + \zeta_n - \phi_c^{(m)}(\gamma) + (n\omega_c - m\omega_r)t \right) \hat{I}_x \\ &\times \hat{R}_z \left((\omega_{\text{tx}} - \Omega_0)t + \zeta_n - \phi_c^{(m)}(\gamma) + (n\omega_c - m\omega_r)t \right)^{-1} \end{aligned} \quad (154)$$

$$\begin{aligned} &= \sum_{m=-\infty}^{+\infty} \sum_{n=-\infty}^{+\infty} A_c^{(m)} C_n \hat{R}_z \left(\zeta_n - \phi_c^{(m)}(\gamma) + (nK - m)\omega_r t \right) \hat{I}_x \\ &\times \hat{R}_z \left(\zeta_n - \phi_c^{(m)}(\gamma) + (nK - m)\omega_r t \right)^{-1}. \end{aligned} \quad (155)$$

To go to the third line we have set $\omega_c = K\omega_r$, as discussed above, and set the transmitter offset so that it is resonant with the isotropic shift, so that $\omega_{\text{tx}} = \Omega_0$. This expression is reminiscent of that obtained for the S³AP with the added complexity of two summations rather than one, where the index m sums over the sidebands in the manifold, and n sums over the components in the RF ‘comb’ of the DANTE sequence.

As with earlier applications of the jolting frame, the spin dynamics can, to a very good approximation, be described by the first-order average Hamiltonian $\overline{\hat{\mathcal{H}}}$, or equivalently by the first term in the expansion of the effective Floquet Hamiltonian, provided that $|C_n| \ll \omega_r$ for all n . This condition is satisfied if $\overline{\omega}_1 = \omega_1^{\max} \tau_p / \tau_c \ll \omega_r$, and then

the only terms in the double sum above that contribute are those with $m = nK$, which are time independent:

$$\hat{\mathcal{H}} = \sum_{m=-\infty}^{+\infty} \sum_{n=-\infty}^{+\infty} A_c^{(m)} C_n \hat{R}_z(\zeta_n - \phi_c^{(m)}(\gamma)) \hat{I}_x \hat{R}_z(\zeta_n - \phi_c^{(m)}(\gamma))^{-1} \delta_{m,nK} \quad (156)$$

$$= \sum_{n=-\infty}^{+\infty} A_c^{(nK)} C_n \hat{R}_z(\zeta_n - \phi_c^{(nK)}(\gamma)) \hat{I}_x \hat{R}_z(\zeta_n - \phi_c^{(nK)}(\gamma))^{-1}. \quad (157)$$

It is worth considering the implications of the form of the average Hamiltonian before analysing the effects in greater detail. We see that the only sidebands that contribute are of order nK , which is a result of these being the only sidebands that experience an irradiation from the DANTE sequence. That is, if $K = 1$ then all sidebands are simultaneously irradiated by DANTE, whereas if $K = 2$ only the even-order sidebands are irradiated. This has important implications on the spectrum that is obtained following excitation by DANTE as a result of the effect on the γ -averaging. Fig. 23 shows simulated spectra of a selection of single crystallite orientations belonging to the same carousel following excitation by a conventional non-selective 90° pulse, and DANTE sequences of 50 kHz RF field amplitude comprising $K = 1, 2, 3, 4,$ and 8 pulses per rotor period. The value of N is also increased so that the DANTE sequences have the same duration of 10 rotor periods, i.e. $N = 10K$. For each scheme six single-crystallite spectra are shown at 60 kHz MAS with γ -angles running from 0° to 300° in steps of 60° , in addition to the spectrum obtained by averaging over the carousel.

For the non-selective 90° pulse the sideband manifolds of the individual crystallites are excited with the same pattern of intensities, but different phases as expected from the expressions in Eq. (34), and on summing we obtain sidebands with the same phase [54]. The spectra obtained following excitation with D_1^{10} are identical to those obtained with non-selective excitation, an observation that can be explained as follows. The pulse lengths τ_p are sufficiently short to satisfy the condition $\tau_p \ll \tau_c$, which can be easily verified by noting that $\tau_p = 5.0/N \mu\text{s} = 0.5/K \mu\text{s}$ and $\tau_c = 11.67/K \mu\text{s}$, leading to $\tau_p/\tau_c = 0.04$. Therefore the DANTE excitation pulse amplitudes C_n and phases ζ_n are given by Eq. (92) as $\bar{\omega}_1$ and 0 respectively. Eq. (157) takes on the simplified form

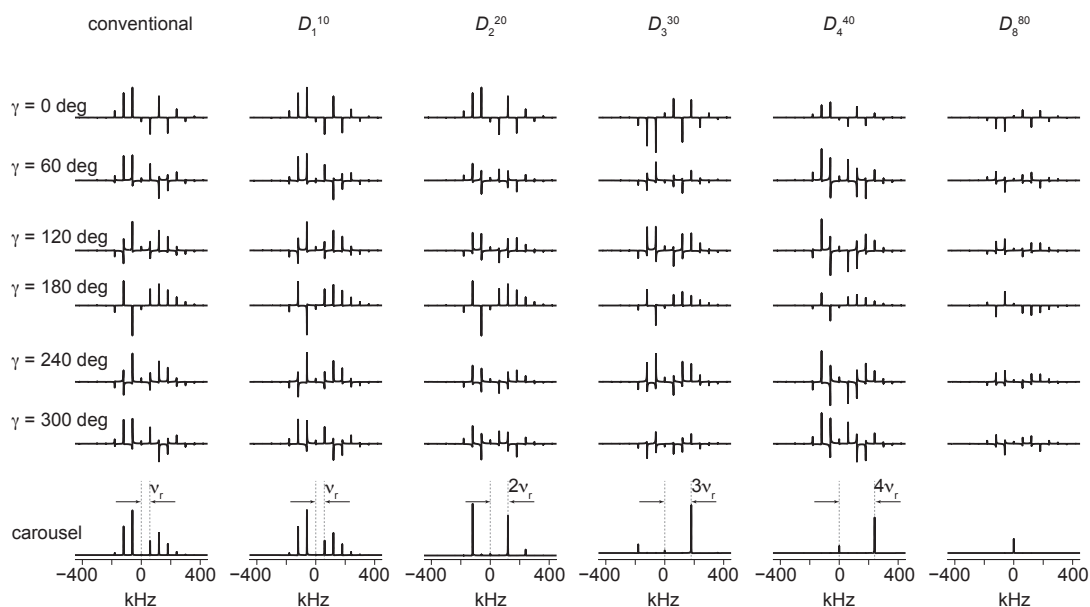


Figure 23: Simulated effects of γ -averaging on the spectra excited by a DANTE sequence with multiple pulses per rotor period. The spectra shown are of single crystallites that are members of the carousel $(\alpha, \beta) = (0^\circ, 50^\circ)$ and with γ angles between 0° and 300° in steps of 60° . Also shown are the spectra resulting from the average over all values of γ for each excitation scheme. For each simulation the transmitter frequency is resonant with the centreband. The carousel excited by the DANTE sequence with one pulse per rotor period D_1^{10} matches exactly the conventional spectrum, in that all sidebands have the same phase and are separated by the spinning frequency [54]. The use of a DANTE sequence with two pulses per rotor period D_2^{20} interferes with the γ averaging so that the intensities of the odd-order sidebands cancel, resulting in a carousel spectrum in which the sidebands are apparently separated by twice the spinning frequency. The simulations of the sequences D_3^{30} and D_4^{40} illustrates the general result that the application of a sequence D_K^N to the spectrum of a powder sample spinning at ω_r interferes with the γ averaging so that the resulting spectrum contains only the sidebands of orders that are integer multiples of $K\omega_r$. The application of the sequence D_8^{80} results in only the centreband being observed in the carousel spectrum. This is because the ± 8 -order sidebands, which are the closest sidebands to the centreband which would appear in the spectrum, have negligible intensity and so are not observed. The shift tensor parameters are: isotropic shift 0 kHz, CSA +200 kHz, asymmetry parameter 0.3, and the MAS frequency is 60 kHz. All DANTE sequences were of RF field amplitude 50 kHz and duration 166.67 μ s.

for $K = 1$

$$\hat{\mathcal{H}} = \bar{\omega}_1 \sum_{n=-\infty}^{+\infty} A_c^{(n)} \hat{R}_z(-\phi_c^{(n)}(\gamma)) \hat{I}_x \hat{R}_z(-\phi_c^{(n)}(\gamma))^{-1}, \quad (158)$$

which is a sum of contributions to the overall RF field in the jolting frame from each individual sideband. The sum is simply equal to \hat{I}_x , which can be seen by considering the following identity:

$$\begin{aligned} & \hat{R}_z(\Phi_c^{\text{SA}}(\gamma; 0, 0)) \hat{I}_x \hat{R}_z(\Phi_c^{\text{SA}}(\gamma; 0, 0))^{-1} \\ &= \sum_{m=-\infty}^{+\infty} A_c^{(m)} \hat{R}_z(\phi_c^{(m)}(\gamma)) \hat{I}_x \hat{R}_z(\phi_c^{(m)}(\gamma))^{-1} \end{aligned} \quad (159)$$

$$= \hat{I}_x, \quad (160)$$

and so we obtain

$$\hat{\mathcal{H}}(t) = \bar{\omega}_1 \hat{I}_x. \quad (161)$$

This is simply an RF pulse of amplitude $\bar{\omega}_1$ applied on resonance to an isotropic spin system in the jolting frame which, when applied for a time $N\tau_c$ such that $\bar{\omega}_1 N\tau_c = \omega_1^{\text{max}} N\tau_p = \pi/2$, will give perfect excitation. In other words, a DANTE sequence of the form D_1^N should be able to give uniform excitation of a sideband manifold provided we are resonant with one of the sidebands.

In the short-flip-angle pulse limit $\tau_p \ll \tau_c$ with more than one pulse per rotor period ($K > 1$) the first-order average Hamiltonian in the jolting frame is

$$\hat{\mathcal{H}} = \bar{\omega}_1 \sum_{n=-\infty}^{+\infty} A_c^{(nK)} \hat{R}_z(-\phi_c^{(nK)}(\gamma)) \hat{I}_x \hat{R}_z(-\phi_c^{(nK)}(\gamma))^{-1}. \quad (162)$$

We see that only the sidebands of orders $0, \pm K, \pm 2K, \dots$ contribute to the pulse as expressed in the jolting frame. The direct result of this is that the sideband manifold of the carousel that is observed in the rotating frame contains only those sidebands of order separated from the centreband by an integer multiple of K . This is seen in Fig. 23 in the simulated spectra following excitation by the sequence D_2^{20} (with $K = 2$) where only the sidebands with even order are seen in the spectrum of the carousel. It is tempting to explain this observation as resulting from an increase in the effec-

tive spinning frequency. However this is certainly not the case as the spectra of the individual crystallites contain all the sidebands expected from an unchanged spinning frequency, but with different phases compared to those excited conventionally, or by D_1^{10} . The cancellation of the odd-order sidebands in the carousel is therefore simply a consequence of the γ -averaging being perturbed by the different excitation scheme. In addition when we increase the spinning frequency in reality, the spectral intensity is distilled into fewer sidebands whose intensities therefore increase. This is not what is observed here where the relative intensities of the surviving sidebands match those of the conventional carousel spectrum. The same behaviour is observed with the excitation sequences D_3^{30} and D_4^{40} , where the carousel spectra contain only sidebands with orders that are integer multiples of 3 and 4 respectively. Once again, each individual crystallite is excited to give its full sideband manifold, and the cancellation in the carousel is purely a consequence of γ -averaging. In all cases this behaviour means that the spectrum of the full powder will also only contain sidebands of order nK .

When K is increased so that ω_c is larger than the anisotropy, the only sideband that contributes in the sum of Eq. (162) is the centreband, as the sidebands with orders more positive than K , or more negative than $-K$, have zero intensity. The sum therefore collapses to a single term to give

$$\hat{\mathcal{H}}(t) = \bar{\omega}_1 A_c^{(0)} \hat{R}_z(-\phi_c^{(0)}(\gamma)) \hat{I}_x \hat{R}_z(-\phi_c^{(0)}(\gamma))^{-1}. \quad (163)$$

This is exactly the same Hamiltonian that we obtained for single-sideband-selective irradiation with a low-power constant-amplitude pulse in Eq. (124), where we have substituted $\bar{\omega}_1$ for ω_1 . Following such a DANTE excitation sequence we would expect the spectrum of the carousel to contain only the irradiated sideband (here the centreband) due to the perturbation of the γ -averaging as calculated using Eq. (130). This is seen in Fig. 23 for the sequence D_8^{80} where we see only the centreband in the carousel spectrum as the +8- and -8-order sidebands have negligible intensity.

The form of the Hamiltonians derived above also has a direct effect on the efficiency of the excitation. As shown in Eq. (161) a DANTE sequence with one pulse per rotor period should give excitation with 100% efficiency for all crystallites in the

powder simultaneously, provided that N , τ_p , and ω_1^{\max} are properly calibrated. This is confirmed by the simulation of the RF field amplitude profile of D_1^{10} applied to the full powder average of a spin system with a 200 kHz CSA at 60 kHz MAS in Fig. 24 (top panel) in which are shown the calculated profiles of the x -, y -, and z -magnetization components. The variation of the three components with RF field amplitude has the same form as that for a conventional pulse of phase x applied to an isotropic spin on resonance with $M_x = 0$, $M_y = -\sin(\omega_1^{\max} N \tau_p)$, and $M_z = \cos(\omega_1^{\max} N \tau_p)$. This is the result of the sum of the normalised complex sideband intensities for a given crystallite being equal to unity, as shown by the identity in Eq. (159). However for $K > 1$ not all the sidebands contribute to the sum in the expression of the Hamiltonian in Eq. (162), and so the sum is no longer equal to unity. The sequence therefore no longer behaves as an ideal pulse, and uniform excitation of the signal in all crystallites simultaneously is no longer possible. This is also shown in Fig. 24 for DANTE sequences with $K = 2, 3, 4,$ and 8 , both for sequences with a constant number (10) of pulses (denoted D_K^{10}) of length $166.67/K \mu\text{s}$, and a constant length of $166.67 \mu\text{s}$ and an increasing number of pulses (denoted D_K^{10K}). For none of these sequences is 100% excitation achieved for the powder, and so these sequences cannot be used for uniform, broadband excitation. The RF field profiles are also shown for two low-power constant-amplitude centreband-selective pulses to illustrate their equivalence to the DANTE sequences with $K = 8$. The pulse of length $20.83 \mu\text{s}$ is equivalent to D_8^{10} , for which the RF field amplitude is effectively scaled down by a factor of 0.24 and hence is why the DANTE RF scale of 0 to 200 kHz is equivalent to 0 to 48 kHz for the conventional pulse. The small deviation in behaviour for the conventional pulse above 40 kHz is due to higher-order effects in the average Hamiltonian that have hitherto not been accounted for, but which become important when the RF field becomes comparable to the spinning frequency. The longer pulse of $166.67 \mu\text{s}$ duration is equivalent to D_8^{80} , for which the effective RF field amplitude scaling factor is 0.03; the ‘equivalent’ RF scale for the former pulse is therefore 0 to 6 kHz. We note that, unlike the other pulse, there is no deviation in the behaviour between the conventional pulse and the DANTE sequence as the lower RF fields being considered mean that higher-order effects are still negligible.

We now turn our attention to the excitation and inversion profiles of the DANTE

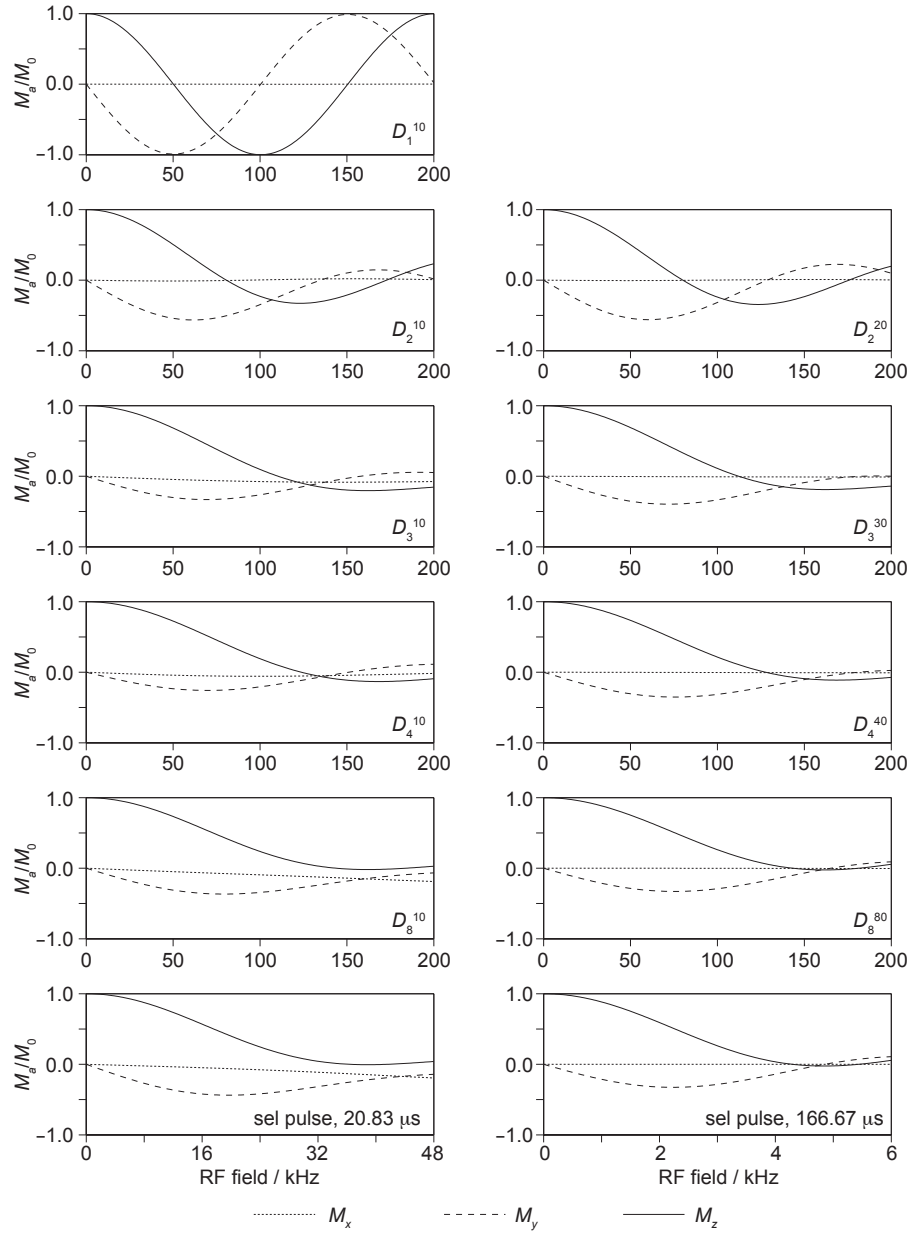


Figure 24: Radiofrequency field profiles of a selection of DANTE pulse sequences D_K^N [25]. All profiles show the x - (dotted line), y - (dashed line) and z -magnetization (full line) present after the sequence as a function of RF field amplitude. The sequences whose profiles are shown in the left-hand column all have 10 DANTE pulse–delay units, and are of duration $10\tau_r/K$ which decreases with the number of pulses per rotor period K . The sequences whose profiles are shown in the right-hand column are all of equal duration $10\tau_r = 166.67 \mu\text{s}$. The RF field profiles of the DANTE sequences with $K = 8$ are exactly the same as those due to a constant-amplitude pulse of the same duration ($20.83 \mu\text{s}$ for D_8^{10} and $166.67 \mu\text{s}$ for D_8^{80}) and an RF field amplitude given by the scaled RF field amplitude of the DANTE sequence. The latter profiles are shown at the bottom of each column. The shift tensor parameters are: isotropic shift 0 kHz, CSA +200 kHz, asymmetry parameter 0.3, and the MAS frequency is 60 kHz.

pulse-sequence elements as a function of the isotropic offset of the spin from the carrier. The examples considered here are the inversion profiles of DANTE sequences that have been optimised as 180° pulses at different MAS frequencies, but the same considerations also apply to the excitation and refocusing of coherences. These sequences are compared, in Fig. 25, with a non-selective 180° and two SHAPs of different sweep widths and the same RF field amplitude. The simulations of the inversion profiles were made at MAS frequencies of (a) 20 kHz, (b) 40 kHz, (c) 60 kHz, (d) 80 kHz, and (e) 100 kHz. The SHAPs are the same as those analysed by simulations in Section 7.3, namely tanh/tan pulses of $50 \mu\text{s}$ length, 5 MHz and 10 MHz sweep widths, and RF field amplitudes equal to (a) 210 kHz, (b) 310 kHz, (c) 400 kHz, (d) 500 kHz, and (e) 550 kHz. The DANTE sequences were chosen to have the same duration as the SHAPs, which therefore required an increase in N with MAS frequency; the exact sequences used were therefore (a) D_1^1 (which is equivalent to a non-selective pulse), (b) D_1^2 , (c) D_1^3 , (d) D_1^4 , and (e) D_1^5 . The DANTE pulses, SHAPs, and non-selective pulses also shared the same RF field amplitude for each MAS frequency.

So far the theoretical treatment in combination with the simulations has confirmed that DANTE sequences with one pulse per rotor period can be used to give uniform excitation or inversion of a spin which exhibits a broad spinning sideband manifold comprising narrow sidebands provided we are on resonance with one of the sidebands. When considering the experimental performance it is important to see how well the sequence performs on systems that show effects that are commonly encountered in paramagnetic systems, namely inhomogeneous broadening of the sidebands, multiple sites giving overlapping spinning sideband manifolds with a large range of isotropic shifts that, in general, will not be known a priori, and short relaxation times.

The DANTE inversion profile at 20 kHz MAS, shown in Fig. 25(a) is exactly the same as the one obtained for the non-selective pulse. This is expected as the former comprises simply just one pulse ($N = 1$) with the same RF field and length at the conventional pulse. Neither achieves 100% inversion, with the best performance being 60% on resonance and dropping off rapidly with offset. The reason for the non-complete inversion on resonance is the presence of the CSA which broadens the resonance, and the MAS which constantly shifts the instantaneous chemical shift into and

out of the pulse bandwidth. Both SHAPs perform much better, giving 100% inversion over a bandwidth of approximately 1 MHz, with the pulse with the wider sweep width having the larger bandwidth. At 40 kHz MAS the DANTE sequence comprises $N = 2$ pulses with the result that the inversion profile splits into a series of spikelets of high inversion efficiency that are separated by the spinning frequency (40 kHz), as shown in Fig. 25(b). The envelope of the spikelet inversion efficiency resembles a sinc function that falls away with increasing offset. This envelope is now broader than the inversion profile of the non-selective pulse, but it should be noted that, for the DANTE sequence, there is *no* inversion when the isotropic shift falls between two spikelets. The two SHAPs require a higher RF field amplitude to achieve inversion on resonance, and this also results in the bandwidth of each being larger than at 20 kHz MAS. The same effects are noticed at the higher spinning frequencies of 60 to 100 kHz in Fig. 25(c)–(e). The DANTE inversion profile exhibits spikelets that are separated by a larger interval (equal to the spinning frequency) and their efficiency envelope becomes broader. At 100 kHz MAS it can be seen that the bandwidth of the envelope is larger than the bandwidth of the SHAP with the 10 MHz sweep. However it should, once again, be noted that for spins with isotropic chemical shifts placed between two spikelets, there is no inversion.

The first experimental example presented here is the ${}^7\text{Li}$ spectrum of the cathode material $\text{LiFe}_{0.5}\text{Mn}_{0.5}\text{PO}_4$. The small dispersion of the ${}^7\text{Li}$ isotropic shift (approximately 90 ppm) and the presence of inhomogeneous broadening of the lines (also approximately 90 ppm), and ABMS effects [97], make it impossible to resolve the individual isotropic shifts. Fig. 26 shows a series of one-dimensional spectra that have been acquired with various DANTE pulse sequences with varying K , at 60 kHz MAS which is sufficient for the neighbouring sidebands to be resolved from each other, and these can be compared with the reference spectrum acquired with a double-SHAP-echo sequence in Fig. 18(c). The DANTE sequences were incorporated into a spin-echo sequence of the form $P_1-\tau_r-P_2-\tau_r\text{-acq.}$, where P_1 is a sequence D_K^{10K} optimised for excitation, P_2 is a sequence D_K^{20K} which is double the length of P_1 , and is therefore optimised for refocusing. All pulses have a peak RF field amplitude of 56.8 kHz, and the carrier frequency was set so that the centre of gravity of the centreband was on

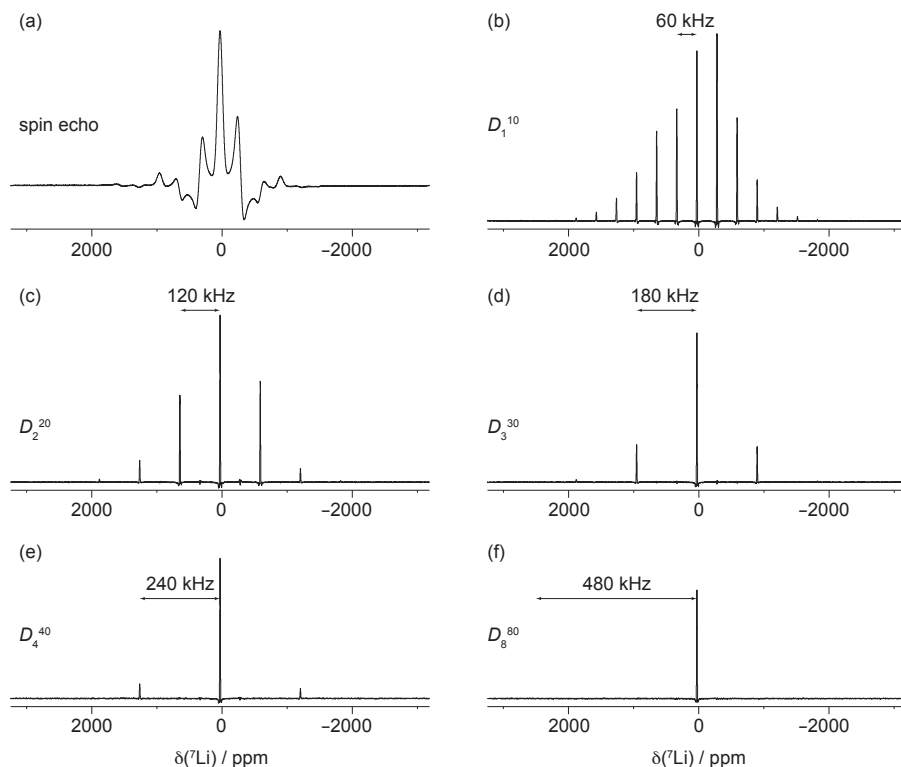


Figure 26: Experimental ${}^7\text{Li}$ spectra acquired from the cathode material $\text{LiFe}_{0.5}\text{Mn}_{0.5}\text{PO}_4$ using DANTE excitation sequences. For all spectra the pulse sequence was a spin-echo of the form $P_1-\tau_r-P_2-\tau_r\text{-acq.}$, with the RF field amplitude of all pulses set to 56.8 kHz, and the MAS frequency 60 kHz giving a rotor period τ_r of 16.67 μs . The transmitter offset was set to be resonant with the centreband. In (a) is shown the conventional spin-echo spectrum, where P_1 and P_2 are conventional 90° and 180° pulses of lengths 4.4 and 8.8 μs . DANTE spin-echo spectra are shown in (b)–(f) where P_1 is an excitation DANTE sequence D_K^N of total length 166.67 μs , comprising N small-flip-angle pulses of length $0.44/K$ μs , and P_2 is a refocussing DANTE sequence D_K^{2N} of total length 333.33 μs , comprising $2N$ small-flip-angle pulses of length $0.44/K$ μs . Spectrum (b) was acquired with the sequence $D_1^{10}-\tau_r-D_1^{20}-\tau_r\text{-acq.}$, and shows sidebands separated by the spinning frequency 60 kHz. Spectrum (c) was acquired using the sequence $D_2^{20}-\tau_r-D_2^{40}-\tau_r\text{-acq.}$ comprising the overtone DANTE sequences, and only shows the sidebands with even sideband order. Spectra (d) and (e) were acquired with the sequences $D_3^{30}-\tau_r-D_3^{60}-\tau_r\text{-acq.}$ and $D_4^{40}-\tau_r-D_4^{80}-\tau_r\text{-acq.}$ and show sidebands spaced every 180 and 240 kHz respectively. The DANTE pulses used in the excitation of spectrum (f) result in observation of only the centreband, as the ± 8 -order sidebands are of negligible intensity, and the spectrum is exactly the same the one that would be observed following excitation with single-sideband-selective 90° and 180° pulses of lengths 166.67 and 333.33 μs respectively, and RF field amplitude 1.5 kHz [18, 39]. Each spectrum was acquired at 11.74 T, and with 8192 scans.

resonance. Note that as K is increased the number of pulses in each sequence is increased proportionately so that the compared sequences have the same overall length, with P_1 and P_2 being of duration $166.67 \mu\text{s}$ and $333.33 \mu\text{s}$ respectively. The overall spin-echo sequence was therefore $533.33 \mu\text{s}$ in length, which is less than one third of T_2' and losses due to relaxation and coherent dephasing were negligible.

The spectrum shown in Fig. 26(a) was acquired with a conventional spin-echo sequence with the same RF field amplitude to serve as a comparison. The excitation is clearly not broadband when compared with the spectrum in Fig. 1(c), with the sideband intensities following a sinc function. It is also evident that the lines are considerably broadened by inhomogeneous effects, with the expected homogeneous broadening being an order of magnitude lower given the bulk T_2' of 1.59 ms. The spectra in Fig. 26(b) to Fig. 26(f) were recorded using the DANTE sequences with increasing K . The spectrum acquired following excitation with the echo sequence $D_1^{10}-\tau_r-D_1^{20}-\tau_r$ is shown in Fig. 26(b). Broadly speaking the pattern of sideband intensities matches that in the reference spectrum in Fig. 1(c) indicating that the excitation is 100% efficient when the pulse is resonant with the isotropic shift. Nevertheless we see considerable line narrowing with only the central parts of each sideband being excited, and the width of the sidebands being given by a combination of the homogeneous linewidth and the bandwidth of each excitation lobe of the DANTE sequence. The inhomogeneous broadening results is due to a spatial variation of the magnetic field throughout the sample, with the result that the chemical shifts are also vary with position in the sample. Each site is therefore only excited in the part of the sample where the isotropic shift is resonant with the carrier frequency. The spectrum is therefore a superposition of responses from all sites, and *not* a single site that has been extracted. The remaining spectra were acquired following a DANTE spin echo where the number of pulses per rotor period was (c) 2, (d) 3, (e) 4, and (f) 8. The form of the spectra follows that expected from the simulations in Fig. 23 with the separation between neighbouring sidebands being equal to $60 \times K$ kHz. We also note that the relative intensities of the surviving sidebands in each spectrum match the relative intensities in the spectrum in Fig. 23(b) where all sidebands are observed. The spectrum in Fig. 23(f) contains only the centreband, and so could also have been acquired using centreband-selective 90° and 180° of duration

166.67 μs and 333.33 μs respectively, and an RF field amplitude of 1.5 kHz.

The second experimental example is the more challenging case of ^{31}P NMR of the same material. The isotropic shifts of the multiple ^{31}P sites are distributed over a wide range of 4500 ppm with considerable inhomogeneous broadening due to ABMS effects (approximately 90 ppm) [97]. In addition the relaxation times are considerably shorter than for ^7Li , with the T_1 relaxation times at 500 MHz field varying for the different sites from 261 μs for the all-Mn site to 524 μs for the all-Fe site. The T_2' values vary from 132 μs (all-Mn) to 334 μs (all-Fe). The ^{31}P spectrum has already been assigned for this material using a combination of isotropic MAS NMR spectroscopy and density functional theory (DFT) calculations. The sites can be partially resolved in an adiabatic magic-angle turning (aMAT) experiment, which uses the SHAPs introduced in Section 7.3 as refocusing pulses [33]. The spectrum acquired at 60 kHz MAS, which is shown in Fig. 27(a), shows that the 32 ^{31}P are partially resolved into eight distinct groups with the isotropic shifts given in the indirect dimension. The RF field amplitude of all the pulses was 417 kHz. The one-dimensional spectra in Fig. 27(b)–(h) were acquired following excitation with the same DANTE spin echo applied at different carrier frequencies as indicated by the arrows. The short T_2' dephasing times required the DANTE elements to be shortened considerably compared to those used for ^7Li . The DANTE sequences used for excitation and refocusing were therefore a D_1^3 sequence of 50 μs length, and a D_1^6 sequence of length 100 μs respectively, and used a maximum RF field amplitude of 417 kHz. In all seven cases we obtain similar spectra with narrow sidebands that are observed at frequencies separated from the carrier frequency by an integer multiple of the spinning frequency of 60 kHz. As was the case for ^7Li each spectrum does not represent a single site, as each sideband manifold is considerably broader than those observed in the aMAT spectrum. Therefore, in each case, we observe a superposition of multiple sites which are, in general, excited in different parts of the sample due to magnetic field inhomogeneity.

In summary the DANTE sequence can deliver a broader excitation response over a single sideband manifold when the carrier is resonant with one of the sidebands, but there are a number of potential pitfalls that must be noted, especially when dealing with systems that have a number of chemically distinct sites with unknown chemical

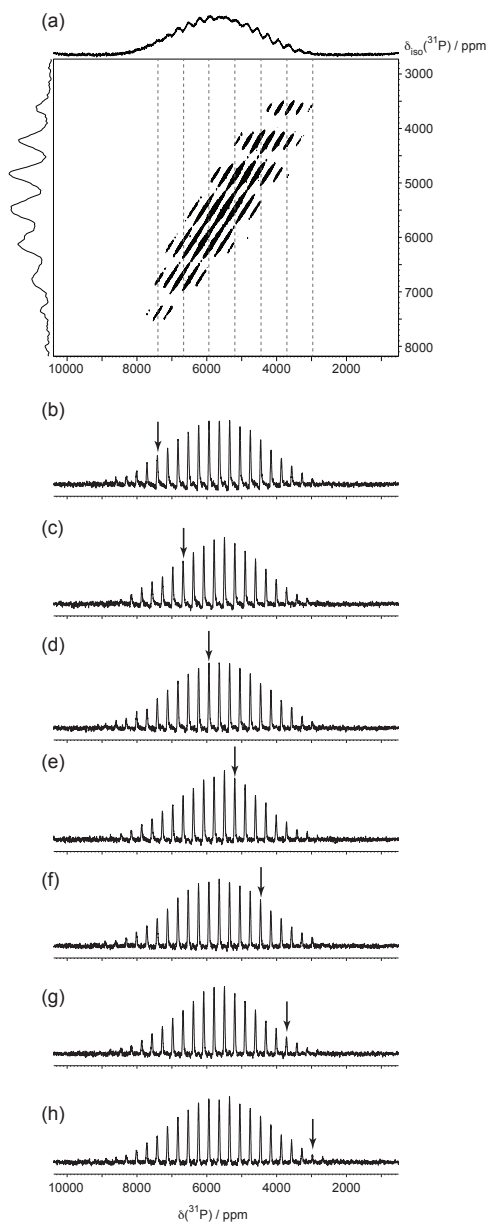


Figure 27: Comparison of experimental ^{31}P DANTE spectra (b)–(h) as a function of carrier frequency and an adiabatic magic-angle turning (aMAT) spectrum [33] (a) acquired from the cathode material $\text{LiFe}_{0.5}\text{Mn}_{0.5}\text{PO}_4$. All spectra were acquired at 60 kHz MAS. The two-dimensional aMAT spectrum was acquired using a non-selective 90° pulse, and six tanh/tan SHAPs that swept through 5 MHz in $50 \mu\text{s}$. All pulses were applied at 417 kHz RF field amplitude. 150 complex increments were acquired with 2656 scans per increment. The one-dimensional DANTE spectra were acquired with a spin-echo sequence of the form $D_1^3-\tau_r-D_1^6-\tau_r-\text{aqc.}$, with the carrier placed at the positions in the spectrum indicated by the vertical arrows. The excitation sequence D_1^3 was of total duration $50 \mu\text{s}$, and the refocussing element D_1^6 of length $100 \mu\text{s}$. All DANTE pulses were applied with a maximum RF field amplitude of 417 kHz. Each DANTE spectrum was acquired at 11.74 T, and with 32768 scans.

shift parameters. Specifically the DANTE sequence in its present form cannot be relied upon to deliver uniform excitation or inversion across the whole spectral range for all sites as many may not be excited. In the presence of inhomogeneous broadening the observed spectrum contains a superposition of sideband manifolds from different sites, and so the sequence cannot be used to “pull out” sideband manifolds from different sites, as can be appreciated readily from the example presented in Fig. 27.

In order to achieve a true, uniform excitation this sequence needs to be implemented in combination with a frequency stepping scheme, similar to that described in Section 7.2, in which we acquire a number of spectra over a frequency range of the order of the spinning frequency with a step size matching the bandwidth in each individual spikelet of the excitation profile. However this will make it inconvenient to incorporate into more complex multi-dimensional NMR experiments. Nevertheless with the advent of probes capable of MAS frequencies of 100 kHz and above the DANTE scheme, as in the case of the S^3 APs, may become an important alternative to SHAPs.

8. Concluding remarks and recommendations for practical broadband NMR

Following on from the detailed analysis of the RF pulse schemes presented above we now provide a series of recommendations for obtaining the best possible NMR excitation profile of paramagnetic species. We will examine how well the various sequences satisfy the three conditions for broadband NMR that were set out in Section 3, which are repeated here:

1. For different nuclear sites, the pulse must excite, invert, or refocus over a sufficient range of isotropic shifts;
2. For different nuclear sites, the pulse must excite, invert, or refocus over a sufficient range of shift anisotropies;
3. For each individual site, the pulse must achieve 100% excitation, inversion, or refocussing for all crystallite orientations.

The ease of incorporation of the various schemes into more sophisticated pulse sequences will also be evaluated. During this discussion there are two additional points

that should also be borne in mind when conducting NMR experiments of solid paramagnetic materials. Firstly an experiment based on the spin echo is required in order to obtain uniform phase across the large spectral window often needed for the large range of shifts and shift anisotropies, to suppress any signal from the probe background that may pollute the spectrum, and to recover possible signal loss due to inhomogeneous decay effects during the receiver dead time. We will therefore consider pulses for both excitation and inversion/refocussing. Secondly Ishii et al. also recommended that one uses a small-outer-diameter rotor and to spin at the maximum available MAS frequency [16]. This not only reduces the number of spinning sidebands, thus increasing both resolution and sensitivity, but also reduces the length of the rotor period and therefore the overall duration of the spin-echo sequences, SHAP, and DANTE elements. This is particularly important when studying samples where the nuclear spins exhibit short coherence lifetimes T_2' . An additional advantage of using a small diameter rotor is that the more favourable filling factor allows one to obtain larger RF field amplitudes using conventional power levels.

Conventional constant-amplitude pulses satisfy all three criteria for both excitation and inversion/refocussing if the RF field amplitude is sufficiently high that it dominates the range of shifts and shift anisotropies. This may be the case for 90° excitation pulses which have a bandwidth of isotropic shifts of $3.16\omega_1$ within which we obtain 90% excitation efficiency. For instance if we use an RF field amplitude of 400 kHz, which can be obtained for ^{31}P on a Bruker 1.3 mm probe, the isotropic shift bandwidth is 1264 kHz. On the other hand the conventional 180° pulses used for inversion and refocussing have a somewhat smaller bandwidth of $0.46\omega_1$ which, for a 400 kHz pulse, is equal to 184 kHz. The refocussing pulse is therefore the unequivocal weak link in a conventional spin echo.

The shortcomings can be addressed by employing frequency stepping at the expense of increased experiment time, and the inconvenience of retuning the probe between the acquisition of each new sub-spectrum. These disadvantages make it extremely difficult, if not impossible, to incorporate the frequency-stepping scheme into more complex experiments.

The short, high-powered adiabatic pulses (SHAPs) can be used for broadband inversion and refocussing as they satisfy all three criteria for broadband NMR under MAS conditions. The isotropic shift bandwidth is also considerably larger than for conventional pulses, typically taking values up to 2 MHz for an RF field amplitude of 400 kHz (Fig. 25). They are therefore efficacious when used for refocussing in spin echoes, but cannot currently be used for excitation.

The single-sideband-selective adiabatic inversion pulses (S^3 APs), when applied to the centreband of a spinning sideband manifold, satisfy the last two criteria for broadband NMR, namely inversion over a range of SAs from zero to a maximum of the order of 100 kHz for all crystallite orientations. However the range of isotropic shifts for which inversion is achieved is more limited and must be in the vicinity of $\omega_{\text{tx}} + k\omega_{\text{r}}$ where k is an integer. The inversion profile as a function of isotropic shift therefore contains a number of ‘holes’ in which inversion is comparatively poor, and so the first condition is not satisfied. In addition excitation has yet to be implemented with these pulses.

The same considerations also apply to delays alternating with nutation for tailored excitation (DANTE) in that the last two criteria are satisfied, but the first is not. The range of isotropic shifts that is inverted is actually smaller than for the S^3 AP as each individual spikelet in the inversion profile has a narrower bandwidth than the low-power adiabatic pulse, in exactly the same way that adiabatic inversion pulses are more broadband than conventional RF pulses. However DANTE can be applied to excitation if the first criterion is not too restrictive for the sample under consideration.

For spin-1/2 systems where the spectra are within the probe bandwidth, the best choice of excitation pulse is currently the conventional constant-amplitude 90° pulse. We expect that the bandwidth is not the largest that is available, but considering the current state of the art it is certainly the safest choice with no holes in the excitation window of isotropic shifts. In addition the short pulse length renders relaxation losses negligible even for very short coherence lifetimes T_2' of the order of 10–100 μs . To complete the spin-echo sequence we recommend the SHAPs for coherence refocussing

to give the following

$$90^\circ - \tau_r/2 - \text{SHAP} - \tau_r/2 - \tau_r/2 - \text{SHAP} - \tau_r/2 - \text{aqc.} \quad (164)$$

with a phase cycle where the cycles of both SHAPs are nested according to EXOR-CYCLE. The choice of the SHAP reflects that, out of the currently available pulse schemes, it is the one that best satisfies the three criteria for broadband NMR and, with pulse lengths of approximately $50 \mu\text{s}$, can also be used for fast-relaxing systems. Both of these properties make it more suitable than either the $S^3\text{AP}$ or DANTE for working with paramagnetic systems containing several nuclear sites with unknown isotropic shifts, or with significant inhomogeneous broadening of the sidebands. This sequence can also be used for quadrupolar nuclei with relatively small quadrupole moments C_Q , such as ${}^6\text{Li}$ and ${}^7\text{Li}$ [34, 35]. The SHAPs have also been demonstrated versatility as they have been incorporated into more complex sequences including CPMG [74] and the two-dimensional sideband-separation experiment aMAT [33].

There are two instances where the above double SHAP echo is not the best choice of sequence. Systems containing nuclei with particularly large PREs will suffer from very large intensity losses during the sequence, and if the T_2' is particularly short, say of the order of $10 \mu\text{s}$ there will be no signal remaining at the end of the sequence as the combined length of the two SHAPs is of the order of $100 \mu\text{s}$. In this case it will be best to use either a conventional spin-echo sequence

$$90^\circ - \tau_r - 180^\circ - \tau_r - \text{aqc.}, \quad (165)$$

or a stimulated-echo sequence of the form

$$90^\circ - \tau_r - 90^\circ - \tau_z - 90^\circ - \tau_r - \text{aqc.}, \quad (166)$$

combined with appropriate phase cycling so that the coherence order is +1 during the first delay τ_r , 0 during the z -filter delay τ_z , and -1 during the second delay τ_r [101]. The stimulated echo has the advantage over the conventional spin echo in that it does not suffer from the low bandwidth of the 180° pulse but, in the absence of relaxation

effects, it has a maximum sensitivity equal to half that of the spin echo as only half the available signal is refocused. The stimulated echo has also been used as part of a MAT sequence with greater bandwidth than the conventional form of the experiment with five 180° pulses [101]. Secondly the performance of the SHAP can break down when applied to quadrupolar nuclei with moderate-to-high C_Q values, such as ^{23}Na , ^{27}Al , or ^{17}O . This is ascribed to the SHAP not having a sufficiently large bandwidth to manipulate the central transition and satellites so that all are excited quantitatively, nor being selective to the central transition due to the necessity of using a sweep width and RF field amplitude in order to counter the paramagnetic effects. In these cases the best choice of sequence is a conventional spin echo [102, 103].

9. Acknowledgements

We acknowledge Prof. Lyndon Emsley and Mr Kevin J. Sanders (Ecole Normale Supérieure de Lyon), Prof. Clare P. Grey and Ms Raphaële J. Clément (University of Cambridge), Dr Dominique Massiot and Dr Michaël Deschamps (Université d'Orléans), and Prof. Philip J. Grandinetti (Ohio State University) for many useful discussions about various aspects of broadband NMR sequences, adiabaticity, and the jolting frame. We are grateful to Prof. M. Stanley Whittingham and Dr Joel K. Miller (State University of New York at Binghamton) for supplying the sample of $\text{LiFe}_{0.5}\text{Mn}_{0.5}\text{PO}_4$. A.J.P. was supported by the LABEX iMUST (ANR-10-LABX-0064) of the Université de Lyon, within the program Investissements d'Avenir (ANR-11-IDEX-0007) operated by the Agence Nationale de la Recherche (ANR). The research leading to these results has received funding from the People Programme (Marie Curie Actions Initial Training Networks (ITN)) of the European Union's Seventh Framework Programme FP7/2007-2013/ under REA grant agreement no. 317127, the "pNMR" project.

References

- [1] L. Emsley, I. Bertini, *Frontiers in solid-state NMR technology*, *Acc. Chem. Res.* 46 (2013) 1912–1913.

- [2] H. Heise, F. H. Köhler, M. Herker, W. Hiller, Inter- and intramolecular spin transfer in molecular magnetic materials. solid-state NMR spectroscopy of paramagnetic metallocenium ions, *J. Am. Chem. Soc.* 124 (2002) 10823–10832.
- [3] F. H. Köhler, R. Lescouëzec, Highly resolved spin-density distribution in the Prussian-blue precursors $\text{Cs}_2\text{K}[\text{Fe}(\text{CN})_6]$ and $\text{Cs}_2\text{K}[\text{Mn}(\text{CN})_6]$, *Angew. Chem. Int. Ed.* 43 (2004) 2571–2573.
- [4] C. P. Grey, N. Dupre, Nmr studies of cathode materials for lithium-ion rechargeable batteries, *Chem. Rev.* 104 (2004) 4493–4512.
- [5] N. P. Wickramasinghe, M. Shaibat, Y. Ishii, Enhanced sensitivity and resolution in H-1 solid-state NMR spectroscopy of paramagnetic complexes under very fast magic angle spinning, *J. Am. Chem. Soc.* 127 (2005) 5796–5797.
- [6] G. Kervern, G. Pintacuda, Y. Zhang, E. Oldfield, C. Roukoss, E. Kuntz, E. Herdtweck, J. M. Basset, S. Cadars, L. Emsley, Solid-state NMR of a paramagnetic DIAD-Fe-II catalyst: Sensitivity, resolution enhancement, and structure-based assignments, *J. Am. Chem. Soc.* 128 (2006) 13545–13552.
- [7] A. Flambard, F. H. Köhler, R. Lescouëzec, Revisiting Prussian blue analogues with solid-state MAS NMR spectroscopy: Spin density and local structure in $[\text{Cd}_3[\text{Fe}(\text{CN})_6]_2] \cdot 15\text{H}_2\text{O}$, *Angew. Chem. Int. Ed.* 48 (2009) 1673–1676.
- [8] I. Bertini, L. Emsley, M. Lelli, C. Luchinat, J. F. Mao, G. Pintacuda, Ultrafast MAS solid-state NMR permits extensive C-13 and H-1 detection in paramagnetic metalloproteins, *J. Am. Chem. Soc.* 132 (2010) 5558–5559.
- [9] J. Estephane, E. Groppo, J. G. Vitillo, A. Damin, D. Gianolio, C. Lamberti, S. Bordiga, E. A. Quadrelli, J. M. Basset, G. Kervern, L. Emsley, G. Pintacuda, A. Zecchina, A multitechnique approach to spin-flips for $\text{Cp}_2\text{Cr}(\text{II})$ chemistry in confined state, *J. Phys. Chem. C* 114 (2010) 4451–4458.
- [10] M. J. Knight, A. J. Pell, I. Bertini, I. C. Felli, L. Gonnelli, R. Pierattelli, T. Herrmann, L. Emsley, G. Pintacuda, Structure and backbone dynamics of a micro-

crystalline metalloprotein by solid-state NMR, *Proc. Natl. Acad. Sci. USA* 109 (2012) 11095–11100.

- [11] C. Luchinat, G. Parigi, E. Ravera, M. Rinaldelli, Solid-state NMR crystallography through paramagnetic restraints, *J. Am. Chem. Soc.* 134 (2012) 5006–5009.
- [12] A. W. MacGregor, L. A. O’Dell, R. W. Schurko, New methods for the acquisition of ultra-wideline solid-state NMR spectra of spin-1/2 nuclides, *J. Magn. Reson.* 208 (2011) 103–111.
- [13] L. A. O’Dell, A. J. Rossini, R. W. Schurko, Acquisition of ultra-wideline NMR spectra from quadrupolar nuclei by frequency-stepped WURST-QCPMG, *Chem. Phys. Lett.* 468 (2009) 330–335.
- [14] K. Harris, A. Lupulescu, B. E. G. Lucier, L. Frydman, R. W. Schurko, Broadband adiabatic inversion pulses for cross polarization in wideline solid-state NMR spectroscopy, *J. Magn. Reson.* 224 (2012) 28–47.
- [15] E. R. Andrew, A. Bradbury, R. G. Eades, Removal of dipolar broadening of nuclear magnetic resonance spectra of solids by specimen rotation, *Nature* 183 (1959) 1802–1803.
- [16] Y. Ishii, N. P. Wickramasinghe, S. Chimon, A new approach in 1D and 2D C-13 high-resolution solid-state NMR spectroscopy of paramagnetic organometallic complexes by very fast magic-angle spinning, *J. Am. Chem. Soc.* 125 (2003) 3438–3439.
- [17] S. W. Sparks, P. D. Ellis, ¹⁹⁵Pt shielding tensors in potassium hexachloroplatinate(IV) and potassium tetrachloroplatinate(II), *J. Am. Chem. Soc.* 108 (1986) 3215–3218.
- [18] A. J. Pell, R. J. Clément, C. P. Grey, L. Emsley, G. Pintacuda, Frequency-stepped acquisition in nuclear magnetic resonance spectroscopy under magic angle spinning, *J. Chem. Phys.* 138 (2013) 114201.

- [19] G. Kervern, G. Pintacuda, L. Emsey, Fast adiabatic pulses for solid-state NMR of paramagnetic systems, *Chem. Phys. Lett.* 435 (2007) 157–162.
- [20] R. Siegel, T. T. Nakashima, R. E. Wasylishen, Sensitivity enhancement of NMR spectra of half-integer spin quadrupolar nuclei in solids using hyperbolic secant pulses, *J. Magn. Reson.* 184 (2007) 85–100.
- [21] K. K. Dey, S. Prasad, J. T. Ash, M. Deschamps, P. J. Grandinetti, Spectral editing in solid-state MAS NMR of quadrupolar nuclei using selective satellite inversion, *J. Magn. Reson.* 185 (2007) 326–330.
- [22] T. T. Nakashima, R. E. Wasylishen, R. Siegel, K. J. Ooms, Sensitivity enhancement of solid-state NMR spectra of half-integer spin quadrupolar nuclei: Double- or single-frequency sweeps? Insights from the hyperbolic secant experiment, *Chem. Phys. Lett.* 450 (2008) 417–421.
- [23] T. T. Nakashima, R. Teymoori, R. E. Wasylishen, Using hyperbolic secant pulses to assist characterization of chemical shift tensors for half-integer spin quadrupolar nuclei in MAS powder samples, *Magn. Reson. Chem.* 47 (2009) 465–471.
- [24] A. J. Pell, G. Kervern, L. Emsley, M. Deschamps, D. Massiot, P. J. Grandinetti, G. Pintacuda, Broadband inversion for MAS NMR with single-sideband-selective adiabatic pulses, *J. Chem. Phys.* 134 (2011) 024117.
- [25] V. Vitzthum, M. A. Caporini, S. Ulzega, G. Bodenhausen, Broadband excitation and indirect detection of nitrogen-14 in rotating solids using Delays Alternating with Nutation (DANTE), *J. Magn. Reson.* 212 (2011) 234–239.
- [26] T. L. Hwang, A. J. Shaka, Water suppression that works. Excitation sculpting using arbitrary wave-forms and pulsed-field gradients, *J. Magn. Reson. Ser. A* 112 (1995) 275–279.
- [27] K. Stott, J. Stonehouse, J. Keeler, T. L. Hwang, A. J. Shaka, Excitation sculpting in high-resolution nuclear magnetic resonance spectroscopy: Application to selective NOE experiments, *J. Am. Chem. Soc.* 117 (1995) 4199–4200.

- [28] A. Pines, M. G. Gibby, J. S. Waugh, Proton-enhanced NMR of dilute spins in solids, *J. Chem. Phys.* 59 (1973) 569–590.
- [29] N. P. Wickramasinghe, Y. Ishii, Sensitivity enhancement, assignment, and distance measurement in C-13 solid-state NMR spectroscopy for paramagnetic systems under fast magic angle spinning, *J. Magn. Reson.* 181 (2006) 233–243.
- [30] S. K. K. Swamy, A. Karczmarzka, M. Makowska-Janusik, A. Kassiba, J. Dittmer, Solid-state NMR correlation experiments and distance measurements in paramagnetic metalorganics exemplified by Cu-Cyclam, *ChemPhysChem* 14 (2013) 1864–1870.
- [31] E. L. Hahn, Spin echoes, *Phys. Rev.* 80 (1950) 580–594.
- [32] G. Kervern, A. D'Aleo, O. Maury, L. Emsley, G. Pintacuda, Crystal structure determination of powdered paramagnetic lanthanide complexes by proton NMR, *Angew. Chem. Int. Ed. Engl.* 48 (2009) 3082–3086.
- [33] R. J. Clément, A. J. Pell, D. S. Middlemiss, F. C. Strobridge, J. K. Miller, M. S. Whittingham, L. Emsley, C. P. Grey, G. Pintacuda, Spin-transfer pathways in paramagnetic lithium transition metal phosphates from combined broadband isotropic solid-state MAS NMR spectroscopy and DFT calculations., *J. Am. Chem. Soc.* 134 (2012) 17178–17185.
- [34] M. Bini, S. Ferrari, C. Ferrara, M. C. Mozzati, D. Capsoni, A. J. Pell, G. Pintacuda, P. Canton, P. Mustarelli, Polymorphism and magnetic properties of Li_2MSiO_4 (M = Fe, Mn) cathode materials, *Sci. Rep.* 3 (2013) 3452.
- [35] J. Xu, R. J. Lee, R. J. Clément, X. Yu, M. Leskes, A. J. Pell, G. Pintacuda, X.-Q. Yang, C. P. Grey, Y. S. Meng, Identifying the critical role of Li substitution in $\text{P2-Na}_x[\text{Li}_y\text{Ni}_z\text{Mn}_{1-y-z}]\text{O}_2$ ($0 < x, y, z < 1$) intercalation cathode materials for high energy Na-ion batteries, *Chem. Mater.* 26 (2014) 1260–1269.
- [36] F. C. Strobridge, D. S. Middlemiss, A. J. Pell, M. Leskes, R. J. Clément, F. Pourpoint, Z. Lu, J. V. Hanna, G. Pintacuda, L. Emsley, A. Samoson, C. P. Grey,

Characterising local environments in high energy density Li-ion battery cathodes: a combined NMR and first principles study of $\text{LiFe}_x\text{Co}_{1-x}\text{PO}_4$, *J. Mater. Chem. A* 2 (2014) 11948–11957.

- [37] M. Mehring, *Principles of High-Resolution NMR in Solids*, Springer Verlag, Berlin, 1983.
- [38] M. M. Maricq, J. S. Waugh, NMR in rotating solids, *J. Chem. Phys.* 70 (1979) 3300–3316.
- [39] P. Caravatti, G. Bodenhausen, R. R. Ernst, Selective pulse experiments in high-resolution solid-state NMR, *J. Magn. Reson.* 55 (1983) 88–103.
- [40] A. K. Padhi, K. S. Nanjundaswamy, J. B. Goodenough, Phospho-olivines as positive-electrode materials for rechargeable lithium batteries, *J. Electrochem. Soc.* 144 (1997) 1188–1194.
- [41] J. Kim, D.-H. Seo, S.-W. Kim, Y.-U. Park, K. Kang, Mn based olivine electrode material with high power and energy, *Chem. Commun.* 46 (2010) 1305–1307.
- [42] D. S. Middlemiss, A. J. Ilott, R. J. Clément, F. C. Strobridge, C. P. Grey, Density functional theory-based bond pathway decompositions of hyperfine shifts: Equipping solid-state NMR to characterize atomic environments in paramagnetic materials, *Chem. Mater.* 25 (2013) 1723–1734.
- [43] T. L. Hwang, P. C. M. van Zijl, M. Garwood, Fast broadband inversion by adiabatic pulses, *J. Magn. Reson.* 133 (1998) 200–203.
- [44] M. Veshkort, R. G. Griffin, SPINEVOLUTION: A powerful tool for the simulation of solid and liquid state nmr experiments, *J. Magn. Reson.* 178 (2006) 248–282.
- [45] M. Edén, M. H. Levitt, Computation of orientational averages in solid-state nmr by Gaussian spherical quadrature, *J. Magn. Reson.* 132 (1998) 220–239.
- [46] I. Bertini, C. Luchinat, G. Parigi, *Solution NMR of paramagnetic molecules; application to metalloproteins and models*, Elsevier, London, 2001.

- [47] I. Bertini, C. Luchinat, G. Parigi, Magnetic susceptibility in paramagnetic NMR, *Prog. Nucl. Magn. Reson. Spectrosc.* 40 (2002) 249–273.
- [48] M. Kaupp, F. H. Köhler, Combining NMR spectroscopy and quantum chemistry as tools to quantify spin density distributions in molecular magnetic compounds, *Coord. Chem. Rev.* 253 (2009) 2376–2386.
- [49] N. F. Ramsey, Magnetic shielding of nuclei in molecules, *Phys. Rev.* 78 (1950) 699–703.
- [50] T. O. Pennanen, J. Vaara, Nuclear magnetic resonance chemical shift in an arbitrary electronic spin state, *Phys. Rev. Lett.* 100 (2008) 133002.
- [51] S. Moon, S. Patchkovskii, *Calculation of NMR and EPR Parameters: Theory and Applications*, Wiley-VCH, Weinheim, 2004, Ch. Chapter 20. First-Principles Calculations of Paramagnetic NMR Shifts.
- [52] A. Abragam, B. Bleaney, *Electron Paramagnetic Resonance of Transition Ions*, Oxford University Press, Oxford, 1970.
- [53] E. R. Andrew, A. Bradbury, R. G. Eades, Nuclear magnetic resonance spectra from a crystal rotated at high speed, *Nature* 182 (1958) 1659.
- [54] M. H. Levitt, Why do spinning sidebands have the same phase?, *J. Magn. Reson.* 82 (1989) 427–433.
- [55] P. Tekely, To what extent does the centreband and each spinning sideband contain contributions from the different crystallites of the powder sample?, *Solid State Nucl. Magn. Reson.* 14 (1999) 33–41.
- [56] M. G. Munowitz, R. G. Griffin, Two-dimensional nuclear magnetic resonance in rotating solids: an analysis of line shapes in chemical shift-dipolar spectra, *J. Chem. Phys.* 76 (1982) 2848–2858.
- [57] E. Olejniczak, S. Vega, R. G. Griffin, Multiple pulse NMR in rotating solids, *J. Chem. Phys.* 81 (1984) 4804–4817.

- [58] O. N. Antzutkin, S. C. Shekar, M. H. Levitt, Two-dimensional sideband separation in magic-angle-spinning NMR, *J. Magn. Reson. Ser. A* 115 (1995) 7–19.
- [59] A. Abragam, *Principles of Nuclear Magnetism*, Oxford University Press, Oxford, 1961.
- [60] R. R. Ernst, G. Bodenhausen, A. Wokaun, *Principles of nuclear magnetic resonance in one and two dimensions*, Oxford University Press, Oxford, 1987.
- [61] M. H. Levitt, Symmetrical composite pulse sequences for NMR population inversion. II. compensation of resonance offset, *J. Magn. Reson.* 50 (1982) 95–110.
- [62] M. Garwood, L. DelaBarre, The return of the frequency sweep: Designing adiabatic pulses for contemporary NMR, *J. Magn. Reson.* 153 (2001) 155–177.
- [63] J. Baum, R. Tycko, A. Pines, Broad-band and adiabatic inversion of a 2-level system by phase-modulated pulses, *Phys. Rev. A* 32 (1985) 3435–3447.
- [64] R. Q. Fu, G. Bodenhausen, Broad-band decoupling in NMR with frequency-modulated chirp pulses, *Chem. Phys. Lett.* 245 (1995) 415–420.
- [65] E. Kupce, R. Freeman, Stretched adiabatic pulses for broadband spin inversion, *J. Magn. Reson. Ser. A* 117 (1995) 246–256.
- [66] E. Kupce, R. Freeman, Adiabatic pulses for wide-band inversion and broad-band decoupling, *J. Magn. Reson. Ser. A* 115 (1995) 273–276.
- [67] E. Kupce, R. Freeman, Optimized adiabatic pulses for wideband spin inversion, *J. Magn. Reson. Ser. A* 118 (1996) 299–303.
- [68] M. Deschamps, G. Kervern, D. Massiot, G. Pintacuda, L. Emsley, P. J. Grandinetti, Superadiabicity in magnetic resonance, *J. Chem. Phys.* 129 (2008) 204100.
- [69] G. Bodenhausen, R. Freeman, G. A. Morris, A simple pulse sequence for selective excitation in Fourier transform NMR, *J. Magn. Reson.* 23 (1976) 171–175.

- [70] G. A. Morris, R. Freeman, Selective excitation in Fourier transform nuclear magnetic resonance, *J. Magn. Reson.* 29 (1978) 433–462.
- [71] D. Carnevale, V. Vitzthum, O. Lafon, J. Trébosc, J.-P. Amoureux, G. Bodenhausen, Broadband excitation in solid-state NMR of paramagnetic samples using Delays Alternating with Nutation for Tailored Excitation ('Para-DANTE'), *Chem. Phys. Lett.* 553 (2012) 68–76.
- [72] D. M. Brink, G. R. Satchler, *Angular Momentum*, Clarendon Press, Oxford, 1993.
- [73] S. Conolly, G. Glover, D. Nishimura, A. Macovski, A reduced power selective adiabatic spin-echo pulse sequence, *Magn. Reson. Med.* 18 (1991) 28–38.
- [74] G. Kervern, S. Steuernagel, F. Engelke, G. Pintacuda, L. Emsley, Absence of Curie relaxation in paramagnetic solids yields long H-1 coherence lifetimes, *J. Am. Chem. Soc.* 129 (2007) 14118.
- [75] A. J. Pell, G. Pintacuda, L. Emsley, Single crystal nuclear magnetic resonance in spinning powders, *J. Chem. Phys.* 135 (2011) 144201.
- [76] U. Haeberlen, J. S. Waugh, Coherent averaging effects in magnetic resonance, *Phys. Rev.* 175 (1968) 453–467.
- [77] J. H. van Vleck, The dipolar broadening of magnetic resonance lines in crystals, *Phys. Rev.* 74 (1948) 1168–1183.
- [78] H. Primas, Generalized perturbation theory in operator form, *Rev. Mod. Phys.* 35 (1963) 710–712.
- [79] M. Goldman, P. J. Grandinetti, A. Llor, Z. Olejniczak, J. R. Sachleben, J. Zwanziger, Theoretical aspects of higher-order truncations in solid-state nuclear-magnetic-resonance, *J. Chem. Phys.* 97 (1992) 8947–8960.
- [80] M. Leskes, P. K. Madhu, S. Vega, Floquet theory in solid-state nuclear magnetic resonance, *Prog. NMR. Spectrosc.* 57 (2010) 345–380.

- [81] M. Goldman, P. J. Grandinetti, A. Llor, Z. Olejniczak, R. J. Sachleben, J. W. Zwanziger, Theoretical aspects of higher-order truncations in solid-state nuclear magnetic resonance, *J. Chem. Phys.* 97 (1992) 8947–8960.
- [82] M. T. Sananes, A. Tuel, J. C. Volta, A study by ^{31}P NMR spin-echo mapping of VPO catalysts: I. characterization of the reference phases, *J. Catal.* 145 (1994) 251–255.
- [83] M. T. Sananes, A. Tuel, J. C. Volta, Characterization of different precursors and activated vanadium phosphate catalysis by ^{31}P NMR spin echo mapping, *J. Catal.* 148 (1994) 395–398.
- [84] M. T. Sananes, A. Tuel, Magnetic properties of vanadium phosphorus oxide catalysts studied by spin echo mapping ^{31}P NMR, *J. Chem. Soc., Chem. Commun.* (1995) 1323–1324.
- [85] Y. Y. Tong, Nuclear spin-echo Fourier-transform mapping spectroscopy for broad NMR lines in solids, *J. Magn. Reson., Ser. A* 119 (1996) 22–28.
- [86] L. Canesson, A. Tuel, The first observation of ‘NMR-invisible phosphorus in cobalt-substituted aluminophosphate molecular sieves, *Chem. Commun.* (1997) 241–241.
- [87] L. Canesson, Y. Boudeville, A. Tuel, Local environment of phosphorus atoms in $\text{CoAPO}_4 - n$ molecular sieves: a ^{31}P NMR study, *J. Am. Chem. Soc.* 119 (1997) 10754–10762.
- [88] G. Mali, A. Ristic, V. Kaucic, ^{31}P NMR as a tool for studying incorporation of Ni, Co, Fe, and Mn into aluminophosphate zeotypes, *J. Phys. Chem. B* 109 (2005) 10711–10716.
- [89] J. Kim, D. S. Middlemiss, N. A. Chernova, B. Y. X. Zhu, C. Masquelier, C. P. Grey, Linking local environments and hyperfine shifts: A combined experimental and theoretical ^{31}P and ^7Li solid-state NMR study of paramagnetic Fe(III) phosphates, *J. Am. Chem. Soc.* 132 (2010) 16825–16840.

- [90] D. Massiot, I. Farnan, N. Gautier, D. Trumeau, A. Trokiner, J. P. Courures, ^{71}Ga and ^{69}Ga nuclear magnetic resonance study of $\beta\text{-Ga}_2\text{O}_3$: resolution of four- and six-fold coordinated Ga sites in static conditions, *Solid State Nucl. Magn. Reson.* 4 (1995) 241–248.
- [91] R. W. Schurko, S. Wi, L. Frydman, Dynamic effects on the powder line shapes of half-integer quadrupolar nuclei: A solid-state NMR study of XO_4^- groups, *J. Chem. Phys. A* 106 (2002) 51–62.
- [92] J. Ash, P. J. Grandinetti, Solid-state NMR characterization of ^{69}Ga and ^{71}Ga in crystalline solids, *Magn. Reson. Chem.* 44 (2006) 823–831.
- [93] L. A. O'Dell, R. W. Schurko, Fast and simple acquisition of solid-state ^{14}N NMR spectra with signal enhancement via population transfer, *J. Am. Chem. Soc.* 131 (2009) 6658–6659.
- [94] M.-H. Thibault, B. E. G. Lucier, R. W. Schurko, F.-G. Fontaine, Synthesis and solid-state characterization of platinum complexes with hexadentate amino- and iminophosphine ligands, *Dalton Trans.* (2009) 7701–7716.
- [95] J. Cabana, J. Shirakawa, G. Chen, T. J. Richardson, C. P. Grey, MAS NMR study of the metastable solid solutions found in the $\text{LiFePO}_4/\text{FePO}_4$ system, *Chem. Mater.* 22 (2010) 1249–1262.
- [96] J. Keeler, *Understanding NMR Spectroscopy Second Edition*, Wiley and Sons, Ltd, Chichester, 2010.
- [97] M. Alla, E. Lippmaa, Resolution limits in magic-angle rotation NMR spectra of polycrystalline solids, *Chem. Phys. Lett.* 87 (1982) 30–33.
- [98] X. Lu, J. Trébosc, O. Lafon, D. Carnevale, S. Ulzega, G. Bodenhausen, J.-P. Amoureux, Broadband excitation in solid-state NMR using interleaved DANTE pulse trains with N pulses per rotor period, *J. Magn. Reson.* 236 (2013) 105–116.
- [99] D. Carnevale, A. J. P. Linde, G. Bauer, G. Bodenhausen, Solid-state proton NMR of paramagnetic metal complexes: DANTE spin echoes for selective excitation in inhomogeneously broadened lines, *Chem. Phys. Lett.* 580 (2013) 172–178.

- [100] V. Vitzthum, M. A. Caporini, S. Ulzega, J. Trebosc, O. Lafon, J.-P. Amoureux, G. Bodenhausen, Uniform broadband excitation of crystallites in rotating solids using interleaved sequences of delays alternating with nutation, *J. Magn. Reson.* 223 (2012) 228–236.
- [101] I. Hung, L. Zhou, F. Pourpoint, C. P. Grey, Z. Gan, Isotropic high field NMR spectra of Li-ion battery materials with anisotropy > 1 MHz, *J. Am. Chem. Soc.* 134 (2012) 1898–1901.
- [102] J. Cabana, N. A. Chernova, J. Xiao, M. Roppolo, K. A. Aldi, M. S. Whittingham, C. P. Grey, Study of the transition metal ordering in layered $\text{Na}_x\text{Ni}_{x/2}\text{Mn}_{1-x/2}\text{O}_2$ ($2/3 \leq x \leq 1$) and consequences of Na/Li exchange, *Inorg. Chem.* 52 (2013) 8540–8550.
- [103] N. C. George, A. J. Pell, G. Dantelle, A. Llobet, M. Balasubramanian, G. Pintacuda, B. F. Chmelka, R. Seshadri, Local environments of dilute activator ions in the solid-state lighting phosphor $\text{Y}_{3-x}\text{Ce}_x\text{Al}_5\text{O}_{12}$, *Chem. Mater.* 25 (2013) 3979–3995.

List of abbreviations

ABMS: anisotropic bulk magnetic susceptibility
aMAT: adiabatic magic-angle turning
BRAIN-CP: broadband adiabatic inversion cross polarization
CP: cross polarization
CPMG: Carr-Purcell-Meiboom-Gill
CSA: chemical shift anisotropy
DFT: density functional theory
DANTE: delays alternating with nutation for tailored excitation
EPR: electron paramagnetic resonance
HSQC: heteronuclear single quantum correlation
INEPT: insensitive nuclei enhanced by polarization transfer

MAS: magic-angle spinning
MAT: magic-angle turning
MRI: magnetic resonance imaging
NMR: nuclear magnetic resonance
NOE: nuclear Overhauser effect
PAF: principal axis frame
PASS: phase-adjusted spinning sidebands
PRE: paramagnetic relaxation enhancement
RF: radiofrequency
S³AP: single-sideband-selective adiabatic pulse
SA: shift anisotropy
SHAP: short, high-power adiabatic pulse
SHAP-CPMG: short, high-power adiabatic pulse Carr-Purcell-Meiboom-Gill
TEDOR: transferred echo double resonance
TM: transition metal
VOCS: variable offset cumulative spectroscopy
WURST: wideband, uniform rate, and smooth truncation
WURST-CPMG: wideband, uniform rate, and smooth truncation Carr-Purcell-Meiboom-Gill
Gill
XS: crystallite-selective pulse scheme
ZFS: zero-field splitting